LASER MELTING OF A MOVING SLAB IN RELATION TO SURFACE TREATMENT APPLICATION

BY

Omeir Momin

A Thesis Presented to the
DEANSHIP OF GRADUATE STUDIES

KING FAHD UNIVERSITY OF PETROLEUM & MINERALS

DHAHRAN, SAUDI ARABIA

In Partial Fulfillment of the
Requirements for the Degree of

MASTER OF SCIENCE

In

Mechanical Engineering

May 2011

KING FAHD UNIVERSITY OF PETROLEUM & MINERALS

DHAHRAN 31261, SAUDI ARABIA
DEANSHIP OF GRADUATE STUDIES

This thesis, written by Omeir Momin under the direction of his thesis advisor and approved by his thesis committee, has been presented to and accepted by the Dean of Graduate Studies, in partial fulfillment of the requirements for the degree of **MASTER OF SCIENCE IN MECHANICAL ENGINEERING**.

Thesis Committee

Dr. S. Z. Shuja (Advisor)

Dr. B. S. Yilbas (Member)

Ahmet

Dr. A. Z. Sahin (Member)

Dr. Amro M. Al- Qutub
Department Chairman

Dr. Salam A. Zummo
Dean of Graduate Studies

28/5/11
Date

Dedicated to

My Mother

Thank You

For all the Support, Patience and Love

ACKNOWLEDGEMENT

All praises to Almighty Allah, most merciful and most compassionate, sustainer of the heavens and earth. We ask for His guidance and seek His forgiveness and humbly offer our gratitude for His unlimited blessings.

Acknowledgement is due to King Fahd University for providing me the chance to learn and work in this outstanding environment.

The deepest and most heartfelt appreciation goes to my advisor, teacher and mentor, Dr. Shahzada Zaman Shuja. I cannot thank him enough, for his patience with me and his guidance. I will always be indebted to him for his countless hours of personal attention, his unwavering support and encouragement and his eternal smile. It has been a truly wonderful learning experience.

I must also thank Dr. Bekir Sami Yilbas for his constructive input and his attention. I am truly lucky to have had the opportunity to be in the presence of a truly brilliant mind. His kind words and fatherly gestures are a cool breeze on a hot day. I learnt a lot from him and I wish I had a chance to learn some more.

Thanks is also due to Dr. Ahmet Sahin for his constructive criticism and brilliant insights, which helped to bring this work to a successful conclusion.

My earnest and utmost appreciation goes out to my parents for their constant support and understanding, and teaching me whatever I know today. Without their encouragement, this work would not have been possible. May Allah shower His blessings upon them.

Acknowledgement is due to all the ME faculty, who provided a wonderful learning experience. Special thanks goes out to Dr. Esmail Mokheimer, Dr. Syed Zubair, Dr. M.A. Habib, Dr. M. Antar and Dr. A.F.M. Arif.

I would like to take this opportunity to thank the entire team at the S.O.S. department for their support in running Fluent and Ansys. Their constant support helped me greatly speed up a very computationally expensive problem and bring this work to a quick conclusion.

I would like to acknowledge my friends and seniors at KFUPM: Islam, Awad, Aqeel, Usama, Haris, Ammar as well as Hassan Baig, Murtaza Baig, Bilal Qureshi and all the other graduate students whose company made working and staying at KFUPM truly enjoyable.

TABLE OF CONTENTS

LIST OF FIGURES

LIST OF TABLES

ABSTRACT (ENGLISH)

NAME: OMEIR MOMIN

TITLE: LASER MELTING OF A MOVING SLAB IN RELATION TO SURFACE TREATMENT APPLICATION

MAJOR: MECHANICAL ENGINEERING

DATE: May 15th, 2011

Laser surface treatment process, in general, is involved with conduction heating, melting, and superheating in melt phase. In order to gain an understanding of the physical phenomena taking place during laser heating of a workpiece, experimentation and modeling of the process is necessary. During laser heating, the laser beam moves/scans the workpiece surface with a constant velocity. The laser is pulsating and the intensity is a function of time. In this work, the enthalpy-porosity technique is used to model the melting/solidification process. In the simulations, different metals such as steel and titanium are used as workpiece materials. The temperature and velocity fields generated due to the laser heating are presented. The effect of various parameters is investigated. It is shown that with increasing pulse parameter the melt pool becomes wide and shallow and increasing scanning velocity increases asymmetry. The thermal stress field and residual stresses due to laser heating have also been investigated.

Master of Science Degree
King Fahd University of Petroleum and Minerals
Dhahran, Saudi Arabia
May 2011

ABSTRACT (ARABIC)

الاسم: عمير مؤمن.

العنوان: صهر الليزر لكتله متحركه في علاقه عمليات معالجه السطح.

التخصص: الهندسه الميكانيكيه.

التاريخ: 15 مايو 2011

عمليه معالجه السطح الليزريه, بشكل عام, منخرطه مع عمليه الانتقال الحراري باللمس,الصهر, و الحراره القصوى في حاله الصهر. من أجل فهم العمليات الفيزيائيه التي تحدث خلال التسخين الليزري لقطعه العمل, الاختبار التجريبي و\ او التصميم للعمليه يكون مهما. الاختبار التجريبي مكلف نتيجه للعمليات المحليه ودجات الحراره العاليه المصاحبه للعمليه. دراسات التصميم الكمبيوتريه باستخدام التصميم الرياضي والمحاكاه العدديه يوفر نظره ثاقبه للعمليات الفيزيائيه, التي ممكن ان تستخدم لعمليه تحقيق الامثليه. علاوه على ذلك, خلال عمليه التسخين الليزري, شعاع الليزر يتحرك\ يتفحص سطح قطعه العمل بسرعه ثابته. "الانثالبي" – تقنيه المساميه قد استخدمت لتصميم عمليه الصهر\والصلاده. في المحاكاه, معادن مختلفه مثل الفولاذ و التيتانيوم قد استخدموا كمواد لقطع العمل. وبالتالي , الخصائص المرتبطه بالحراره لهذه المواد قد طبقت في هذا الرمز العددي.

شهاده العلوم في الماجستير

جامعه الملك فهد للبترول والمعادن

الظهران, المملكه العربيه السعوديه

مايو 2011

CHAPTER # 1

INTRODUCTION

Lasers are widely used in the manufacturing industry for surface treatment and machining applications. In surface treatment applications, they are generally used for surface alloying, heat treatment, grain refining, surface cladding, surface hardening, transformation hardening, annealing, glazing and shock hardening besides several other processes. Laser surface treatment processes can be divided into three categories:

i. Heating without melting
ii. Heating with controlled melting
iii. Melting and particle injection

Laser surface treatment offers significant advantages over conventional processes. In some cases, laser treatment is the only option for surface treatment of some surfaces. The advantages of laser surface processing include:

Lasers produce concentrated power which results in very high temperatures locally. This results in a small heat affected zone in the work-piece.

Lasers require electrical energy for operation unlike other processes, which require fuel burning. Thus, they can be used with both inert and active environments. This allows them to be used for processes such as carburizing and nitriding. The time scale of heating and cooling cycles in lasers can be controlled from a few pico-seconds to several seconds allowing for their use in surface treatment processes involving several different kinds of phenomena. Lasers are very precise and surface treatment processes using lasers produce a very high quality finish eliminating the need for any further machining. Laser processing, in general, is fast as compared to conventional methods.

The ablative micromachining abilities of laser find wide-spread use in industry. Lasers are used for drilling very small holes upto a diameter of ~ 1μm, for example, tapered nozzles in ink-jet printers are drilled via laser machining [1-2]. They are employed for laser scribing of thin films, fabrication of MEMS systems and fabrication of surfaces with micro- and nano-scale features such as surface with anti-reflective properties [1].

Lasers are used for high accuracy tasks such as etching high density multi-layered printed circuit boards and lettering of keyboards [2]. Lasers also find applications in cutting, drilling, welding, surface treatment, ablation, etc. [3].

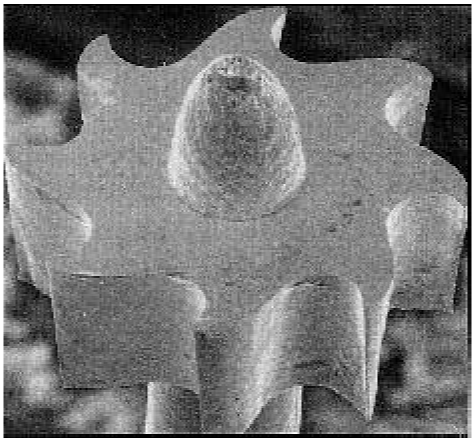

Figure 1: A 470 µm microturbine
manufactured by laser machining
Courtesy of the Rutherford Appleton Lab[1]

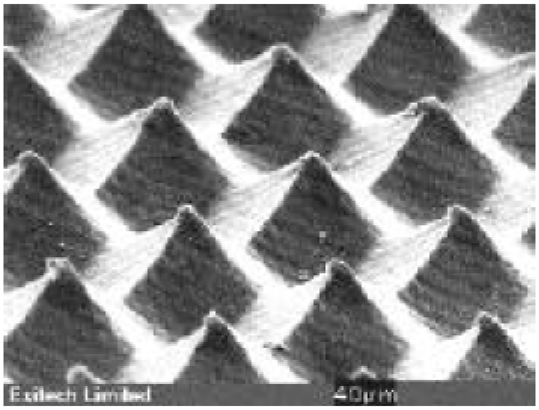

Figure 2: Pyramids produced using a KrF laser
Courtesy of the Rutherford Appleton Lab [1]

The Handbook of Laser Materials Processing by the Laser Institute of America [4] lists the following industrial uses of lasers:

i. Heat treatment
ii. Glazing
iii. Remelting
iv. Alloying/Cladding
v. Surface Cleaning
vi. Brazing/Soldering
vii. Conduction Welding
viii. Penetration Welding
ix. Laser Cutting
x. Hole Drilling Balancing
xi. Marking
xii. Rapid Prototyping
xiii. Trimming
xiv. Laser Marking/Branding
xv. Link Cutting/Making
xvi. Repair
xvii. Photolithography
xviii. Electronic Packaging
xix. Film Deposition and doping

In order to produce the required characteristics in the workpiece, several parameters associated with a laser beam can be varied.

The values of peak power intensity, I_0 and laser scanning speed, U can be varied to achieve optimal temperature distribution for controlled melting. The intensity distribution in the irradiated region can be controlled through the pulse parameter, β. At $\beta = 0$, the distribution is Gaussian. As the value of β increases, the intensity at the spot center is reduced and the energy of the beam is spread more evenly over the radius of the beam.

Laser output can be continuous (continuous wave) or in consecutive pulses (pulse repetition). In many applications, controlled consecutive pulse heating can provide several advantages over consecutive wave. In the case of pulsating laser heating, several additional parameters such as pulse length, duty cycle, and fall and rise times can also be controlled. This additional flexibility allows us greater control over the process in order to achieve optimal temperature distribution.

For example, using selectively spaced multiple power pulses, the temperature profile in the substrate can be maintained above the transformation temperature during laser surface hardening without reaching excessive surface temperatures. This allows us to achieve the desired structure and hardening depth.

Moreover, the cooling rate can also be controlled without the use of a quenching medium [5]. This is because of a phenomenon known as self-quenching. Because of the localized nature of heating, very large temperature gradients are produced between the surface and the bulk of the work piece material. As a consequence, heat is conducted very rapidly from the surface to the bulk leading to rapid cooling. The temperature gradients and hence the cooling rates can be controlled by controlling the laser intensity and laser scanning speed. Higher intensity with a faster scanning speed produces much sharper gradients as compared to lower intensity with a lower scanning speed, while producing the same surface temperatures.

In reality, the power of the laser beam is absorbed within some thickness of the substrate material. This absorption is governed by the Lambert's-Beer law. Using the Lambert's-Beer law one can find that the depth of absorption is shallow for metals, which is on the order of 10^{-8} m. This means that in the modeling of laser heating of metals, the laser beam can be considered as a surface heat source rather than a volumetric heat source with little loss of accuracy but at much lower computational cost.

The efficiency of a laser process is limited by the absorpitivity of the laser in the substrate material. The absorpitivity of most materials can be improved by covering it with energy-absorbing coating. However, this may lead to elements from the paint diffusing into the work piece [6].

At high power intensity heating, the substrate material in the irradiated region undergoes a localized heating and phase change occurs across the irradiated region. In the resulting melt pool, two kinds of convection currents occur. The variation in mass density due to temperature difference causes a phenomenon known as Rayleigh-Bernard convection, while the surface tension variation caused by the temperature gradient produces Marangoni-Bernard convection. Moreover, the laser beam moves/scans the workpiece surface with a constant velocity. This situation modifies the problem so that temperature profile and melt pool size should be analyzed in three dimensions.

Workpiece surface properties during laser treatment are very sensitive to temperature variation. To obtain the desired properties, an understanding of the physical phenomena taking place during surface treatment is very important. However, experimental measurement of the temperature distribution is not feasible because of high temperatures involved and the very short duration of heating. For some cases, the temperature is not very high and we are able to measure the surface temperature using thermocouples. However, it is not possible to measure the temperature inside the bulk of the worpiece. Therefore, numerical simulation of the heating process is imperative.

Through the use of computational fluid dynamics we can gain insight into the temperature and stress fields that develop during the heating process.

Although considerable research studies have been carried out to examine laser controlled melting of metallic surfaces, the influence of laser scanning speed and laser pulse repetition rate on the melt pool formation requires further analysis to improve the physical understanding of the process. Moreover, thermal properties, such as thermal conductivity and specific heat capacity, of the substrate material influence the temperature field in the irradiated region. This requires comparative study including different workpiece materials for process optimization. Consequently, in the present work, the influence of laser scanning speed and material properties on temperature field and melt pool characteristics judged by depth and size, as well as flow field is undertaken.

The different aspects of laser surface treatment process and its uses in industry are introduced in chapter one of this study. The different parameters that can be varied to control the effect of the laser heating process are also explained.

A summary of the research articles most relevant to this work is presented in chapter two. The literature survey covers both journal publications and conference proceedings. The research areas covered in the survey include closed form solutions for limiting case problems, numerical simulations of different heating situations and finite element analysis of resulting thermal stress and strains.

The mathematical modeling aspect of this work is presented in chapter three. The chapter covers the mathematical equations for spatial distribution and time variation of the laser intensity. The effects of various parameters on laser intensity are explained. The initial and boundary conditions are introduced. The numerical techniques used to solve this set of equations are then explained and the enthalpy-porosity technique is presented.

Chapter 4 covers the results and a discussion of the implications of these results. The effect of scanning velocity, laser pulse parameter and material properties is discussed. An experimental verification of these results is presented in chapter 5. Chapter 6 concludes this work with a summary of the results.

CHAPTER # 2

LITERATURE REVIEW

Lasers are widely used in the manufacturing industry for surface treatment processes. As such they have attracted a lot of interest from the academic community and a large quantity of research literature is devoted to this topic. Laser surface heating can lead to solid phase heating, phase-change and evaporation depending on the intensity and duration of heating.

Closed form solutions are available for a few limiting cases which involve only solid phase heating. These cases usually assume an infinite or semi-infinite workpiece with a point or line heating source.

More realistic models are too complex to have a closed form solution and are solved using numerical methods. The laser beam may have a focused or blurred Gaussian profile. This effect is captured by the laser pulse parameter, β. The laser heating involves solid state heating, phase change and liquid phase heating. The temperature of the irradiated zone may rise from room temperature to several thousand Kelvin within a few micro-seconds. The change in temperature leads to change in physical properties which must be included in the model. The change in density leads to Rayleigh-Bernard Convection in the melt pool and the change in surface tension produces Marangoni-Bernard convection. This changes the shape and temperature profile within the melt pool. The temperature gradient and unequal expansion produce thermal stresses. The gradients may be so sharp that it produces permanent plastic strain. The workpiece will have residual stress after cooling to room temperature.

The understanding of the temperature distribution and the resulting stress distribution is important for evaluation of the effect of the laser surface treatment on workpiece properties. A large number of research works have focused on the numerical solution of the temperature and stress fields.

Zhou et al. [7] investigated the transport phenomena and keyhole dynamics during pulsed laser welding. They used VOF method to handle the free surface and accommodated the Marangoni shear in the modeling of the key hole formation and found good agreement between the predictions of weld depth and experimental findings.

Safdar et al. [8] predicted temperature distribution and melt size in the irradiated region for non-conventional laser beam geometries using the surface heat source model with the finite volume method. They concluded that the effect of non-conventional geometries is more pronounced in metals with low thermal conductivity and reduced marangoni flow.

A review of the work on the development, use and effect of non-conventional beam geometries on different laser material processes was carried out by Sheikh and Li [9]. They reported that the potential of non-conventional beam geometries as a process optimization tool is established and new applications utilizing this tool are expected to emerge.

The nano-scale machining using the electron and laser beam was investigated by Wong et al. [10]. They used a Monte Carlo approach and Fresnel reflections to simulate laser heating process and found that approximately 0.5 W from a single electron-beam is sufficient to initialize local evaporation from a thin gold film.

Raj et al. [11] employed particle-tracking algorithm and a simultaneous particle melting consideration in the numerical simulations of laser surface alloying. They found that if the melting temperature of the particles is higher as compared to the base metal, the melting is not instantaneous. Consequently, this model predicted a different composition variation within the resolidified microstructure, as compared to a model that does not incorporate any considerations of distributed melting.

Laser drilling and energy transfer during the heating process was investigated by Wei and Ho [12]. They demonstrated that the drilling speed was a non-linear function of the drilling parameters such as laser power intensity and material thickness.

Fathi et al. [13] studied laser absorption rate and the resulting melt pool depth using superposition principle and the solution of the heat diffusion due to a point heat source. They demonstrated that the maximum melt depth occurred for a certain combination of laser heating parameters.

Shen et al. [14] developed an analytical model for laser heating and melting and showed that discontinuity in the temperature gradient was obvious due to the latent heat of fusion and the increment in thermal conductivity in the solid phase.

Van de Ven and Erdman [15] investigated the laser transmission welding of thermoplastics. They developed a mathematical model to simulate the laser transmission welding process through which temperature was predicted in the welding section. They found the weld width predicted by the model to be in good agreement with experiment.

The enthalpy based lattice Boltzmann model for diffusion dominated solid-liquid phase transformation was introduced by Chatterjee and Chakraborty [16]. They modified the latent heat updating procedure to integrate with the lattice Boltzmann equation predicting the liquid fraction during the continuous evolution of the solid-liquid interface. The results compared well with the continuum model demonstrating the applicability of this method to solve phase change problems.

Thermal behavior and melt pool model in laser material processing were investigated by Sarkar et al. [17]. They modeled the phase change process using a fixed grid enthalpy-porosity technique, which was capable of predicting continuous evolving solid-liquid interface. The effect of scanning speed, laser power, and powder feed rate on geometry and dynamics of the pool, cooling rates, as well as species concentration distribution inside the substrate was investigated.

Laser heating and phase change in the irradiated region was examined by Yilbas and Ben Mansour [18] and Yilbas et al. [19]. A turbulence model was accommodated to account for the turbulence in the evaporating vapor front. It was found that for nanosecond pulses with high intensity, the recession velocity of the surface reaches about 100 m/s at the symmetry axis and the recoil pressure of in the order of 10 GPa is generated in the cavity as a result of rapid evaporation.

Laser heating and phase change process was presented analytically by Yilbas and Shuja [20]. They presented the closed form solution for temperature distribution, provided that the solution was limited to one-dimensional heating situation.

The laser heating of ceramics incorporating the volumetric and surface heating sources was carried out by Li et al. [21]. They indicated that the melt depths and widths predicted from the model using the volumetric heating source were in excellent agreement with the experimental data. This is because of the slow diffusion of the laser beam in ceramics, i.e. absorption length of ceramics is several orders of magnitude larger than the metallic materials, thereby making the surface heating model inaccurate. The finite element simulation of laser spot welding was examined by De et al. [22]. They showed that the results were very sensitive to the assumed absorptivity and the assumed weld pool depth, which were used to define the double ellipsoidal heat source representing the laser beam.

When the surface of the metallic substrate is heated by a laser beam, high temperature gradient is developed in the region irradiated by a laser beam, which in turn results in excessive stress levels in this region. Considerable research studies were carried out to explore the thermal stresses generated in the region heated by a laser beam. Paek and Gagliano [23] introduced an analytical solution to laser heating pulse and modeled the thermal stresses in the region next to cavity. Their solution was limited to surface heat source model, which did not represent accurately the laser heating process.

Thermoelasticity problem for a multilayer coating-substrate heated by a laser beam was examined by Elperin and Rudin [24]. They used Laplace expansion and

Hankel transforms to derive closed form solution for the temperature, displacement and strain distributions for a two-dimensional problem.

A thermal stress development in the surface vicinity of steel due to laser irradiation was studied by Wang et al. [25]. They proposed a new constitutive equation that considers the effects of phase transformation and the effects on the temperature rise and stress generation were investigated numerically. Their results indicate that the residual surface stresses for a laser quenched workpiece are beneficial for the properties of the material.

Yilbas et al [26] investigated thermal stresses due to step input laser pulse heating process. The study involved numerical solutions and experimental validation. They showed that excessive stress levels were generated in the surface region of the substrate material. In addition, microcracks are observed at the surface of the irradiated spot.

Shuja and Yilbas [27] studied modeling of the laser gas-assisted heating process. They modeled the assisting gas impinging on the work piece using Low-Reynolds number k-ε model. They found that the convective cooling effect of the impinging gas jet is more pronounced as the radial distance along the workpiece surface increases.

Yang et al. [28], modeled the characteristics of molten pool during laser processing using a steady-state, fixed-grid source based method. Their results showed good agreement with experiment.

Sowdari and Majumdar [29], solved the problem of laser melting of metals using the commercial FE code ANSYS. An enthalpy based computational model was employed and the results were validated against a limiting case analytical solution.

Kumar and Roy [30] modeled the effect of Marangoni number and scanning speed on powder cladding. They included the Marangoni-Rayleigh-Benard convection and also modeled the evolution of the free surface. The effects of scanning speed Marangoni number on clad built up geometry, dilution level, maximum and average temperature were presented.

Yilbas et al. [31], compared experimental and simulation results for residual stress levels for Laser surface treatment of aluminum and found that the von-Mises stress attains values less than the critical values for the crack formation, particularly after the end of the cooling cycle. The residual stress formed in the surface region was in the order of a few MPa.

Velde et al. [32] carried out numerical simulations of a laser molten pool under the influence of static magnetic fields with different strengths. It is found that in the presence of a static magnetic field applied perpendicular to the plane of interest, the system of vortices due to Marangoni effect was suppressed. This damped flow situation in the melt resulted in a variation of the solute distribution in the solid and in shallower alloyed layers depending upon the applied magnetic induction.

The influence of spatial distribution of laser power intensity on melt pool size and temperature field was modeled by Shuja et al. [33]. The control volume approach was employed and significant effect of the laser pulse parameter was found on the size if the melt pool.

The competitive influence of Marangoni flow and vaporization driven flow in type 304 stainless steel was numerically modelled by Lei et al. [34] using a one-domain mixture continuum model. It was shown that for low values of surface tension gradient, the effect of Langmuir-type vaporization on surface peak temperature and pool profile is significant. However, if the surface tension temperature coefficient is greater than 0.0003, the influence of langmuir-type vaporization heat loss is very small.

Chakraborty and Chakraborty [35] modeled the effects of turbulence during laser of a copper-nickel dissimilar couple are studied using a high Reynolds number k-ε model. The effect of turbulence was most pronounced for species transport. The resulting composition predictions were found to be in good agreement with experiment.

Laser melting of ceramics was modeled by Li et al. [36]. Marangoni-convection and a realistic binary phase diagram were included in a three-dimensional model. It was demonstrated that the most accurate predictions were obtained by including both the latent heat of fusion and fluid flow in the melt pool.

Yilbas and Naqvi [37] used Finite Volume method to predict the cavity produced due to laser heating and validated the code with experimental results. The temperature profile was used to predict stress field. It was observed that the equivalent stress reaches its maxima at two locations in the radial direction.

Raj et al. [38] modeled the alloying of aluminum using nickel powder through laser irradiation. They showed that the melting of the alloying element is not instantaneous and hence it cannot be modeled as a species mass flux boundary condition.

Pinkerton and Li [39] developed a model to predict the width and height of the deposition layer for the case of high powder mass flow rates when the layer's width can become greater than the melt pool width at the substrate surface. The model is based on one-dimensional heat conduction to the substrate and expressions for the elongation of the melt pool with increase in traverse speed. Predicted dimensions correspond well with experimental values.

Chung and Das [40] used a 1-D model to predict melting, vaporization and resolidification in metals subjected to continuous wave (cw) step heat flux input. The model is based on the Stefan problem with appropriate boundary conditions. Based on this model relations for time to reach melting, vaporization and resolidification were developed and compared with other closed form solutions.

Yilbas et al. [41] studied the Laser welding of mild steel sheets under nitrogen assisting gas ambient. Temperature and stress field were predicted using FEM. XRD technique was used to get experimental results. The predictions were found to be in good agreement with experimental values.

Chen and Huang [42] modeled thermocapillary flow during laser heating using a finite difference method and grid-stretching transformation to place more grid points near the surface. They demonstrated that the value of latent heat of fusion has a significant effect on the shape of the melt pool.

Alimardani [43] et al. developed a 3D transient numerical approach to model the deposition geometry and temperature and stress fields during multilayer laser solid free form fabrication. They assumed interaction between laser beam and powder stream to be decoupled. The interaction of the laser beam with the substrate material is solved numerically to obtain the melt pool boundary. Layers are then added based on powder feed rate, elapsed time and intersection of the melt pool and powder stream area. The results were verified experimentally.

Ahmed et al. [44] developed an analytical model to predict the effect of beam shape on melt pool characteristics for inconel 625. Multiple Gaussian sources are superimposed to form a rectangular beam and results are compared with a single circular Gaussian source model as well as experimental results from a high power diode laser with a rectangular beam. Melt depth and melt pool profile and progression have been predicted by modeling, which are compared with experimental results. The model is shown to give a reasonable prediction of melt pool shape.

Toyserkani et al. [45] used a FE model to predict the effect of laser beam shape, scanning speed and powder jet geometry on laser cladding process. The interaction between the powder and melt pool is assumed to be decoupled allowing the problem to be solved sequentially. The quality of clad bead for different parameter sets was experimentally evaluated and shown as a function of effective powder deposition density and effective energy density. The comparisons showed excellent agreement between the modeling and experimental results for cases in which a high quality clad bead were expected.

Nisar et al. [46] studied the crack formation in a glass work piece due to laser irradiation. The purpose of the study was to minimize cut path deviation at the leading and trailing edges. They used finite element method to predict the deiation and carried out experimental validation. They showed that the beam geometry has significant effect on the cut path. In comparison to other beam geometries, the triangular-forward beam at the leading edge and triangular-reverse and circular beam geometry at the trailing edge produces lower tensile stresses and hence minimizes the cut path deviation. The minimum deviation is produced using triangle-forward and triangle-reverse geometries.

Safdar et al. [47-48], analyzed the effect of laser beam geometries on transformation hardening of En 43A steel using FEA. They simulated circular, triangular and rectangular shapes and showed that conventional circular and square geometries are not the optimum shape for hardening. Triangular beam geometry was shown to produce the best thermal history to achieve better transformation and highest hardness due to slower heating without sacrificing the processing rate and hardening depths.

Kim and Kim [49] studied the effect of deformable surface on the melt pool characteristics using axisymmetric FE analysis. They reported the effect on crater depth and rim height for several Re, Ca, B_f and free surface shapes.

Wang, Shi, and Gong [50] simulated the pressure distribution around the keyhole during laser heating. They showed that the formation of the shoulder in the weld pool is a function of the movement of the keyhole relative to the work piece, friction of the metal vapor escaping from the keyhole and buoyancy.

Peng et al. [51] used numerical modeling to study the effects of initial melt pool shape on laser melting of solids. Effects of the heat transfer intensity and the Marangoni number on the melting process were also investigated. Taking the critical time as the time required for heat conduction mechanism to control the formation of initial molten pool, they found that for initial pool having a melting time less than the critical time, the subsequent numerical results are independent of the assumed initial pool.

Hoche et al. [52] studied Marangoni convection, free-surface evolution and nitrogen diffusion in free electron laser nitriding of Titanium. Numerical simulations were carried out using the commercial FE code, COMSOL. In order to model the surface deformation, the level set method was used. The simulations were compared with micrographs of nitrided titanium samples and good agreement was found.

Sim and Kim [53] studied the evolution of free surface in laser melting of steel using an axisymmetric Finite Volume formulation. Zhao et al. [54] showed that as oxygen is absorbed during laser melting, the value of the surface tension is affected and the Marangoni flow in the pool evolves accordingly.

Morvan et al. [55] used fixed-grid enthalpy porosity technique to study the effect of thermocapillary convection in aluminum and an aluminum alloy. The work presents the effects of laser scanning velocity and beam radius.

Yilbas et al. [56] carried out the laser nitriding of tool steel. The metallurgical changes in the irradiated region were examined using a scanning electron microscope. The residual thermal stress was modeled using finite element analysis. Good agreement was found between predictions and experimental results.

Al-Qahtani and Yilbas [57] obtained a closed form solution for temperature variation in the substrate due to step input and time exponentially varying pulses. It was demonstrated that the start of the cooling period is clearly evident for step input pulses but not for exponential pulses.

Matsunawa [58-60] studied the effects of different parameters on the shape of the free surface in detail by employing simple analytical models.

Gratzke et al. [61] studied the phenomena of humping at the free surface. The Rayleigh's theory of instability of a free liquid cylinder was used to calculate the minimum processing speed needed for humping to occur. Results were found to be in good agreement with experimental results. They also demonstrated that humping decreases with increasing power.

Beck et al. [62] used FEM methods to solve for the shape of the irradiated surface. However, phase change was neglected in the model. Mackwood [63] outlined the different methods in literature employed to model laser material interaction. Lambrakos et al. [64] solved the combined equations of energy, momentum and continuity to predict the temperature and fluid velocity field for deep penetration. The laser is modeled with time dependant boundary conditions. The isotherms and convection patterns predicted by the model were presented.

Klemens [65] developed a numerical model to investigate theoretically the factors affecting the dimensions of the cavity and melt zone. They reported that for laser beam penetration depends on power but is independent of collimation.

Andrews and Atthey [66] modeled keyhole cross-sections solving for bouyancy and surface tension. They demonstrated that surface tension reduces the size of the keyhole by upto one-third.

Dowden et al. [67] developed a general model of liquid and vapor motion in the keyhole to predict the keyhole depth based on different parameters. The model provided good approximations for open and blind keyholes. However, the authors conclude that the model is unable to predict the complex three-dimensional flow of heat and fluid in the melt pool at the top of the keyhole.

Kroos et al. [68] calculated the collapse time of the keyhole after the laser irradiation is stopped. It was discovered that the characteristic time constant is a lower limit of the keyhole closing time and under real world conditions, the keyhole is expected to perform oscillations of several hundred Hertz.

Fabbro and Chouf [69-70] studied the effect of welding speed, laser incident intensity and substrate material on the keyhole geometry. They used ray-tracing technique to account for multiple reflections inside the keyhole. The rear wall of the keyhole was demonstrated to oscillate around an apparent equilibrium.

The literature survey shows that several different approaches have been employed to model several parameters affecting laser heating of a workpiece. However, very few works exist in literature, that employ models with realistic boundary conditions incorporating three-dimensional marangoni flow. The marangoni flow can greatly alter the heating situation and the melt pool shape and size.

However, modeling flow inside the melt pool with realistic boundary conditions presents a unique set of difficulties. The workpiece dimensions are several orders of magnitude larger than the melt pool dimensions. Therefore, the conduction heat transfer occurs at very different length scales as compared to the convection heat transfer. Maintaining reasonable accuracy within the melt pool while keeping the grid size small enough to be solvable within available computational resources is a challenge. This work aims to fill this gap in available literature.

CHAPTER # 3

MATHEMATICAL MODELING

3.1 MODELING OF TEMPERATURE FIELD

3.1.1. Modeling of Laser Heating

This work undertakes to study the effect due to a pulsating laser scanning a metal work piece with a constant velocity, U. The laser heating situation is shown in figure (3). The xz plane is the symmetry plane. The laser irradiation is modeled as a heat source. Due to the laser heating, a temperature field develops. The governing equation for solving the temperature field is the energy equation.

3.1.2. Conservation of Energy

The conservation of energy equation pertinent to laser heating process can be written as:

$$\rho\frac{Dh}{Dt}=\left(\nabla\left(k\nabla T\right)\right)$$

or:

$$\rho\frac{D\left(C_P T\right)}{dt}=\left(\nabla\left(k\nabla T\right)\right) \qquad (1)$$

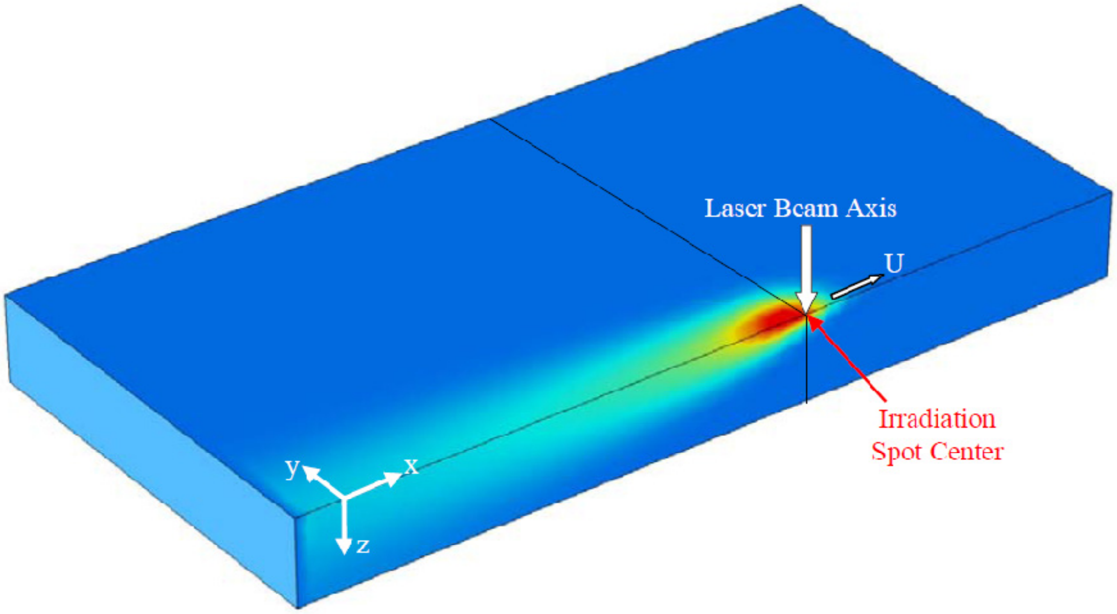

Figure 3: Schematic view of laser heating of a moving workpiece and coordinate system

3.1.3. Initial and Boundary Conditions for the Energy Equation

Equation (1) can be solved numerically with the appropriate boundary conditions to predict the temperature field in the substrate material. Initially (prior to laser heating), the substrate material is assumed to be at ambient temperature, i.e. $T = T_{amb}$, which is considered as constant ($T_{amb} = 300$ K).

t = 0 : $$T(x, y, z, 0) = T_o$$

At the free surfaces of the work piece, the convective boundary is assumed. Therefore, the corresponding boundary conditions are:

y at infinity : $$y = \infty : \frac{\partial T(x, \infty, z, t)}{\partial y} = -\frac{h_t}{k}\left(T - T_\infty\right)$$

z at infinity : $$z = \infty : \frac{\partial T(x, y, \infty, t)}{\partial z} = -\frac{h_t}{k}\left(T - T_\infty\right)$$

where h_t is the heat transfer coefficient due to natural convection, and T_∞ is the ambient temperature.

At far away boundary (at edges of the solution domain along the x-axis) constant temperature boundary may be assumed (T = 300 K), i.e.

$$x = \pm\infty \quad \rightarrow \quad T = 300 \text{ K}$$

3.1.4. Modeling of the Laser Beam as a Heat Source

The absorption of the laser beam inside the bulk is governed by the Lambert-Beer law, which states that light is absorbed as an exponential function. The distance at which 63% of the light is absorbed is called absorption depth. Typical absorption depth for metals is in the range of 10^{-8} m [4]. Therefore, we can model the laser energy as a surface heat source instead of a volumetric heat source without much loss of accuracy but at a much lower computational cost. This means that at the irradiated surface of the workpiece, we will have a heat flux boundary condition:

At z=0: $$\frac{\partial T(x,y,0,t)}{\partial z} = S_o \times f(t),$$

where, S_o is the source term due to laser heating. S_o is a function of spatial coordinates and *f(t)* is a function of time as discussed in the following sections.

3.1.5. Modeling of Time Modulated Laser Beam

The laser heating takes place as a series of short pulses. The total pulse length is denoted as t_p, which includes both the heating period and the cooling period. The ratio of the heating period to the total pulse length is known as duty. We assume that initially the laser intensity increases linearly. This is known as ‘rise time’. Laser beam intensity remains constant through the duration of the pulse. At the end of the heating pulse, the laser intensity falls linearly during the ‘fall time’.

Table 1: Laser pulse parameters used in the simulations.

Laser Pulse Length, t_p (μs)	Duty	Pulse Rise Time, t_r (μs)	Pulse Fall Time, t_f (μs)	Average Power (W)	Pulse Parameter (β)	Guassian Parameter, “a” (μm)
100	60%	1	1	131.947	0 - 1	200

The consecutive pulses can be modeled using a time function *f(t)*, which is expressed as:

$$f(t)=\begin{cases} 0, & mod\left(t,t_p\right)=0 \\ \dfrac{t}{t_r}, & mod\left(t,t_p\right)<t_r \\ 1, & t_r \le mod\left(t,t_p\right)\le t_r+t_c \\ \dfrac{t_r+t_c+t_f-t}{t_f}, & t_r+t_c<mod\left(t,t_p\right)<t_r+t_c+t_f \\ 0, & mod\left(t,t_p\right)>t_r+t_c+t_f \end{cases} \qquad (2)$$

where t_r is the pulse rise time, t_f is the pulse fall time and t_c is the time during which laser is turned on at full intensity. In this expression, 'mod' represents the modulo function.

3.1.6. Modeling of the Spatial Distribution of the Laser Beam Energy

Since the laser beam is moving along the x-axis, the x-coordinate of the irradiation spot center is given by:

$$x_0=U\times t$$

where 'U' is the scanning velocity of the beam and 't' is the time. The intensity of the beam is assumed to have a normal distribution represented by the expression:

$$S_0=I_0\,exp\left(-\left(\frac{r}{a}-\beta\right)^2\right)$$

where

$$r=\sqrt{\left(x-x_0\right)^2+y^2}$$

'I_0' is the peak intensity, 'a' is the Gaussian parameter, and 'β' is the pulse parameter. Integrating the term over total area, we get the total power deposited by the laser beam:

$$P=\int_{-\infty}^{\infty}\int_{0}^{2\pi} I_0\, exp\left(-\left(\frac{r}{a}-\beta\right)^2\right)d\theta dr$$

$$=2\pi\int_{-\infty}^{\infty} I_0\, exp\left(-\left(\frac{r}{a}-\beta\right)^2\right)dr$$

$$P=I_0 a 2\pi\sqrt{\pi}\left(1+erf\left(\beta\right)\right)$$

The value of I_o is adjusted so that the total power remains constant for all values of laser pulse parameter, β. The intensity distributions for several different values of pulse parameter, β are plotted in figure (4).

3.1.7. Modeling of Melting and Solidification

The high intensity of the laser beam produces very high temperatures locally. This leads to phase change and produces a region of molten metal. The enthalpy-porosity technique is used to model the melting/solidification process [73]. The melt interface is identified through a liquid fraction, which is the fraction of the cell volume, i.e., liquid state to total volume of the concerned cell. The liquid fraction is computed at each iteration through satisfying the enthalpy balance. The mushy zone is a region in which the liquid fraction varies between 0 and 1. The mushy zone is assumed to be a "pseudo" porous medium, in which the porosity changes from 1 to 0 as the material solidify. Upon full solidification of the material, the porosity becomes zero in a cell.

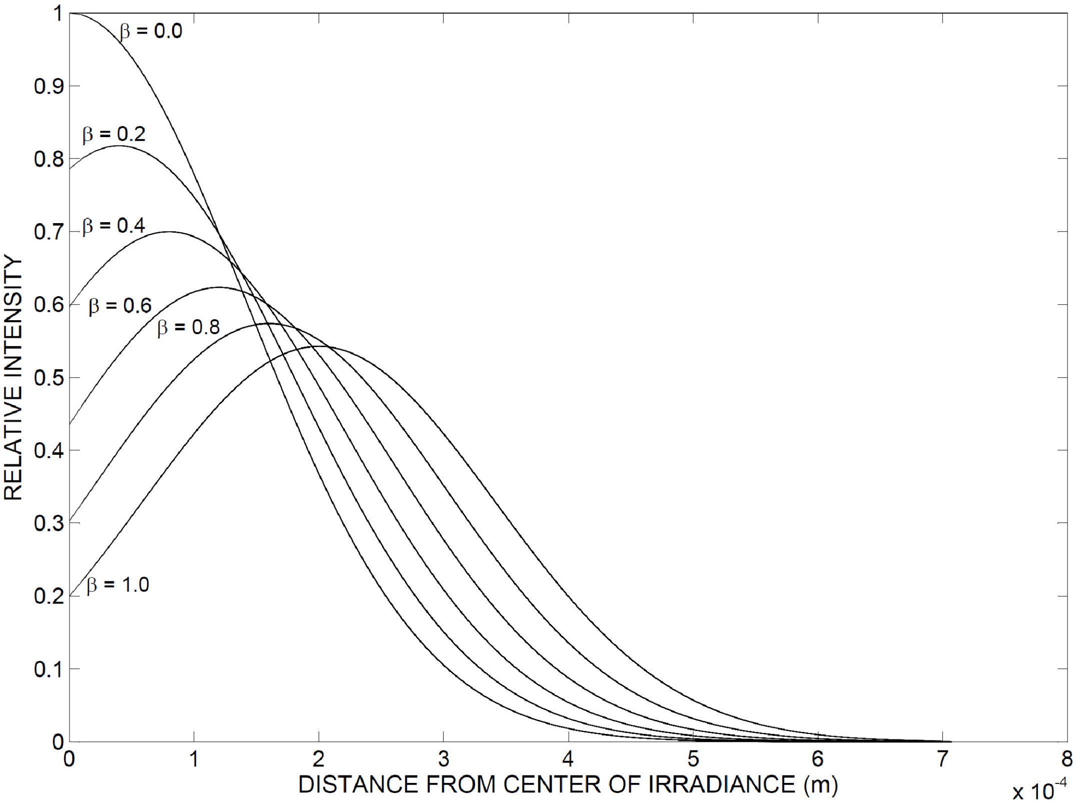

Figure 4: Distribution of intensity as a function of distance from center of irradiance and different values of pulse parameter, β

The energy balance in the substrate material can be presented through the enthalpy balance. The enthalpy of the material is computed as the sum of the sensible enthalpy, h, and the fraction of the latent heat of fusion, Δh_{lat} ($\Delta h_{lat} = \theta h_{lat}$, where h_{lat} is the latent heat of fusion), in case if the material undergoes melting:

$$h = h_{sens} + \Delta h_{lat} \qquad (3)$$

Where

$$h_{sens} = h_{ref} + \int_{T_{ref}}^{T} c_p \, dT \qquad (4)$$

And h_{ref} = reference enthalpy

T_{ref} = reference temperature

c_p = specific heat at constant pressure

The liquid fraction, θ, is defined as:

$\theta = 0$ if $T < T_{solidus}$

$\theta = 1$ if $T > T_{liquidus}$

$$\theta = \frac{T - T_{solidus}}{T_{liquidus} - T_{solidus}} \quad \text{if} \quad T_{solidus} < T < T_{liquidus} \qquad (5)$$

Equation (5) is referred to as the lever rule. The latent heat content can vary between zero (for a solid) and h_{lat} (for a liquid).

The solution for temperature is essentially iteration between the energy equation and the liquid fraction equation. Directly using energy equation to update the liquid fraction usually results in poor convergence of the energy equation; therefore, the method suggested by Voller and Prakash [71] has been used to update the liquid fraction based on the specific heat. All the properties for the simulation are taken as functions of temperature as discussed later. The variation in density and surface tension produce rayleigh and marangoni convection respectively. To solve for the convection in the melt pool, appropriate governing equations have been introduced.

3.1.8. Conservation of Mass

For a problem with a non-constant density the equation of conservation of mass is given by:

$$\frac{\partial \rho}{\partial t} + \nabla .\left(\rho \mathbf{u}\right) = 0$$

This is known as the continuity equation. It is relevant only in the melt pool. In the solid bulk all the terms reduce to zero.

3.1.9. Conservation of Momentum

The equation of conservation of momentum in the melt pool is the Navier-Stokes equation, which is given by:

$$\rho \frac{D\mathbf{u}}{Dt} = -\nabla P + \mu \nabla^2 \mathbf{u} + \rho \mathbf{g} + S$$

The gravity is acting in the positive z-direction. The gravity vector **g** has a value of 9.8 m/s in the z-direction but it is zero in all other directions.

In the mushy regions the velocity reduces and in the solid zones, the velocities extinguish to zero. To account for this a sink term is introduced in the momentum equation:

$$S = \frac{(1-\theta)^2}{\left(\theta^3 + \varepsilon_o\right)} A_{mush}\mathbf{u}$$

where, ε_o is a small number to avoid division by zero. A_{mush} is the damping constant. The higher the value of this constant, the steeper the transition of the velocity of the material to zero as it solidifies. The value of this constant is based on experience. Including the source term in the momentum equation, the momentum equation becomes:

$$\rho\frac{D\mathbf{u}}{Dt} = -\nabla P + \mu\nabla^2\mathbf{u} + \rho\mathbf{g} + \frac{(1-\theta)^2}{\left(\theta^3 + \varepsilon_o\right)} A_{mush}\mathbf{u}$$

Voller and Prakash [71] have explained the effect of the source term in the momentum equation. In the liquid region, θ =1 and the source takes a zero value and the momentum equations are in terms of the actual fluid velocities. In the mushy region the value of θ decreases such that the value of the source term begins to dominate the transient, convective, and diffusive terms and the momentum equation approximates the Darcy law. As the local liquid fraction approaches 0, the source term dominates all other terms in the momentum equation and forces the predicted velocities to values close to zero.

3.1.10. Shear stress Boundary Condition for the momentum equation

At the free surface of the melt pool, surface tension exists. The value of the surface tension is a temperature dependant material property. Consequently, a variation in the surface temperature of the melt pool produces a variation in the surface tension. The uneven distribution of the surface tension produces net shear stress acting on the free surface. This shear stress produces marangoni-bernard convection cells in the melt pool. Therefore, a shear stress boundary condition is introduced for the momentum equation at the free surface of the melt pool.

$$\tau = \frac{d\gamma}{dT} \nabla T$$

3.1.11. Numerical Solution of Mass, Energy and Momentum Equations

To discretise the governing equation, a control volume approach is introduced. The calculation domain is discretised using a multi-block non-conformal grid and a grid independence test has been performed for different grid sizes and orientation. Finer grids are located near the irradiated spot center in the vicinity of the surface and grids become coarser as the distance increases towards the bulk of substrate material. The central difference scheme with second order accuracy was adopted for the diffusion terms. Second-order accuracy is achieved by truncating expressions containing third and higher powers of the spatial term in the Taylor series expansion. The second-order upwind scheme was used to discretise pressure and velocity terms. In this approach, higher-order accuracy is achieved at cell faces through a Taylor series expansion of the cell-centered solution about the cell centroid of the upwind cell. Fully implicit second-order method was used for the discritasation in time. This ensures that the solution is unconditionally stable. The details of the numerical scheme are given in [72].

3.1.12. Modeling of Temperature Dependant Material Properties

In the simulations, steel and titanium were used as workpiece materials. Consequently, temperature dependent properties of these materials have been employed in the numerical code. The various properties of Steel and Titanium used in the simulation were taken from various studies [74-77]. These properties are listed in table 2 and plotted in figures (5) and (6).

Table 2: Various properties of Steel and Titanium

	Titanium	Steel
Viscosity, ν $\left(N\,s/m^2\right)$	5.2×10^{-3}	5.53×10^{-3}
Enthalpy of fusion, Δh $\left(kJ/kg\right)$	391	272
Temperature coefficient of Surface Tension, $\frac{d\gamma}{dT}$ $\left(Pa/K\right)$	-2.8×10^{-4}	-4.3×10^{-4}
Solidous / Liqudous Temperature, T_{mp} $\left(K\right)$	1958	1670

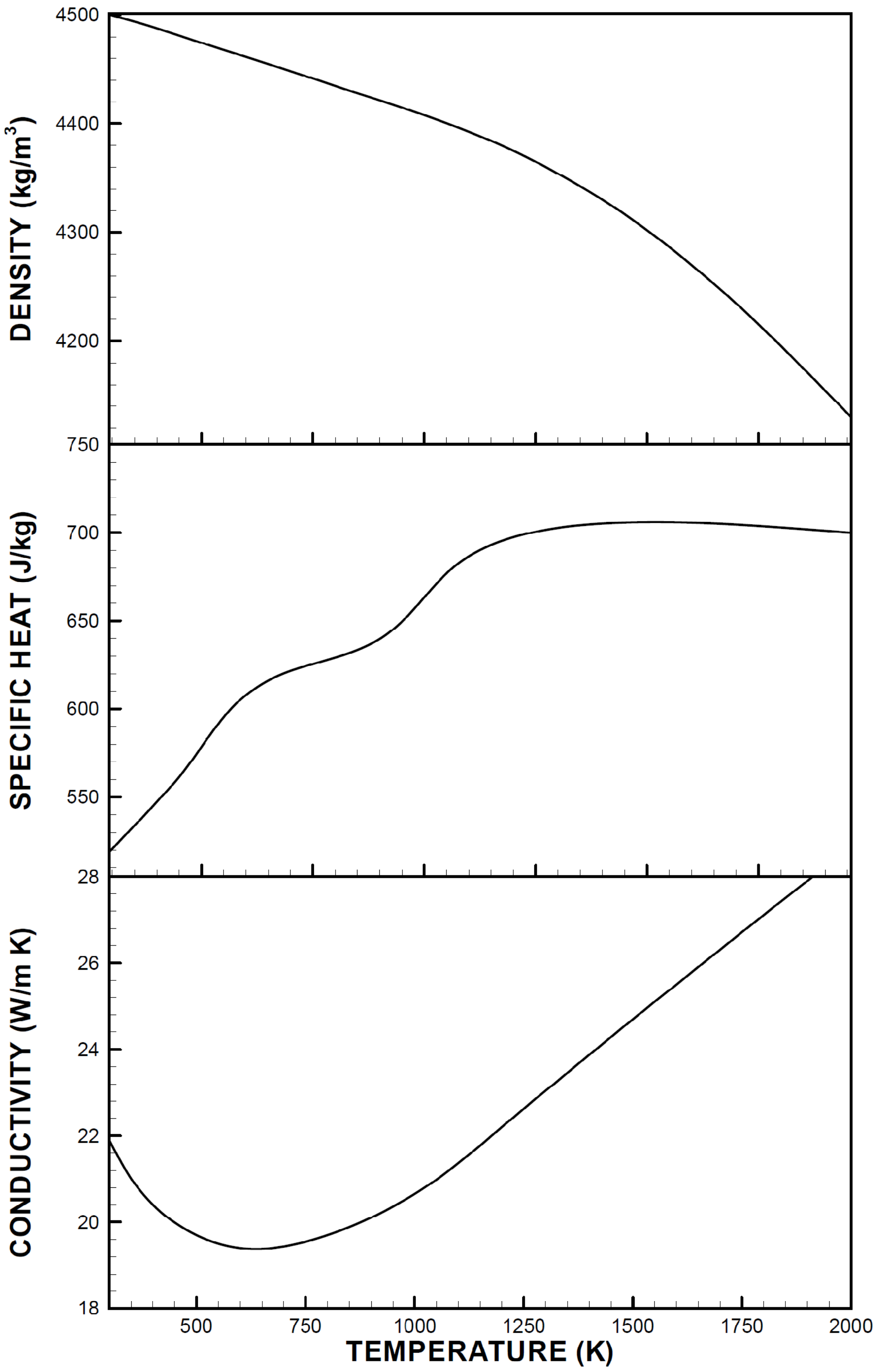

Figure 5: Various properties of Titanium as a function of temperature

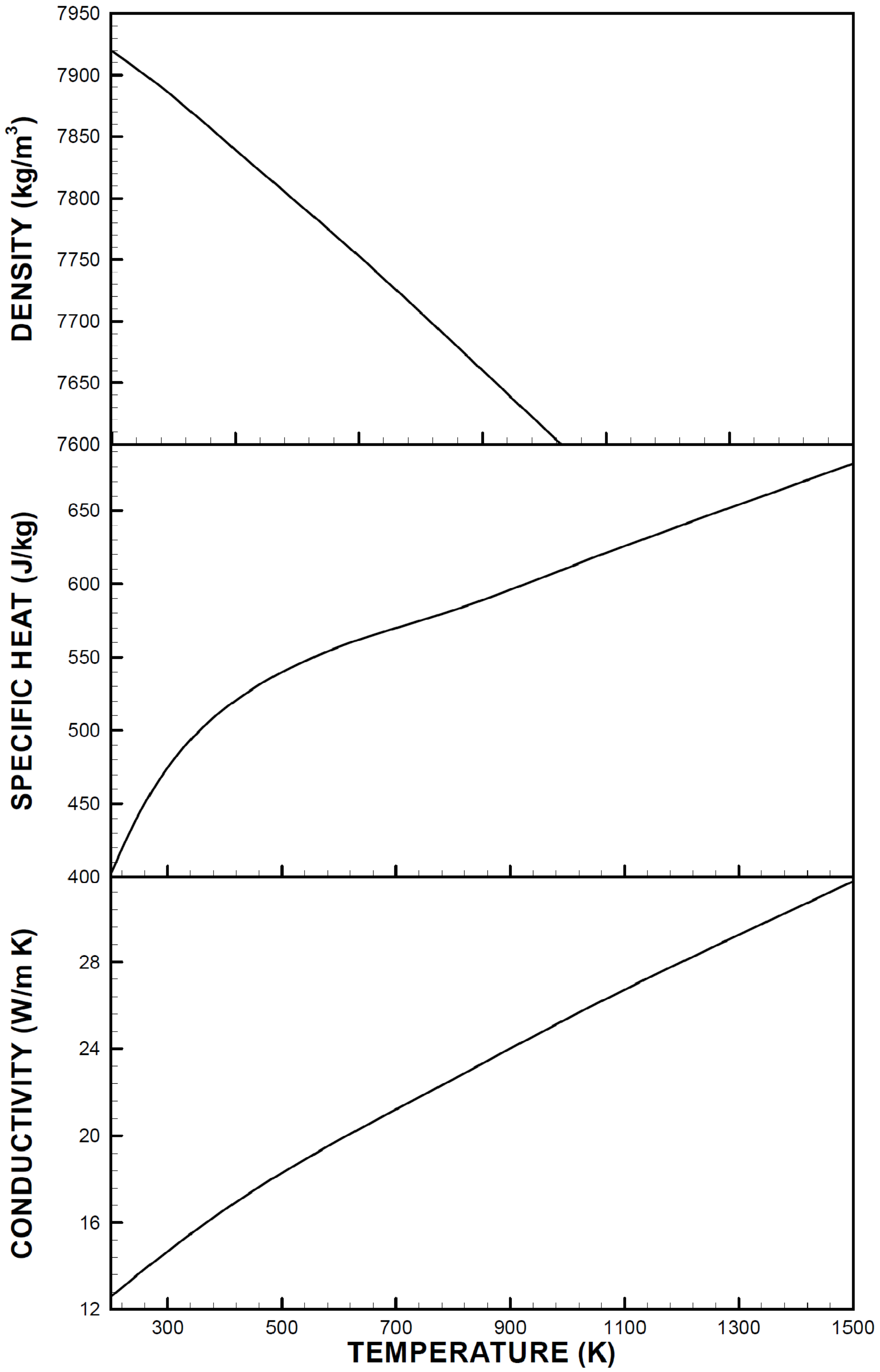

Figure 6: Various properties of Steel as a function of temperature

3.2. MODELING OF THERMAL STRAIN

3.2.1. Modeling of Stress-Strain Relations

The fundamental law governing stress-strain relationship is the Hooke's Law. For a one-dimensional problem the Hooke's Law can be written in its simplest format as shown below:

$$\sigma \propto \varepsilon$$

or

$$\sigma = \frac{1}{E_{elastic}} \varepsilon$$

For a three dimensional problem, stress is a third order tensor. The components of the stress tensor on a 3D element are shown in figure (7). Due to symmetry, the tensor can be reduced to six elements instead of nine as shown below:

$$\begin{pmatrix} \sigma_1 & \sigma_4 & \sigma_5 \\ \sigma_4 & \sigma_2 & \sigma_6 \\ \sigma_5 & \sigma_6 & \sigma_3 \end{pmatrix} = \begin{pmatrix} \sigma_{xx} & \sigma_{xy} & \sigma_{xz} \\ \sigma_{yx} & \sigma_{yy} & \sigma_{yz} \\ \sigma_{zx} & \sigma_{zy} & \sigma_{zz} \end{pmatrix}$$

Similarly, Strain can be reduced to six elements

$$\begin{pmatrix} \varepsilon_1 & \varepsilon_4 & \varepsilon_5 \\ \varepsilon_4 & \varepsilon_2 & \varepsilon_6 \\ \varepsilon_5 & \varepsilon_6 & \varepsilon_3 \end{pmatrix} = \begin{pmatrix} \varepsilon_{xx} & \varepsilon_{xy} & \varepsilon_{xz} \\ \varepsilon_{yx} & \varepsilon_{yy} & \varepsilon_{yz} \\ \varepsilon_{zx} & \varepsilon_{zy} & \varepsilon_{zz} \end{pmatrix}$$

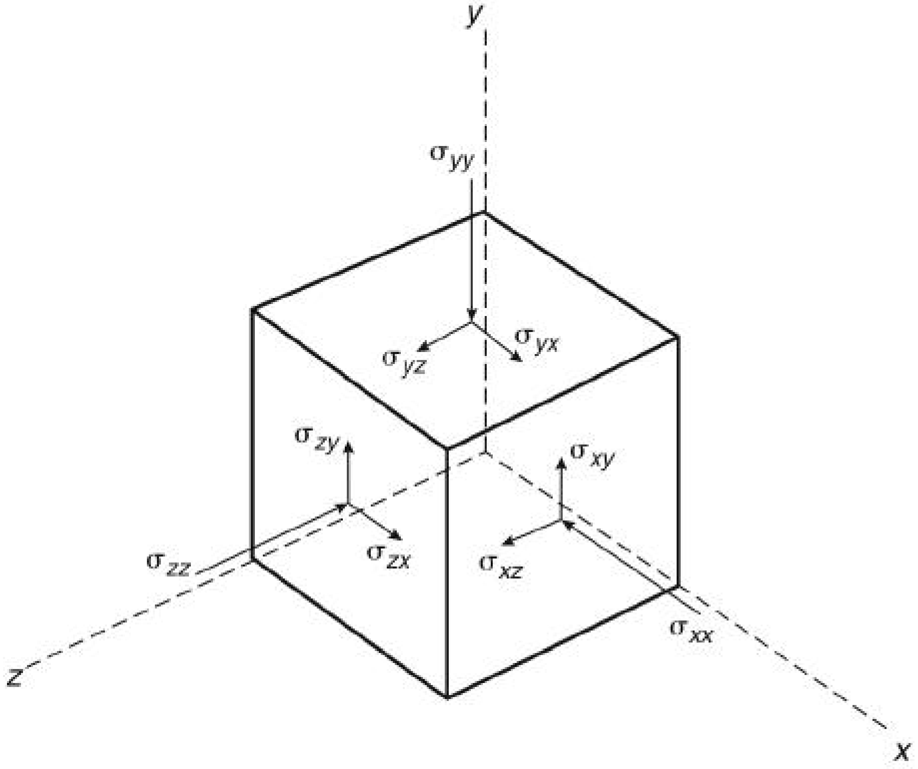

Figure 7: Stress Components

So, the Hooke's law for a three dimensional problem is:

$$\begin{pmatrix}\sigma_1\\ \sigma_2\\ \sigma_3\\ \sigma_4\\ \sigma_5\\ \sigma_6\end{pmatrix}=\begin{pmatrix}c_{11} & c_{12} & c_{13} & c_{14} & c_{15} & c_{16}\\ c_{21} & c_{22} & c_{23} & c_{24} & c_{25} & c_{26}\\ c_{31} & c_{32} & c_{33} & c_{34} & c_{35} & c_{36}\\ c_{41} & c_{42} & c_{43} & c_{44} & c_{45} & c_{46}\\ c_{51} & c_{52} & c_{53} & c_{54} & c_{55} & c_{56}\\ c_{61} & c_{62} & c_{63} & c_{64} & c_{65} & c_{66}\end{pmatrix}\begin{pmatrix}\varepsilon_1\\ \varepsilon_2\\ \varepsilon_3\\ \varepsilon_4\\ \varepsilon_5\\ \varepsilon_6\end{pmatrix}$$

An isotropic material is one where the properties are equal in all directions. For an isotropic material, the stress-strain relation reduces to:

$$\begin{pmatrix}\sigma_1\\ \sigma_2\\ \sigma_3\\ \sigma_4\\ \sigma_5\\ \sigma_6\end{pmatrix}=\begin{pmatrix}c_{11} & c_{12} & c_{12} & 0 & 0 & 0\\ c_{12} & c_{11} & c_{12} & 0 & 0 & 0\\ c_{12} & c_{12} & c_{11} & 0 & 0 & 0\\ 0 & 0 & 0 & c_{44} & 0 & 0\\ 0 & 0 & 0 & 0 & c_{44} & 0\\ 0 & 0 & 0 & 0 & 0 & c_{44}\end{pmatrix}\begin{pmatrix}\varepsilon_1\\ \varepsilon_2\\ \varepsilon_3\\ \varepsilon_4\\ \varepsilon_5\\ \varepsilon_6\end{pmatrix}$$

or

$$\{\sigma\}=\{D\}\{\varepsilon\}$$

This tensor represents the six scalar equations:

$$\sigma_1=\frac{E}{(1+\nu)(1-2\nu)}\left[(1-\nu)\varepsilon_1+\nu(\varepsilon_2+\varepsilon_3)\right]$$

$$\sigma_2=\frac{E}{(1+\nu)(1-2\nu)}\left[(1-\nu)\varepsilon_2+\nu(\varepsilon_3+\varepsilon_1)\right]$$

$$\sigma_3=\frac{E}{(1+\nu)(1-2\nu)}\left[(1-\nu)\varepsilon_3+\nu(\varepsilon_2+\varepsilon_1)\right]$$

$$\sigma_4 = \frac{E}{1+\nu}\varepsilon_4 \qquad \sigma_5 = \frac{E}{1+\nu}\varepsilon_5$$

$$\sigma_6 = \frac{E}{1+\nu}\varepsilon_6$$

3.2.2. Modeling Plasticity

The Hooke's Law is only valid within the elastic limit. Beyond the proportional limit, the stress-strain relation is no longer linear as shown in figure (8). Once the yield point is reached, plasticity occurs, characterized by non-recoverable strains. We use the von-mises stress to check if plasticity is occurring. The von-Misses stress is defined as:

$$\sigma_{vm} = \sqrt{\frac{(\sigma_{11}-\sigma_{22})^2 + (\sigma_{22}-\sigma_{33})^2 + (\sigma_{11}-\sigma_{33})^2 + 6\left(\sigma^2{}_{12} + \sigma^2{}_{23} + \sigma^2{}_{31}\right)}{2}}$$

When $\sigma_{vm} > \sigma_{yield}$, plasticity occurs. The slope of the stress strain curve in the plastic region is known as the tangent modulus.

If the tangent modulus has a value of zero, it is known as elastic perfectly-plastic. For an elastic perfectly-plastic isotropic material, in the plastic region:

$$\sigma_{vm} = \sigma_{yield}$$

i.e., there is no strain-hardening and von-mises stress cannot exceed the yield stress.

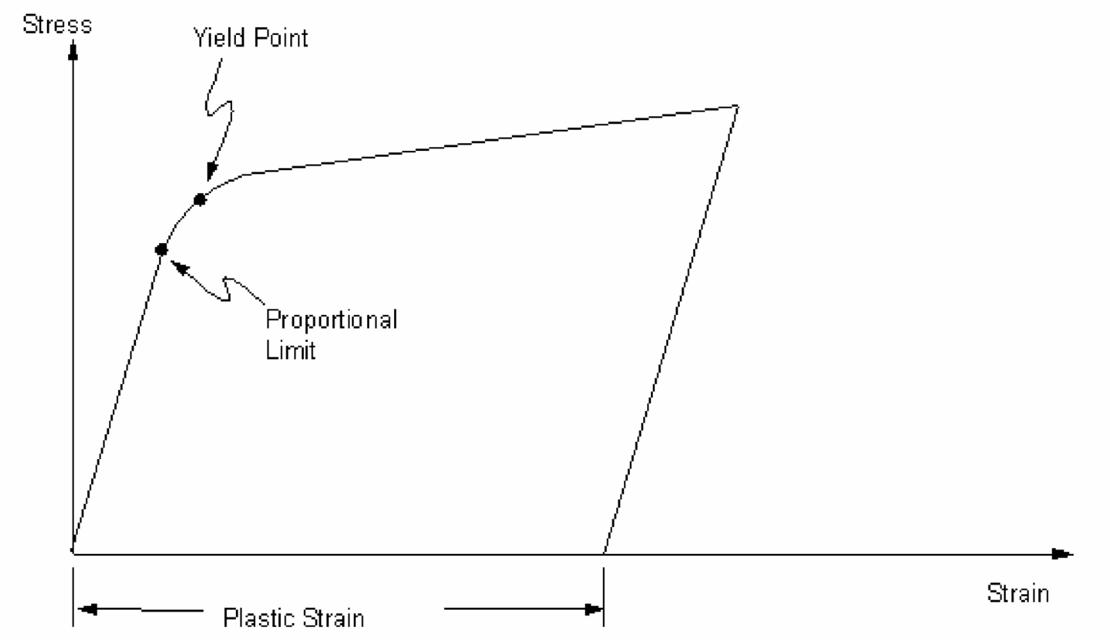

Figure 8: Stress vs Strain curve

3.2.3. Modeling Thermal Strain

The expansion of a material due to temperature is given by the expression:

$$L = L_o \left[1 + \alpha \Delta T \right]$$

where

$$\Delta T = \left(T - T_{ref} \right)$$

The resulting strain is given by:

$$\varepsilon_{th} = \frac{L - L_o}{L_o}$$

Thus, for an isotropic material, the thermal strain matrix is given by the relation:

$$\begin{Bmatrix} \varepsilon_{th,1} \\ \varepsilon_{th,2} \\ \varepsilon_{th,3} \\ \varepsilon_{th,4} \\ \varepsilon_{th,5} \\ \varepsilon_{th,6} \end{Bmatrix} = \begin{Bmatrix} \alpha \Delta T \\ \alpha \Delta T \\ \alpha \Delta T \\ 0 \\ 0 \\ 0 \end{Bmatrix}$$

There is no shear strain because of the isotropic nature of the material.

The total strain is the sum of the thermal and mechanical strains:

$$\left\{ \varepsilon_T \right\} = \left\{ \varepsilon \right\} + \left\{ \varepsilon_{th} \right\}$$

or $$\left\{ \varepsilon_T \right\} = \left\{ D \right\}^{-1} \left\{ \sigma \right\} + \left\{ \varepsilon_{th} \right\}$$

rearranging

$$\{\sigma\}=\{D\}\left[\{\varepsilon_T\}-\{\varepsilon_{th}\}\right]$$

This equation provides a relation between the stress and strains. The thermal strain can be calculated based on the temperature difference. The total strain can be expressed as a function of the displacements as shown below.

3.2.4. Modeling Strain-Displacement Relations

The strain-displacement relations are known as the compatibility equations:

$$\{\varepsilon_T\}=\{B\}\{d\}$$

or

$$\begin{Bmatrix}\varepsilon_1\\\varepsilon_2\\\varepsilon_3\\\varepsilon_4\\\varepsilon_5\\\varepsilon_6\end{Bmatrix}=\begin{bmatrix}\frac{\partial}{\partial x} & 0 & 0\\ 0 & \frac{\partial}{\partial y} & 0\\ 0 & 0 & \frac{\partial}{\partial z}\\ \frac{\partial}{\partial y} & \frac{\partial}{\partial x} & 0\\ \frac{\partial}{\partial z} & 0 & \frac{\partial}{\partial x}\\ 0 & \frac{\partial}{\partial z} & \frac{\partial}{\partial y}\end{bmatrix}\begin{Bmatrix}d_x\\d_y\\d_z\end{Bmatrix}$$

where d_x, d_y and d_z are the displacements in the x, y and z-direction respectively.

3.2.5. Initial and Boundary Conditions for Stress and Displacement Equations

Our problem is symmetric about the xz-plane. Therefore, we can carry out our analysis by modeling only half of the domain. The only boundary condition is the symmetry condition about the xz-plane:

At y = 0: $$\frac{\partial \sigma}{\partial y} = 0$$

Initially, stress and displacement values throughout the domain are assumed to be zero.

At t=0: $$\begin{aligned} \sigma &= 0 \\ d_x &= 0 \\ d_y &= 0 \\ d_z &= 0 \end{aligned}$$

3.2.6. Finite Element Modeling

To derive the finite element formulation for this problem we can use the principle of minimum total potential energy. The principle of minimum potential energy is a substitute to the equations of force equilibrium of an elastic body. However, the use of this method is limited and cannot be used for models other than the elastic material model.

The Potential Energy per unit volume due to mechanical strain is given by:

$$e_o = \frac{1}{2} \times stress \times mechanical\ strain$$

$$e_o = \frac{1}{2} \times \{\sigma\}^T \left[\{\varepsilon_T\} - \{\varepsilon_{th}\}\right]$$

But

$$\{\sigma\}^T = \left[\{\varepsilon_T\} - \{\varepsilon_{th}\}\right]^T \{D\}^T$$

Since D is symmetric, $\{D\}^T = \{D\}$

Therefore,

$$e_o = \frac{1}{2} \times \left[\{\varepsilon_T\} - \{\varepsilon_{th}\}\right]^T \{D\} \left[\{\varepsilon_T\} - \{\varepsilon_{th}\}\right]$$

or

$$e_o = \frac{1}{2} \times \left[\{B\}\{d\} - \{\varepsilon_{th}\}\right]^T \{D\} \left[\{B\}\{d\} - \{\varepsilon_{th}\}\right]$$
$$e_o = \frac{1}{2} \times \left[\{d\}^T \{B\}^T - \{\varepsilon_{th}\}^T\right] \{D\} \left[\{B\}\{d\} - \{\varepsilon_{th}\}\right]$$

Total PE is given by:

$$E = \int e_o dV$$

$$\begin{aligned} E &= \frac{1}{2}\times\int\left[\{d\}^T\{B\}^T-\{\varepsilon_{th}\}^T\right]\{D\}\left[\{B\}\{d\}-\{\varepsilon_{th}\}\right]dV \\ &= \frac{1}{2}\times\int\left[\{d\}^T\{B\}^T\{D\}[B]\{d\}\right]dV+\int\left[\{d\}^T\{B\}^T\{D\}\{\varepsilon_{th}\}\right]dV+\frac{1}{2}\int\{\varepsilon_{th}\}^T\{D\}\{\varepsilon_{th}\}dV \end{aligned}$$

To minimize the PE, we equate its derivative with respect to the degree of freedom to zero:

$$\begin{gathered} \frac{\partial E}{\partial\{d\}}=0 \\ \frac{1}{2}\int\left[\{B\}^T\{D\}\{B\}\{d\}\right]dV+\int\left[\{B\}^T\{D\}\{\varepsilon_{th}\}\right]dV=0 \\ \frac{1}{2}\int\left[\{B\}^T\{D\}\{B\}\right]dV\{d\}=-\int\left[\{B\}^T\{D\}\{\varepsilon_{th}\}\right]dV \end{gathered}$$

or

$$\{k\}\{d\}=\{f_{th}\}$$

By applying this formulation over the discretised subdomains, we obtain the submatrices. The global stiffness matrix can then be assembled and solved.

CHAPTER # 4

RESULTS AND DISCUSSIONS

4.1. EFFECT OF SCANNING SPEED

Figure (9) shows temporal variation of surface temperature at the irradiated spot center for various laser scanning speeds and two laser pulse parameters. The solid phase heating, melting, and the liquid phase heating are evident for the laser pulse parameter β = 0. This is true for all laser scanning speeds and laser pulse parameters considered in the simulations. However workpiece surface does not undergo melting at the irradiated spot centre on the surface for all laser scanning speeds, since temperature remains below the melting temperature of the substrate material. This is associated with the laser pulse intensity distribution at the irradiated spot centre, which is less than that corresponding to the Gaussian distribution (β = 0). Moreover, temperature difference between the maximum and the minimum temperatures is considerably small for β = 1 as compared to that of β = 0 due to laser power intensity at the irradiated spot center. However, the phase change is evident for β = 0; in which case temperature remains almost the same with time during the phase change. The liquid phase heating results in further increase in temperature from the melting temperature in the pulse. This appears as a temperature peak at the surface during the heating pulse. However, melting and liquid phase heating starts within the fourth pulse.

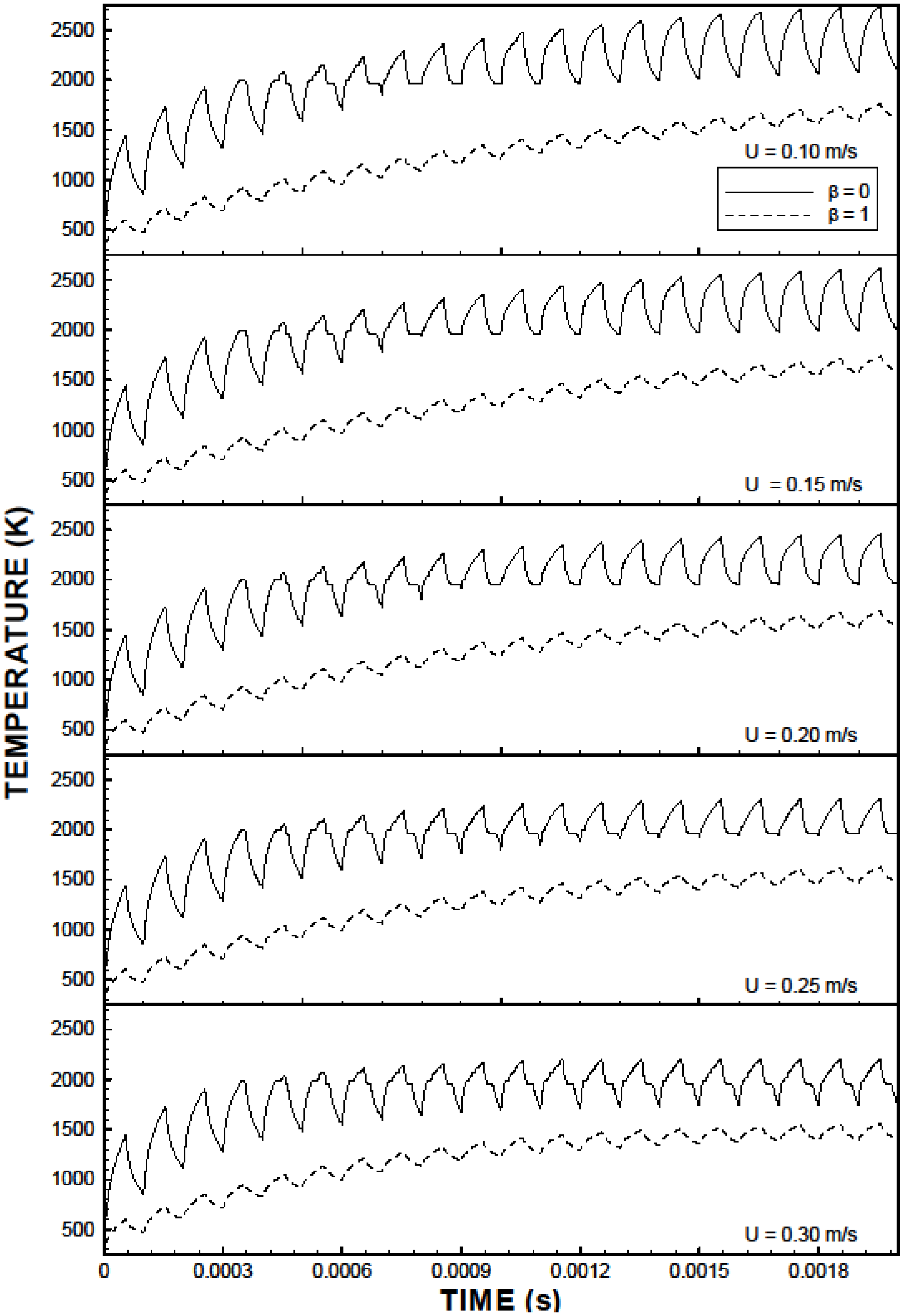

Figure 9: Temporal variation of temperature at the irradiated spot center for Titanium

As the scanning speed increases, the temporal location of liquid phase heating moves further towards the pulse ending. This is associated with the energy absorbed from the irradiated field during each pulse of the repetitive pulses; in which case, increasing laser scanning speed lowers the rate of energy deposited in the surface vicinity of the workpiece. As the number of pulses increase temperature at the surface becomes higher than the melting temperature during the heating and cooling cycle of each pulse. This takes place after the 7th pulse for laser scanning speed 0.1 m/s. However, this situation occurs at different pulse number for laser scanning speed less than $U \leq 0.25$ m/s. Melting, liquid phase heating, and subsequent solidification takes place after the 7th pulse for laser scanning speed 0.30 m/s. The close examination of rate of temperature rise and fall for the last pulse (20th pulse) reveals that the ratio of temperature rise is slower than the rate of fall. This is attributed to the liquid phase heating and heat transfer from the liquid zone to the solid bulk in the laser irradiated region, which is higher in the heating pulse as compared to the cooling period following the pulse. When comparing the difference of temperature rise and fall during the solid phase heating and during the liquid phase heating (Figure (9)), it is evident that temperature rise is faster during solid heating ($2.0\text{x}10^{-4} \leq t \leq 2.5\text{x}10^{-4}$ s) for consecutive pulse number 3 than that corresponding to the liquid phase heating ($19\text{x}10^{-4} \leq t \leq 19.5\text{x}10^{-4}$ s) for consecutive pulse number 20 due to laser scanning speed 0.15 m/s. This is associated with the rate of energy dissipation due to phase change below the melt pool depth, which suppresses the rate of temperature rise in the liquid phase for pulse number 20.

Figures (10) and (11) show melt pool size and Maragoni flow in the melt pool for different laser scanning speeds and for two laser pulse parameters, respectively. In the

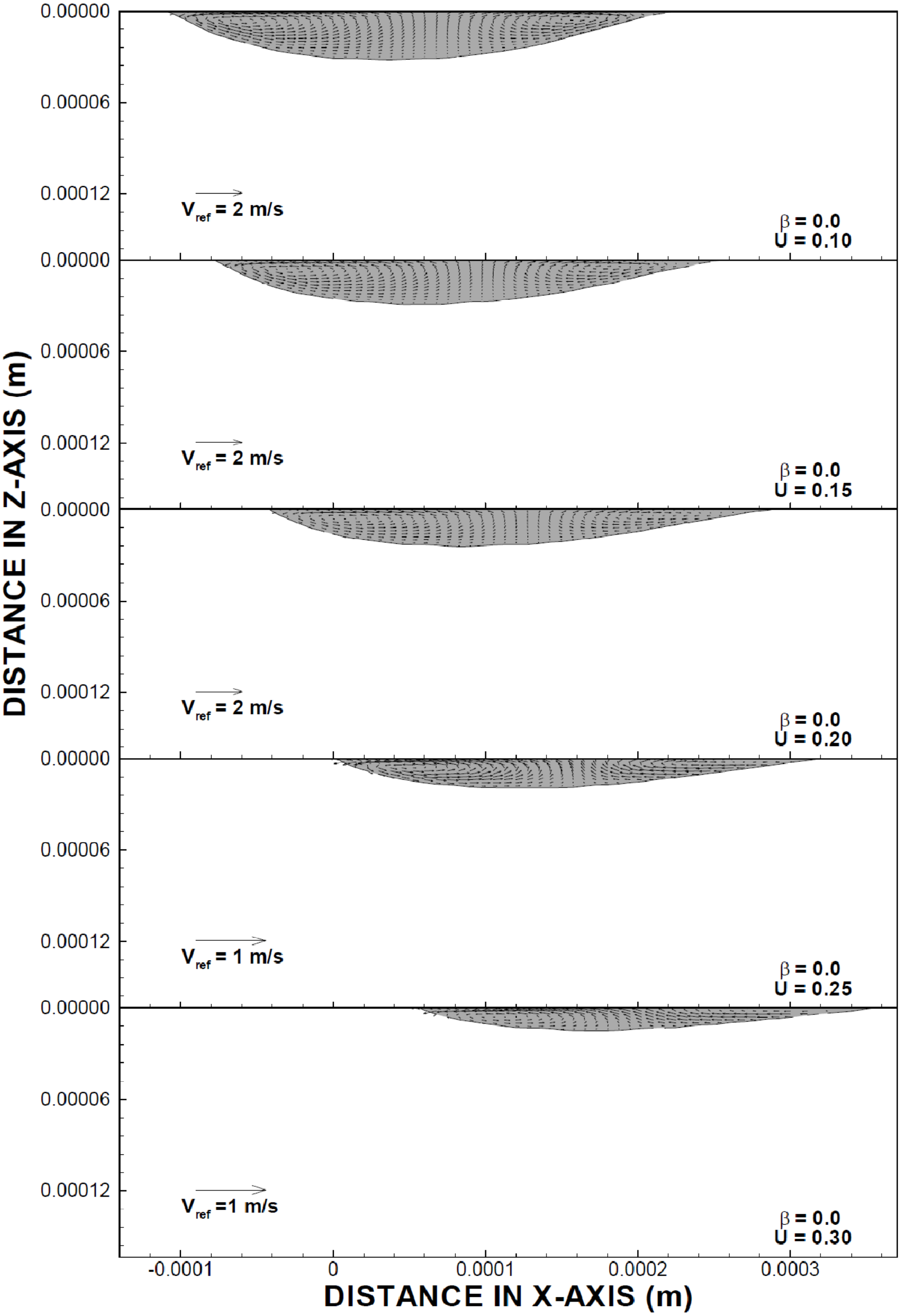

Figure 10: Marangoni flow in the melt pool for laser pulse parameter β = 0.0

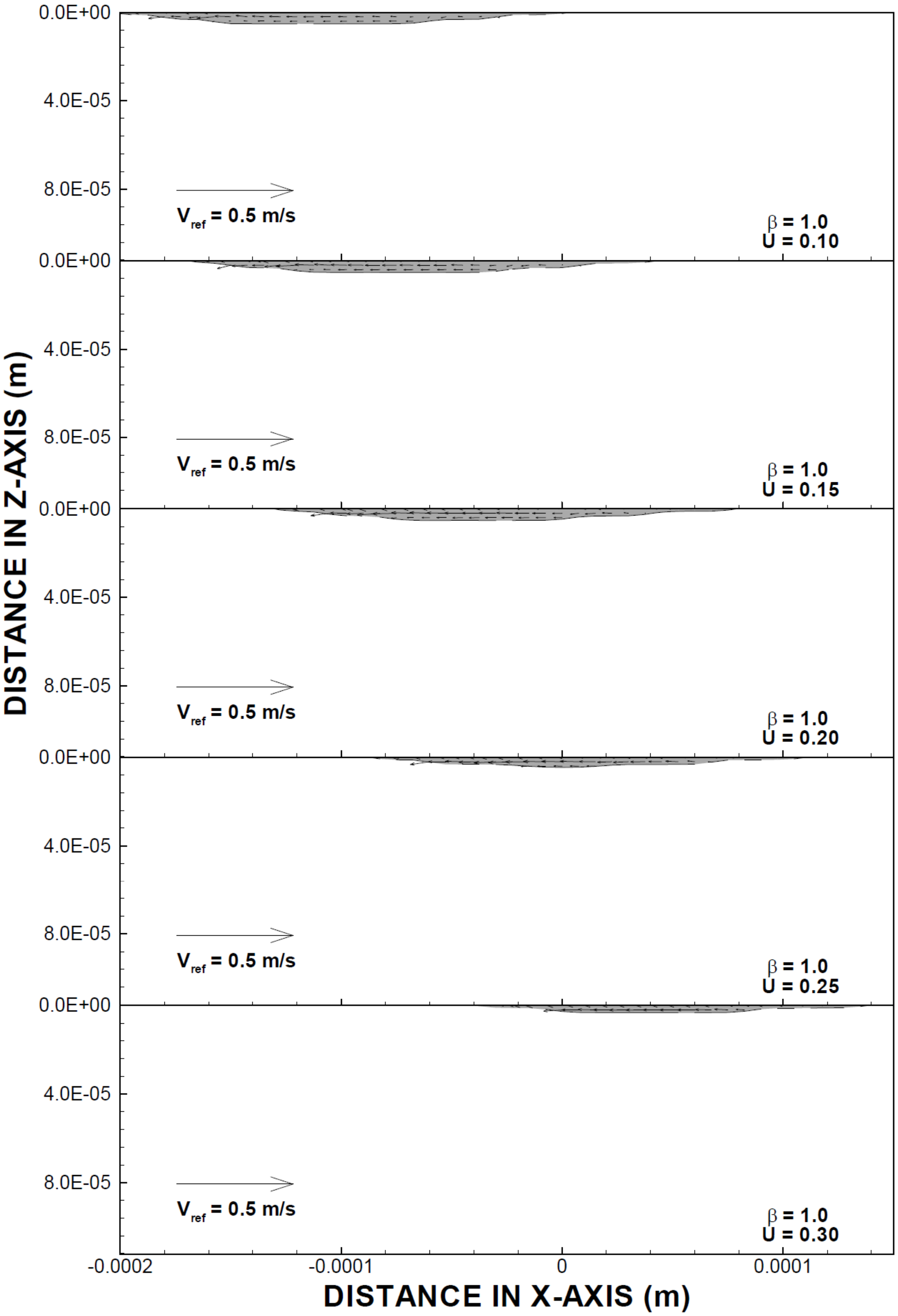

Figure 11: Marangoni flow in the melt pool for laser pulse parameter β = 1.0

case of laser pulse parameter β = 0, the melt pool geometry extends along the x-axis, which corresponds to the laser beam scanning direction. In this case, the thinning of the melt pool depth appears like tail, which takes place in the direction opposite to the laser scanning direction. The maximum melt pool depth occurs for low laser scanning speed (0.1 m/s) and melt pool depth reduces with increasing laser scanning speed. In addition, the location of melt pool changes along the x-axis due to the laser scanning speed. Two counter rotating circulation cells are formed in the melt pool due to Marangoni flow. Since the melt pool is not in symmetry along z-axis, the size of the circulation cell differs in the melt pool. The maximum flow velocity is higher in the melt pool for laser scanning speed 0.1 m/s, which is associated with the depth of the melt pool and the surface tension gradient at the surface.

The top view of the melt pool (x, y-plane) and the flow direction is shown in figure (12) for different laser scanning speeds and the laser pulse parameter β = 0. The shape of the melt pool changes as the laser scanning speed increases. This is more pronounced for 0.3 m/s. In addition, the flow field changes notably with increasing laser scanning speed. In general, the flow field is developed from center region of the melt pool surface towards the pool edges. This is attributed to the surface tension gradient, which increases towards the melt pool edges. In the case of laser parameter β = 1.0 (Figure (11)), melt pool depth along the z-axis becomes very shallow due to the laser power intensity, which is less than that of β = 0 (Figure (4)). In addition the solid heating takes place at the centre of the irradiated spot because of the less power intensity unable to result in melting. The solid material is present within the melt pool, which appears as

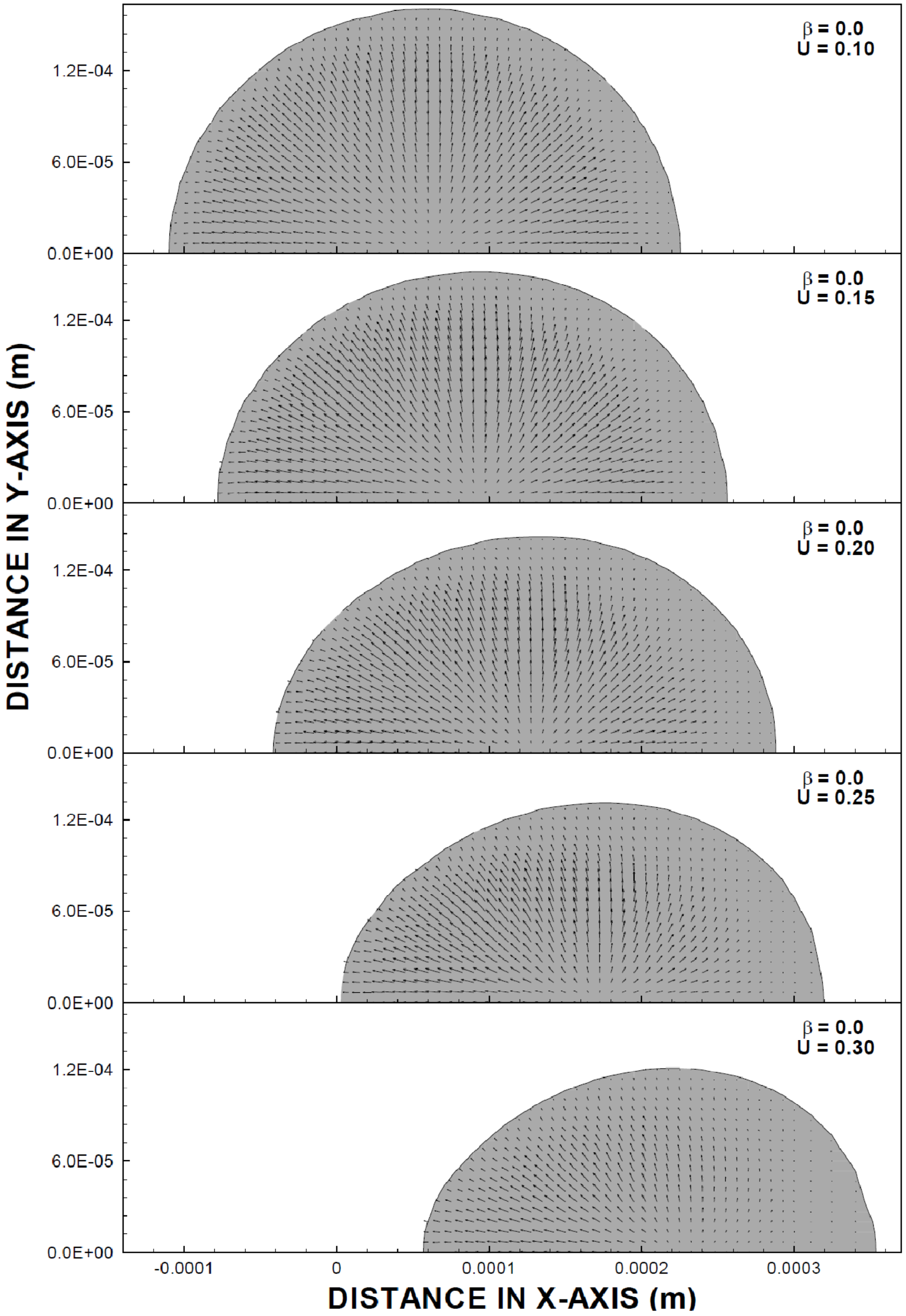

Figure 12: Top view of the melt pool for laser pulse parameter β = 0.0

two shallow melt pools forming in the surface vicinity. This situation can be seen from figure (13) in which the melt pool geometry in the x, y - plane is shown , as the laser scanning speed increases , the size of the solid phase in the irradiated spot surface increases while the size of the melt pool reduces. The flow direction in the melt pool differs significantly at the melt pool surface for the laser pulse parameter β = 1 than that of β = 0. This is attributed to the surface tension gradient $d\gamma/dT$ at the melt pool surface.

Figure (14) shows temperature contours across the symmetry plane (x, z-plane) for different laser scanning velocities and two laser pulse parameters at the end of 20th consecutive pulse. High temperature region extends into the substrate material for the laser pulse parameter β = 0 which is more pronounced for lower laser scanning speed (0.1 m/s). The size of the laser heated region is big at the center of the irradiated region and it becomes shallow in the region away from the irradiated spot center in the direction opposite to the laser scanning direction. In this case, the laser scanning results in extended heated region along the x-axis forming like a temperature tail behind the irradiated spot. This indicates the slow cooling rate in the region behind the laser irradiated spot which is more pronounced for high laser scanning speed (0.3 m/s). In the case of laser parameter β = 1, the size and shape of the heated region inside the workpiece changes from that corresponding to β = 0. This is associated with the laser pulse intensity distribution at the surface (Figure (4)) which follows the shifted Gaussian profile, $Exp\left[-\left(\beta+\left(x^2+y^2\right)/a^2\right)\right]$. The depth and the shape of the heated region change significantly for different laser scanning speeds. Moreover, a tail like heated region is formed for the high laser scanning speed (0.30 m/s).

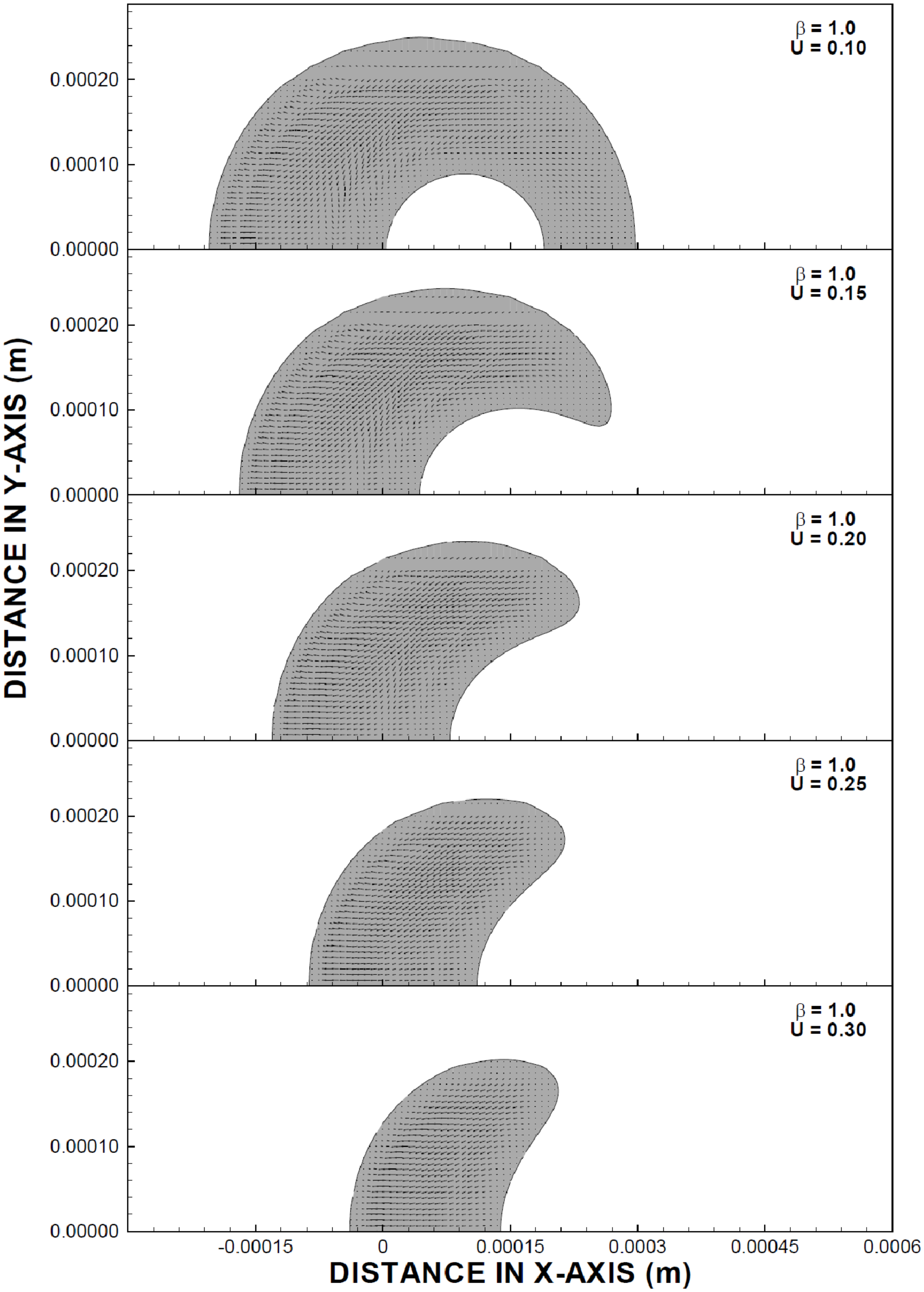

Figure 13: Top view of the melt pool for laser pulse parameter β = 1.0

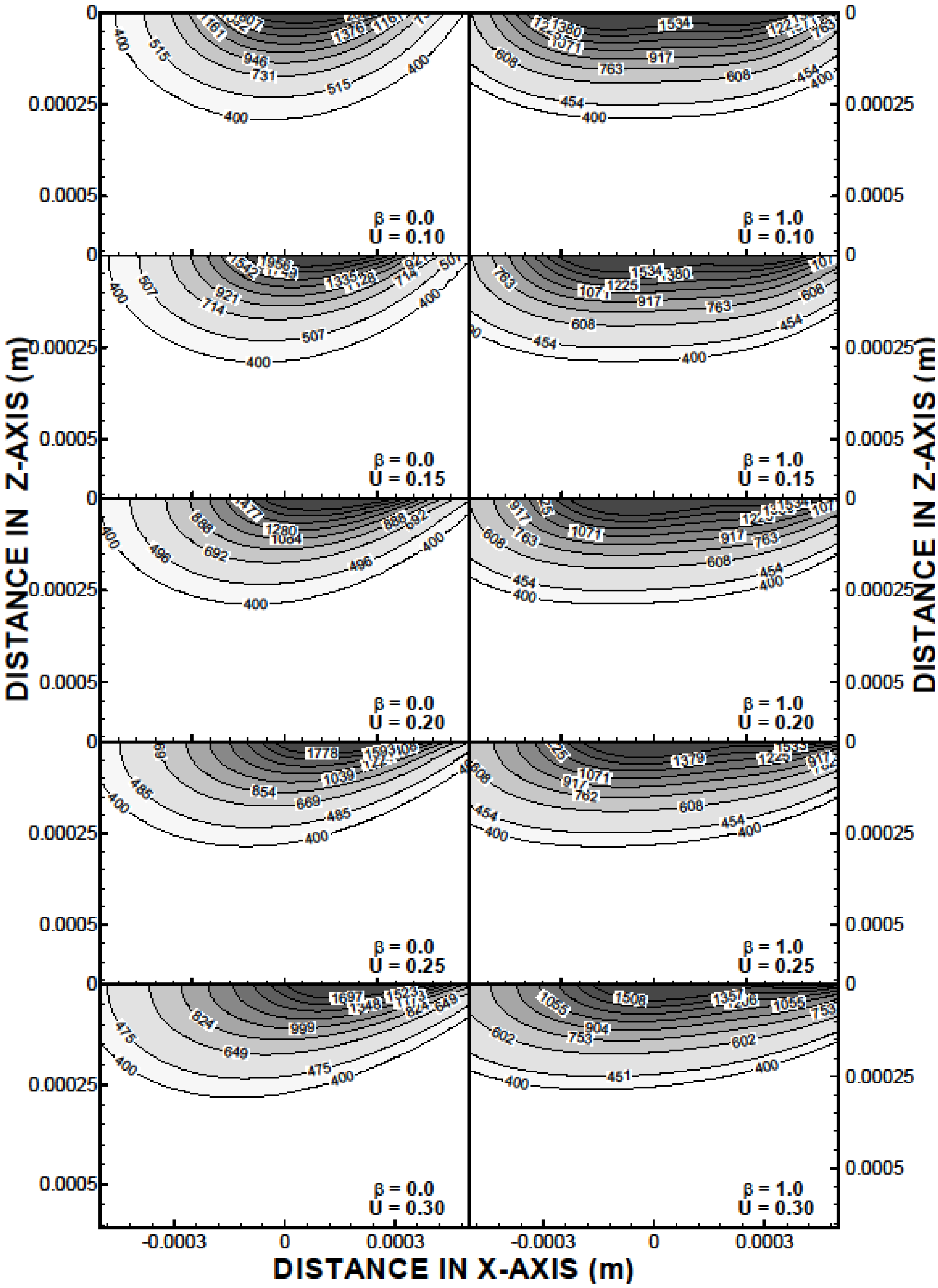

Figure 14: Temperature contours across the symmetry plane (x-z plane) at the end of 20th pulse.

Figure (15) shows temperature distribution along the x axis, for two laser scanning speeds and two laser pulse parameters at the end of the 20th heating pulse. It should be noted that x and y –axis locations are at the center of irradiated spot. Temperature attains well above the melting temperature of the substrate material at the surface for β = 0; in which case, the laser pulse intensity distribution at the surface is Gaussian. The liquid phase heating takes place in the vicinity of the surface and the melt region extends almost 50 μm below the surface. Temperature gradient changes within the vicinity of the melt pool wall where temperature reduces to the melting temperature of the substrate material. In this case, temperature decay is sharper in the melt pool as compared to the region corresponding to next to the melt pool. The sharp decay of temperature in the melt pool is associated with absorption of the laser energy from the irradiated field, which decays exponentially with increasing depth according to the Lamberts Law. However, increasing laser scanning speed reduces the peak temperature at the surface. In addition, the melt depth also reduces considerably in the surface region of the workpiece. Temperature decay in the solid phase decreases slightly with increasing depth below the surface.

It should be noted that heat conduction increases with increasing temperature gradient and heat conduction governs the energy transfer in the solid phase of the substrate material below the melt pool. Therefore, heat conduction towards the solid bulk reduces with increasing depth at the end of 20th heating pulse. In the case of the laser pulse parameter β = 1, the peak temperature at the surface reduces significantly due to low laser power intensity at the irradiated spot centre. The peak

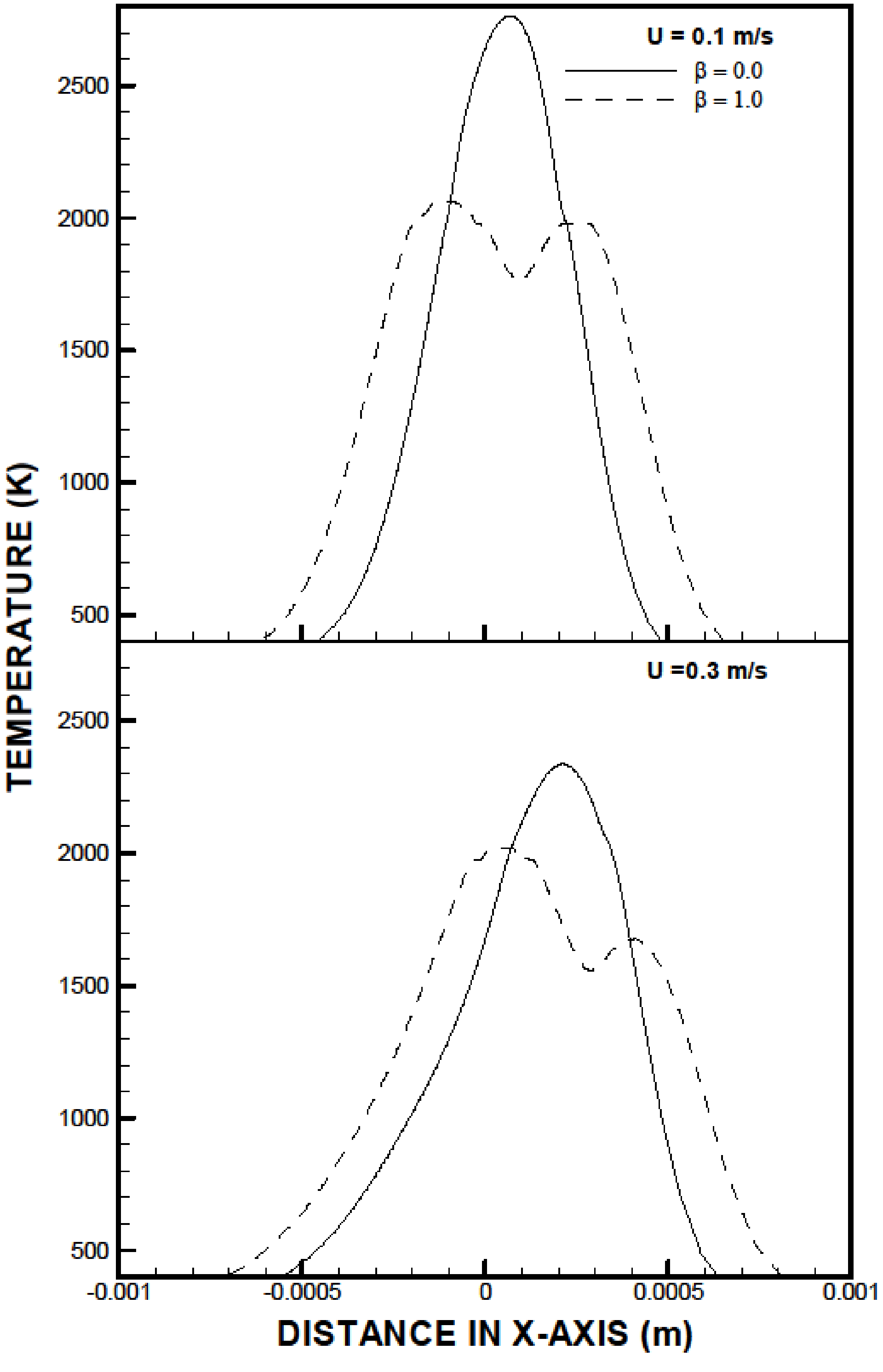

Figure 15: Temperature variation along the x-axis at the end of the 20th pulse.

temperature reduces further with increasing laser scanning speed (0.3 m/s) because of the rate of energy deposited into the substrate material which reduces with increasing scanning speed.

Figure (16) shows temperature distribution along the y axis for two laser scanning speeds and two laser pulse parameters. The x and z axes locations correspond to the irradiated spot center. The melt size along the y axis is notable for the laser pulse parameter $\beta = 0$ for two laser speeds, i.e. temperature remains almost the same across the solid and the melt zone where the mushy zone is generated. The width of the melt pool along the y axis is the order of 180 μm for low laser scanning speed (0.1 m/s), but it is 100 μm for the laser scanning speed of 0.3 m/s for $\beta = 0$. It should be noted that the laser beam diameter at the surface is about 600 μm. Due to the Gaussian distribution of the laser beam intensity at the surface, almost 2/3rd of the laser irradiated spot is melted for the laser scanning speed 0.1 m/s while 1/3rd of the laser irradiated spot is melted for scanning speed 0.3m/s. This indicates that the influence of the laser scanning speed has significant effect on the melt width at the workpiece surface. Temperature decay in the irradiated spot center follows almost the Gaussian distribution because of the laser pulse intensity distribution at the surface for $\beta = 0$.

In the case of $\beta = 1$, temperature profile follows almost the laser pulse intensity distribution at the surface (Figure (4)). However, at low laser scanning speed (0.1 m/s), melting occurs at the surface where laser intensity is high. However, the liquid phase heating in the melt pool is unlikely, since the peak temperature at the surface is slightly higher than the melting temperature of the substrate material.

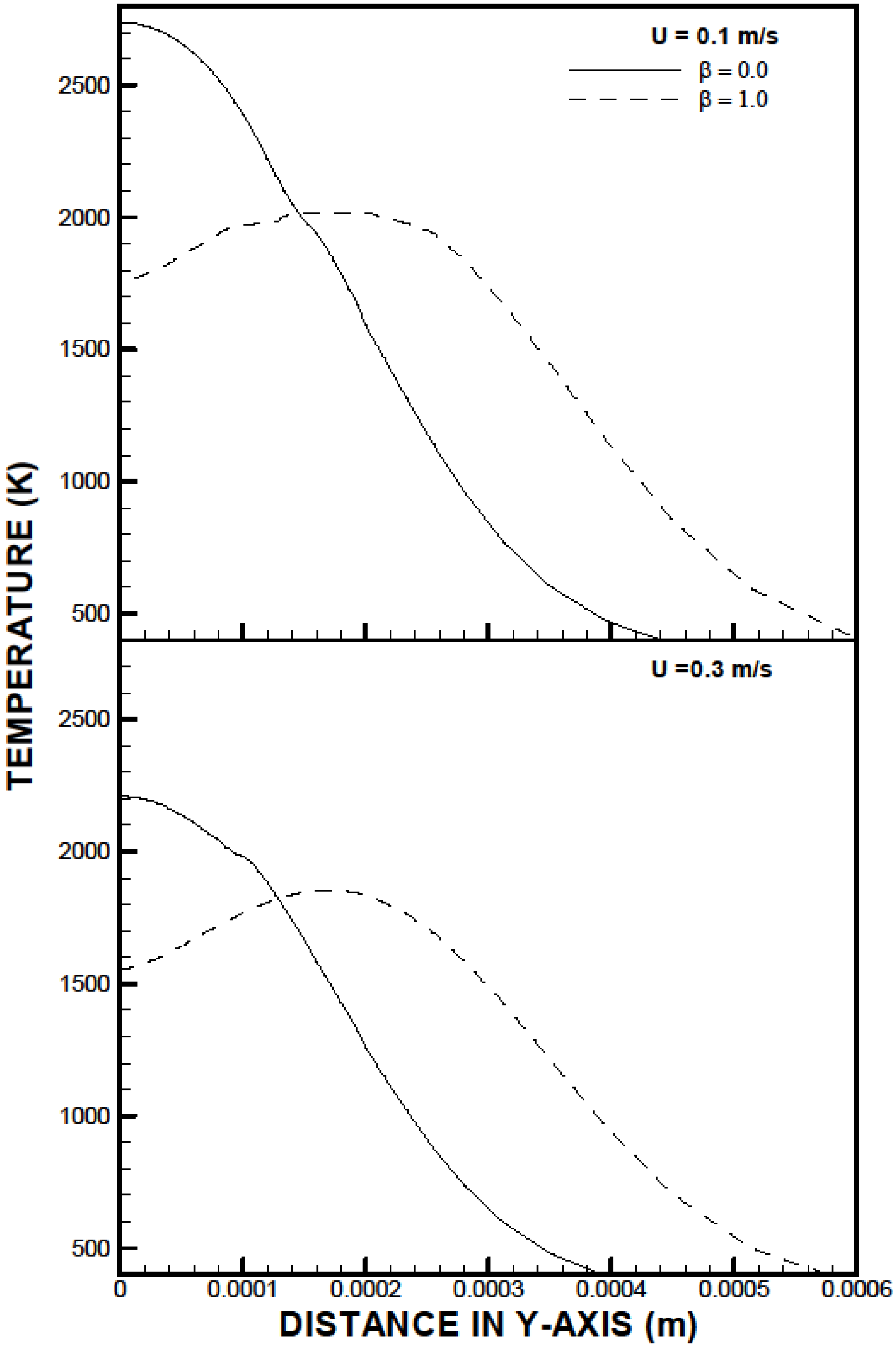

Figure 16: Temperature variation along the y-axis at the end of the 20th pulse

4.2. EFFECT OF LASER PULSE PARAMETER

Figure (17), shows surface temperature distributions along the y-axis for different values of the laser pulse parameter (β) and two laser scanning speeds. The peak temperature at the irradiated surface reduces with increasing values of the laser pulse parameter. This is associated with the laser pulse intensity distributions at the surface, which reduces at the irradiated spot center with increasing laser pulse parameter (Figure (4)). Although the surface temperature distributions almost follows the laser pulse intensity distributions for different laser pulse parameters, the phase change and the liquid phase heating modifies surface temperature behavior. Temperature exceeds the melting temperature of the substrate material in the laser irradiated region for the laser pulse parameter $\beta = 0$, which is Gaussian. Temperature difference between the beginning and the end of the last pulse is high for high values of the laser pulse parameter. This is attributed to the heating rate, which reduces with increasing pulse parameter due to reducing peak laser pulse intensity. The mushy zone formation between the liquid and solid phases is only notable across the mushy zone. Since, the mushy zone size is considerably small, the presence of this zone is not visible for all laser parameters such as $\beta = 1$ for laser scanning speed of 0.1 m/s. The presence of the formation of mushy zone is not pronounced for the last pulse beginning. This is because of the heat dissipation from the melt pool to its neighborhood. Once the laser pulse intensity ends, internal energy gained by the liquid phase in the melt pool ends and cooling in the melt pool through conduction and convection reduces the melt pool size slightly while enhancing the mushy zone size around the melt pool.

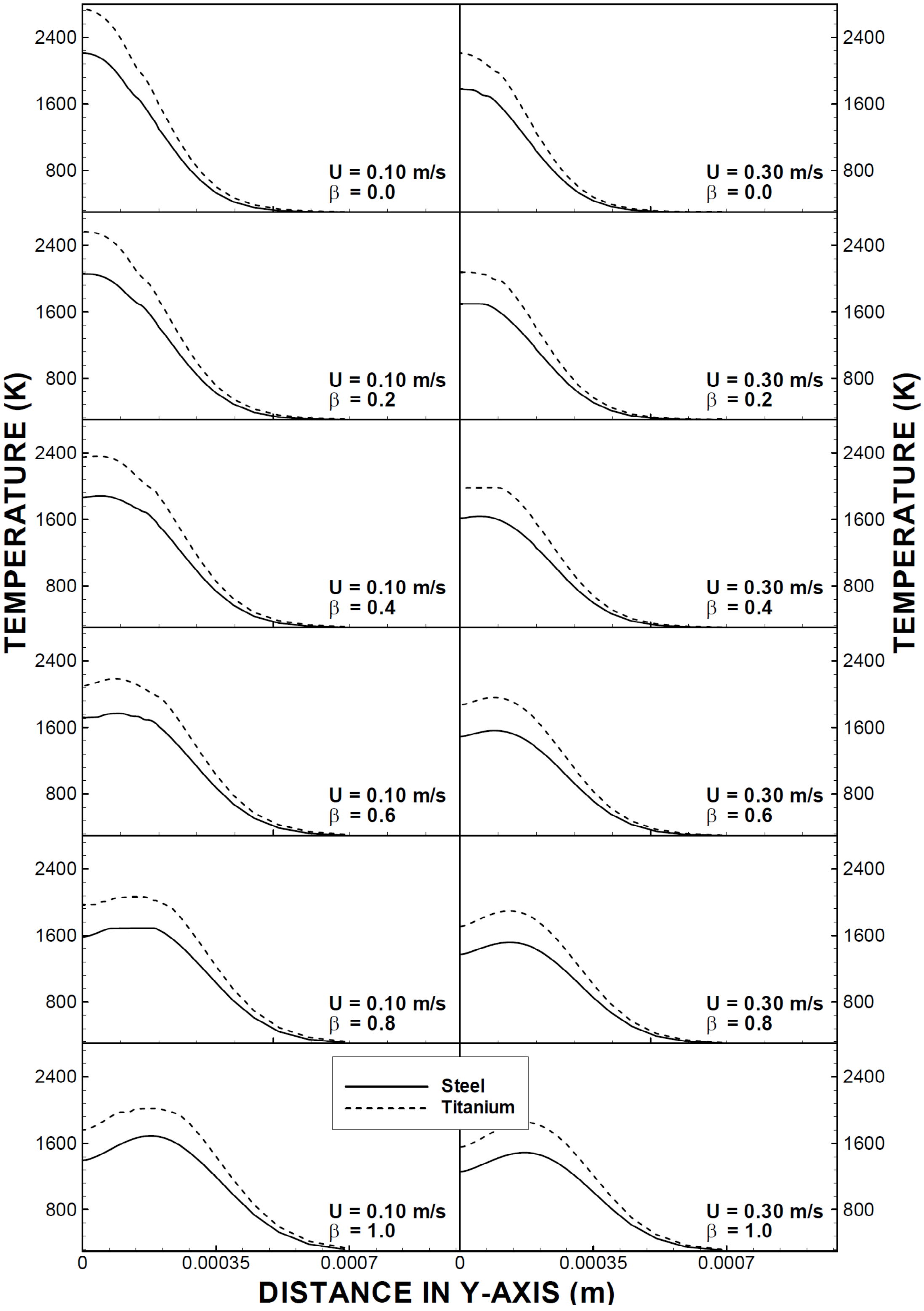

Figure 17: Variation of temperature along y-axis for Steel and Titanium at different laser pulse parameters and two laser scanning speeds

When comparing the influence of laser scanning speed on temperature profiles, it can be observed that increasing laser scanning speed reduces the peak temperature at the surface. In this case the rate of energy deposited by the laser beam into the workpiece reduces for high laser scanning speeds resulting in reduced temperature at the irradiated surface.

Figure (18), shows temperature distribution inside the substrate material for different values of the laser pulse parameter and two laser scanning speeds. Temperature decay is sharp in the surface vicinity and as the depth below the surface increases, it becomes gradual. The sharp decay of temperature in the surface region is more pronounced for small values of the laser pulse parameter. This is associated with the energy gain by the irradiated field in the surface region, which is high for small values of β. Consequently, this results in sharp change in temperature distributions in the vicinity of the surface. In addition, liquid phase heating in the surface region contributes to the sharp decay of temperature in the surface region. Moreover increasing laser pulse parameter lowers the temperature gradient below the surface, which is attributed to the less energy absorbed from the irradiated region. When comparing titanium with steel, it is evident that titanium results high temperature in the substrate material. This is attributed to the low thermal diffusivity of titanium which in turn results in relatively higher temperature than inside the steel substrate.

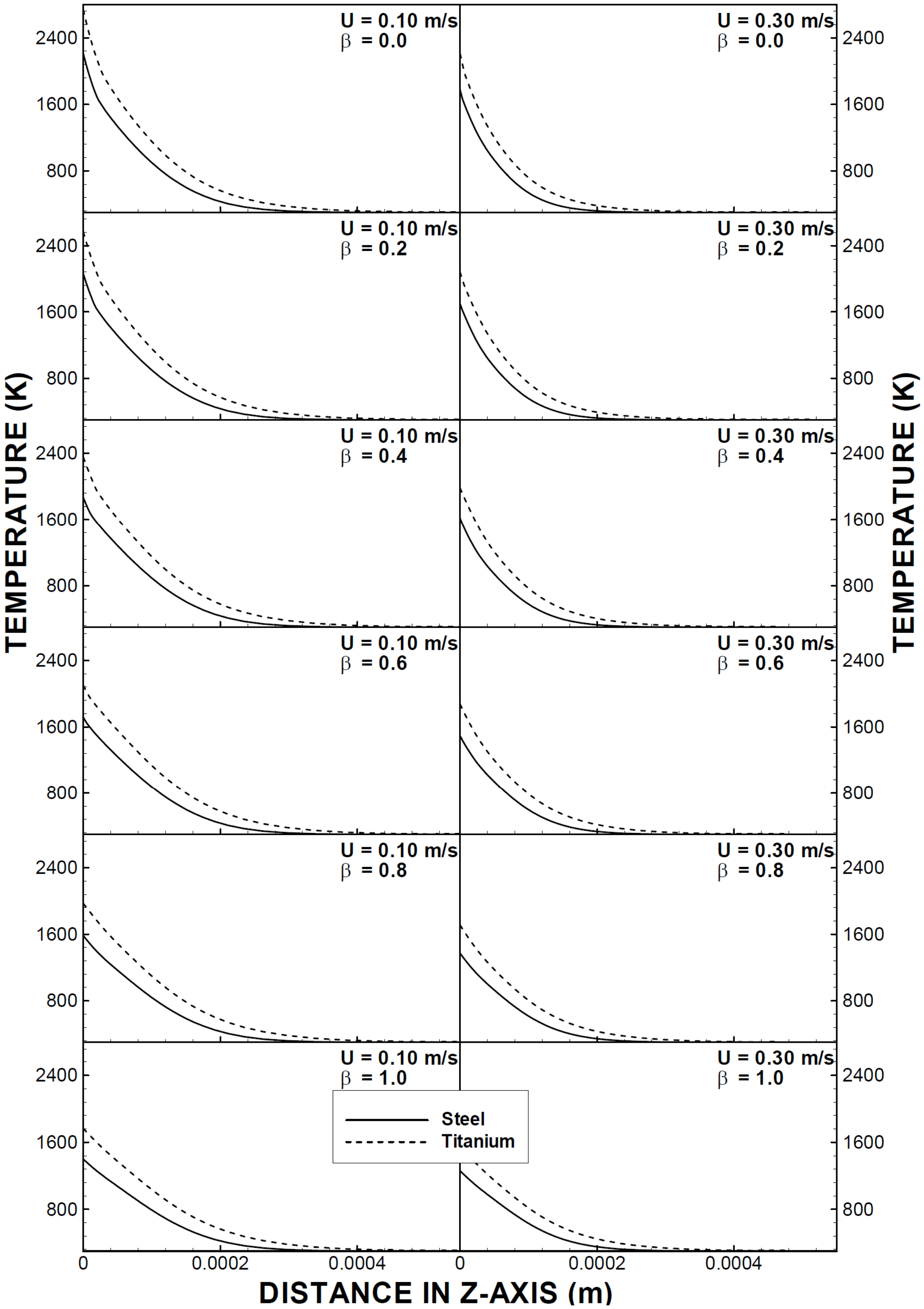

Figure 18: Variation of temperature along z-axis for Steel and Titanium at different laser pulse parameters and two laser scanning speeds.

In the case of steel (Figure (18)), temperature remains below the melting temperature at the irradiated spot center for increasing laser pulse parameter, which is more pronounced for $\beta \geq 0.8$. Laser scanning speed has considerable effect on the peak surface temperature which reduces with increasing speed. This effect is more visible for the laser pulse parameter $\beta = 0$. In this case, laser intensity at the irradiated spot center causes high rate of energy deposition into the substrate material at low laser scanning speeds. However, temperature behavior along the x-axis is almost the same for two scanning speeds.

Figures (19) and (20) show three dimensional plot of temporal variation of surface temperature with laser pulse parameter for two laser scanning speeds, and titanium and steel, respectively. It is evident that increasing laser pulse parameter results in reducing surface temperature at the irradiated spot center. Temperature appears as spikes along each pulse and once the melting occurs, the rise of peak temperatures due to each pulse remains almost the same. This is because of the energy consumed during the melting, which lowers temperature rise at the surface. The influence of laser scanning speed on peak temperature is considerable, particularly in the early heating period, which is more pronounced for small values of laser pulse parameter. The phase change is visible for heating periods between $0.4 < t < 0.8$ ms corresponding to laser scanning speed 0.3 m/s and $\beta = 0$ for titanium. In this case, the rapid rise of temperature peak is observed in the liquid phase. This occurs slightly earlier for low value of laser scanning speeds 0.1 m/s. In the case of steel (Figure (20)), temperature behavior is similar to that corresponding to titanium provided that peak value of temperature remains slightly lower than that of of titanium, which is lower than that of steel (Figures (3) and (4)).

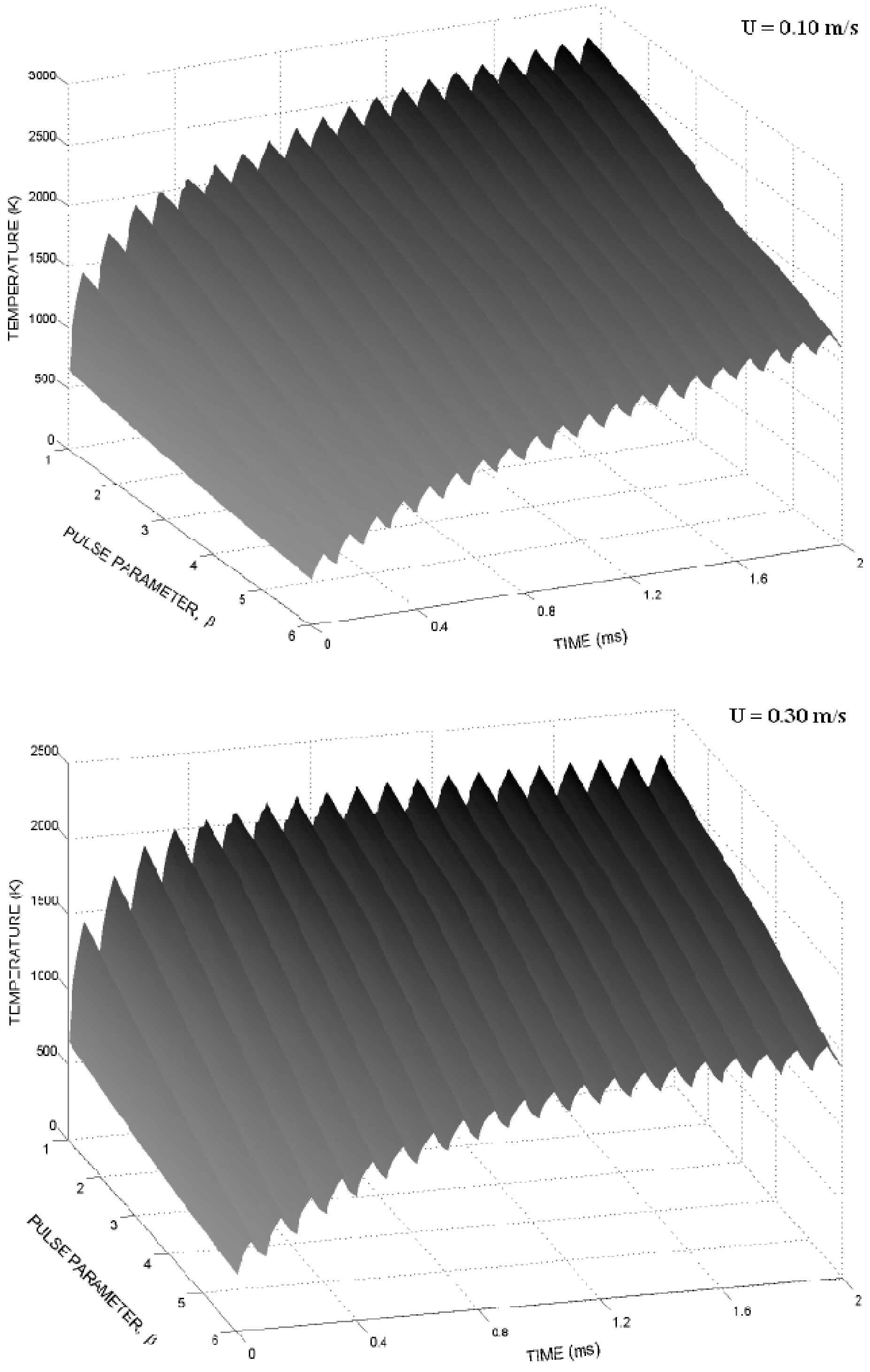

Figure 19: Temporal variation of temperature with laser pulse parameter at titanium surface for two laser scanning speeds

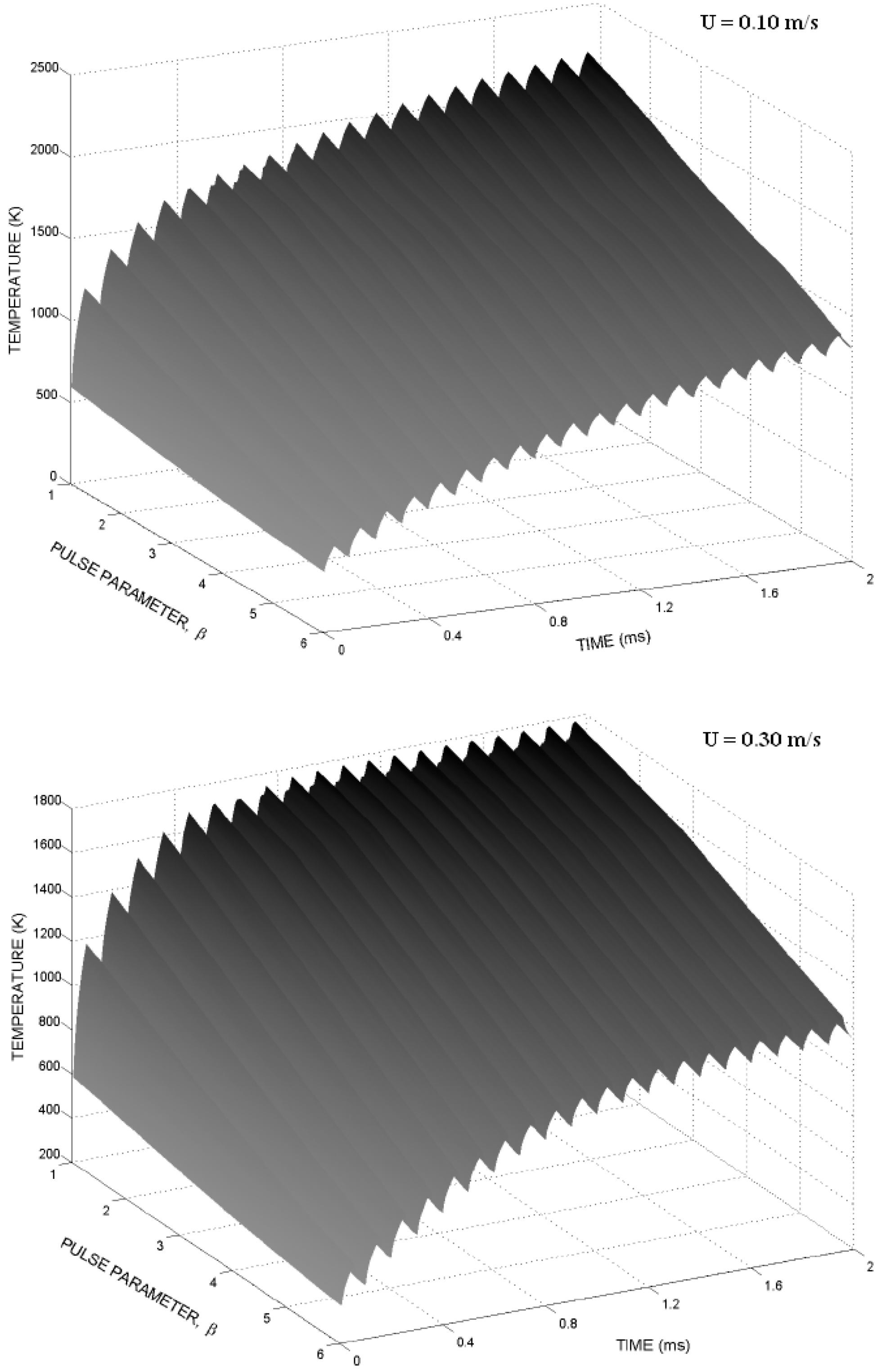

Figure 20: Temporal variation of temperature with laser pulse parameter at Steel surface for two laser scanning speeds.

Figure (21) shows surface temperature variation along the x-axis for different values of laser pulse parameter, two values of laser scanning speeds and titanium and steel. The y-axis location is y = 0 and the heating time corresponds to the end of the 20th pulse. Temperature almost follows the laser pulse intensity distribution at the workpiece surface for small values of the laser pulse parameter and low laser scanning speeds. Peak temperature exceeds the melting temperature of the substrates for the laser pulse parameter $0 \leq \beta \leq 0.6$, which is true for laser scanning speed 0.1 m/s. However, as the laser parameter increases further peak temperature reduces below the melting temperature of steel. In this case, solid phase heating takes place at the workpiece surface. The influence of laser intensity on temperature distribution along the x-axis is more pronounced for the laser pulse parameter $\beta \geq 0.6$. In this case, two temperature peaks are observed at the surface. The first temperature peak is slightly higher than the second peak. This is attributed to the laser scanning speed which results in less energy deposited in the frontal region of the irradiated spot center. This situation becomes more visible for high laser scanning speeds 0.3 m/s. However, melting along the x-axis causes abrupt changes in temperature profile at melting temperature. Temperature behavior due to titanium and steel workpieces is almost the same, provided that the peak temperature is less for steel due to higher thermal diffusivity as compared to titanium.

Figures (22) and (23) show melt pool geometry and flow field at the melt pool surface (x and y-plane) for different laser pulse parameters and two laser scanning speeds. Figure (22) is for titanium and figure (23) is for steel. The heating duration is at

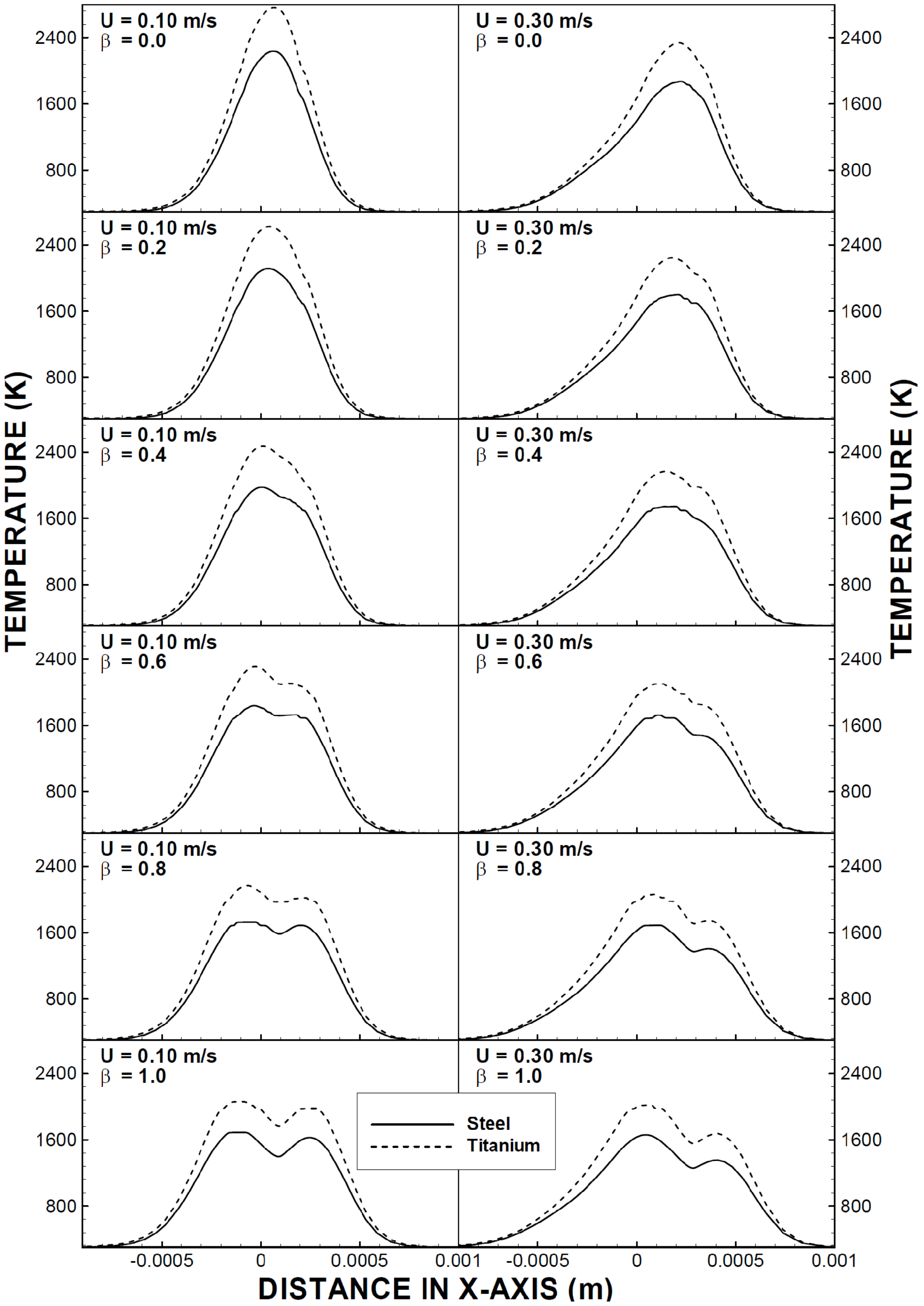

Figure 21: Variation of temperature along x-axis for Steel and Titanium at different laser pulse parameters and two laser scanning speeds

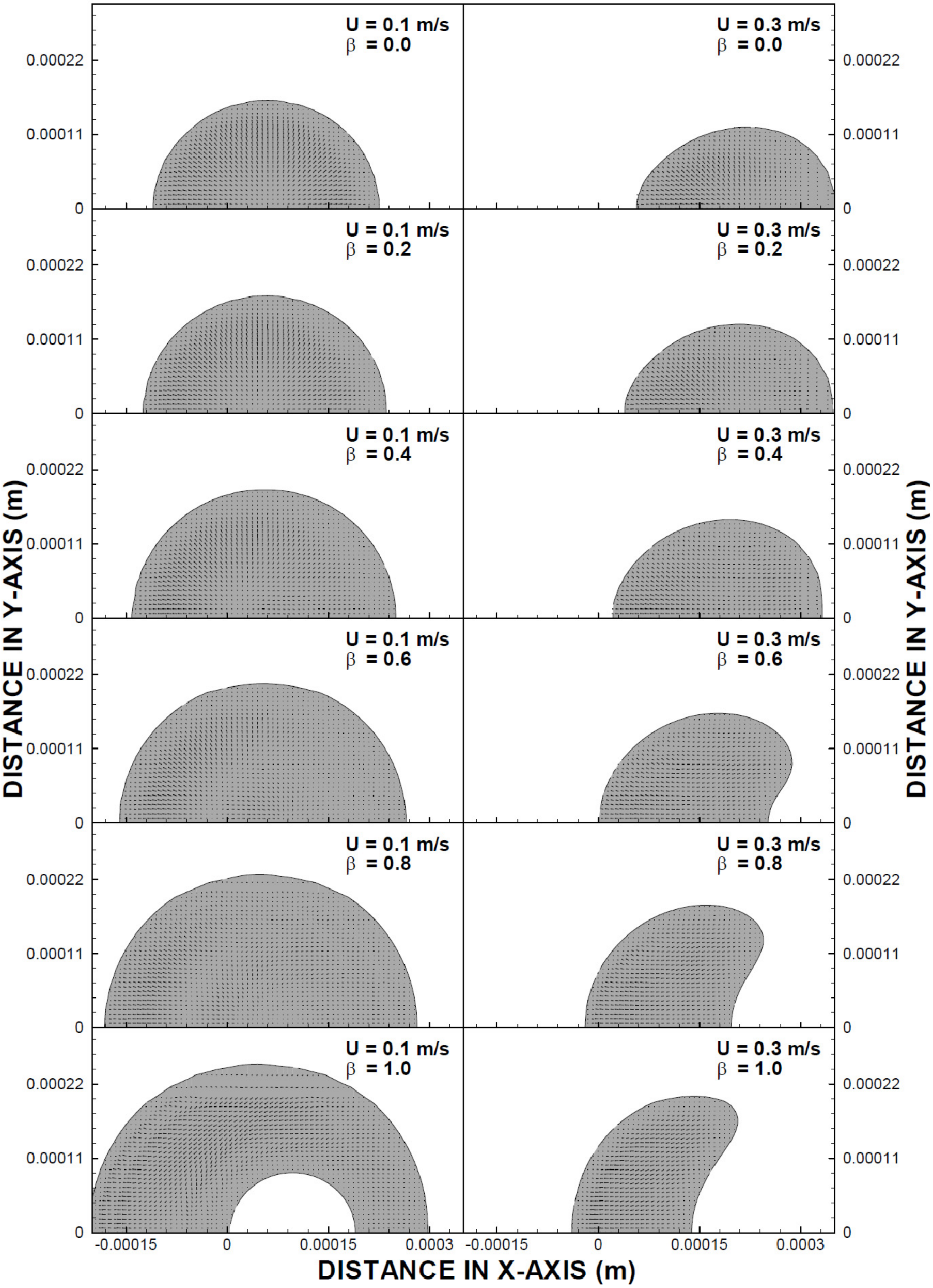

Figure 22: Melt pool in x,y-plane at Titanium surface for different laser pulse parameters and two laser scanning speeds

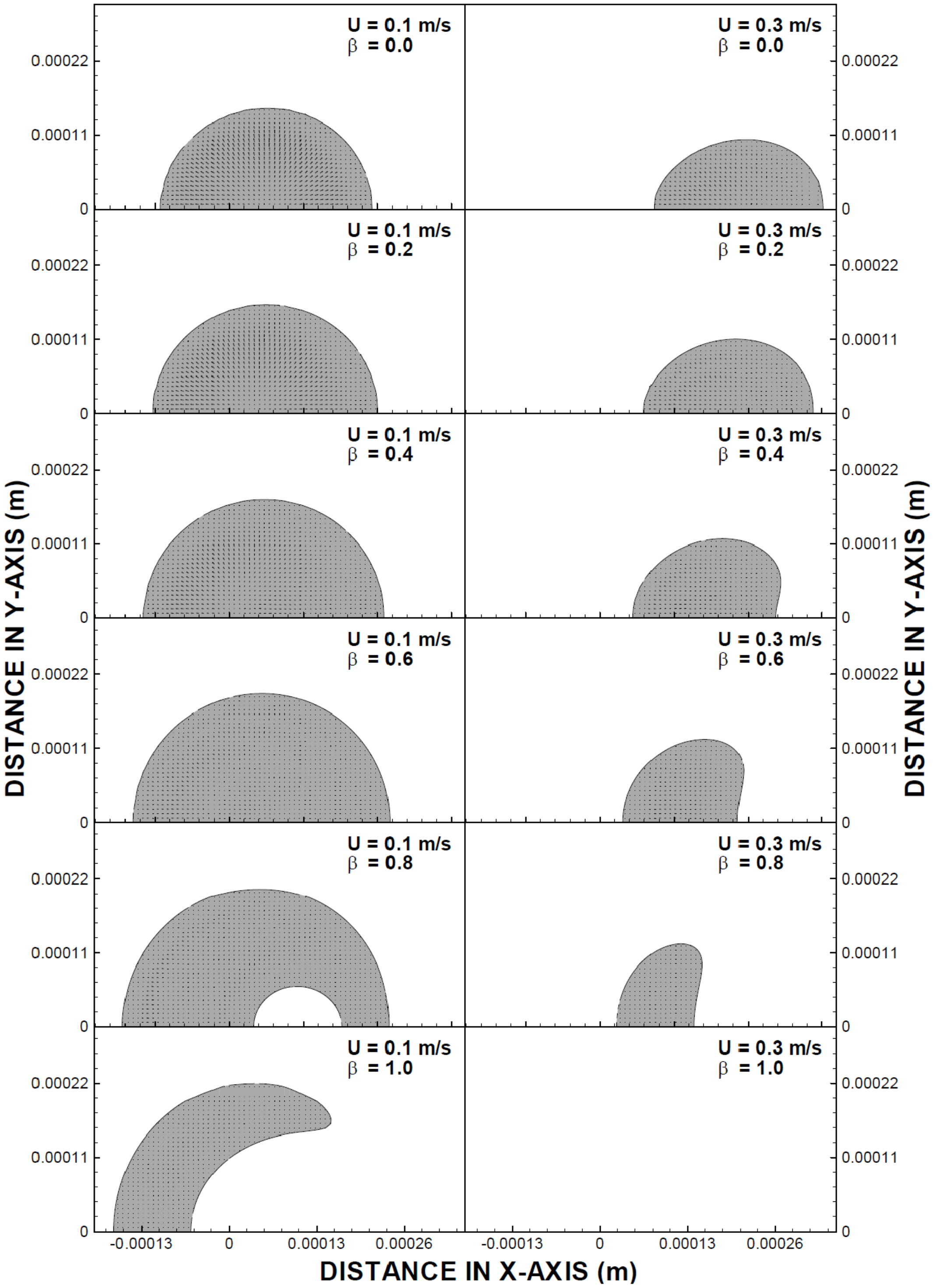

Figure 23: Melt pool in x,y-plane at Steel surface for different laser pulse parameters and two laser scanning speeds.

the end of the 20th pulse. Melt pool size increases with increasing pulse parameter for titanium. However, this increase is limited to $\beta \leq 0.4$ for steel. This is attributed to laser pulse intensity distribution at the surface, which changes with the laser pulse parameter. However, due to the movement of the laser beam, some part of the melt pool vanishes for increasing laser pulse parameter. This is more pronounced for steel substrate which is associated with the solid phase heating at the surface. In this case, low thermal diffusivity of titanium results in melting across the irradiated surface for all β values, except $\beta = 1.0$ for the laser scanning speed of 0.1 m/s. In the case of steel, melting takes place in the region where the laser intensity is higher than the threshold value for melting particularly melting takes place in the region behind the laser beam axis where x values are negative. The Marangoni flow is not significant despite the fact that the flow velocity is higher in the region where the melt depth is not shallow. The laser scanning speed has significant effect on the melt pool size and the Marangoni flow in the melt pool. The melt pool size in the x-y plane reduces considerably with increasing laser scanning speed (Figure (23)). This is associated with the rate of energy deposited into the workpiece, which becomes less with increasing scanning speed.

Figure (24) shows temperature distribution inside steel and titanium workpieces along the z-axis for two laser pulse parameters and two laser scanning speeds. It should be noted that x and y – axes locations are at the centre of irradiated spot. Temperature decay is sharp in the surface vicinity where the laser beam energy is deposited. As the distance from the surface increases, temperature decay becomes gradual especially below the melt depth where conduction is the sole mechanism for heat transfer. This is

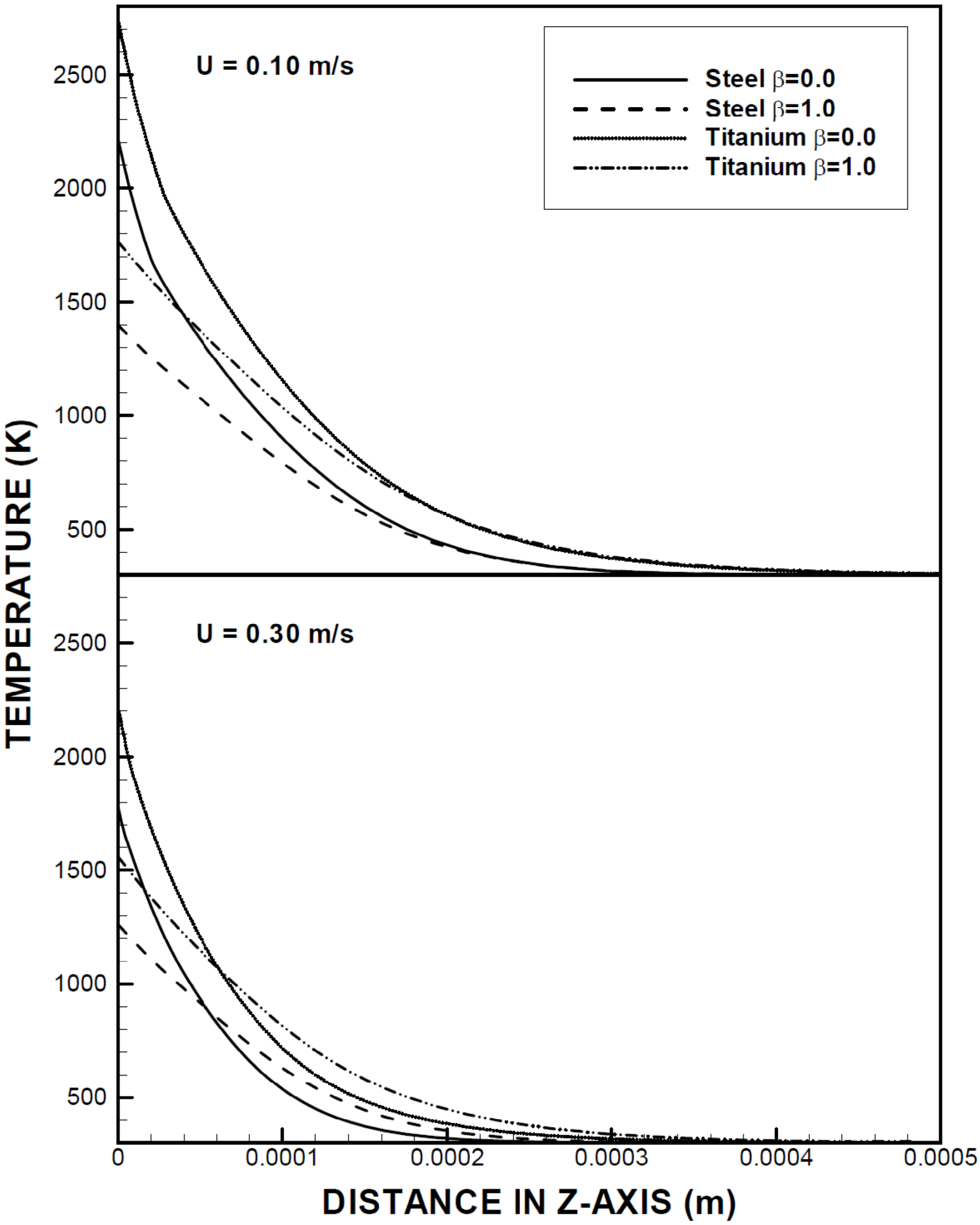

Figure 24: Temperature variation along z-axis for Steel and Titanium.

particularly true for the laser pulse parameter $\beta = 0$ which corresponds to the Gaussian power intensity distribution. In the case of $\beta = 1$ laser intensity reduces at the irradiated spot centre. This is true for steel and titanium workpieces. Temperature gradient along the z–axis for two laser pulse parameters and scanning speeds are shown in figure (25). It is evident that temperature gradient is high in the surface vicinity for low values of laser pulse parameter $\beta = 0$ which is more pronounced for low laser scanning speed (0.1 m/s). The temperature gradient remains high at the surface vicinity irrespective of laser pulse parameter and laser scanning speed. Temperature gradient is high for titanium than that corresponding to steel. This is attributed to the thermal conductivity of titanium, which is low as compared to steel while lowering heat transfer from surface to the solid bulk. The change in the temperature gradient indicates the phase change during the heating; in which case, the decay of the slope becomes gradual across the region where the phase change takes place. This is more pronounced for the laser pulse parameter $\beta = 1$.

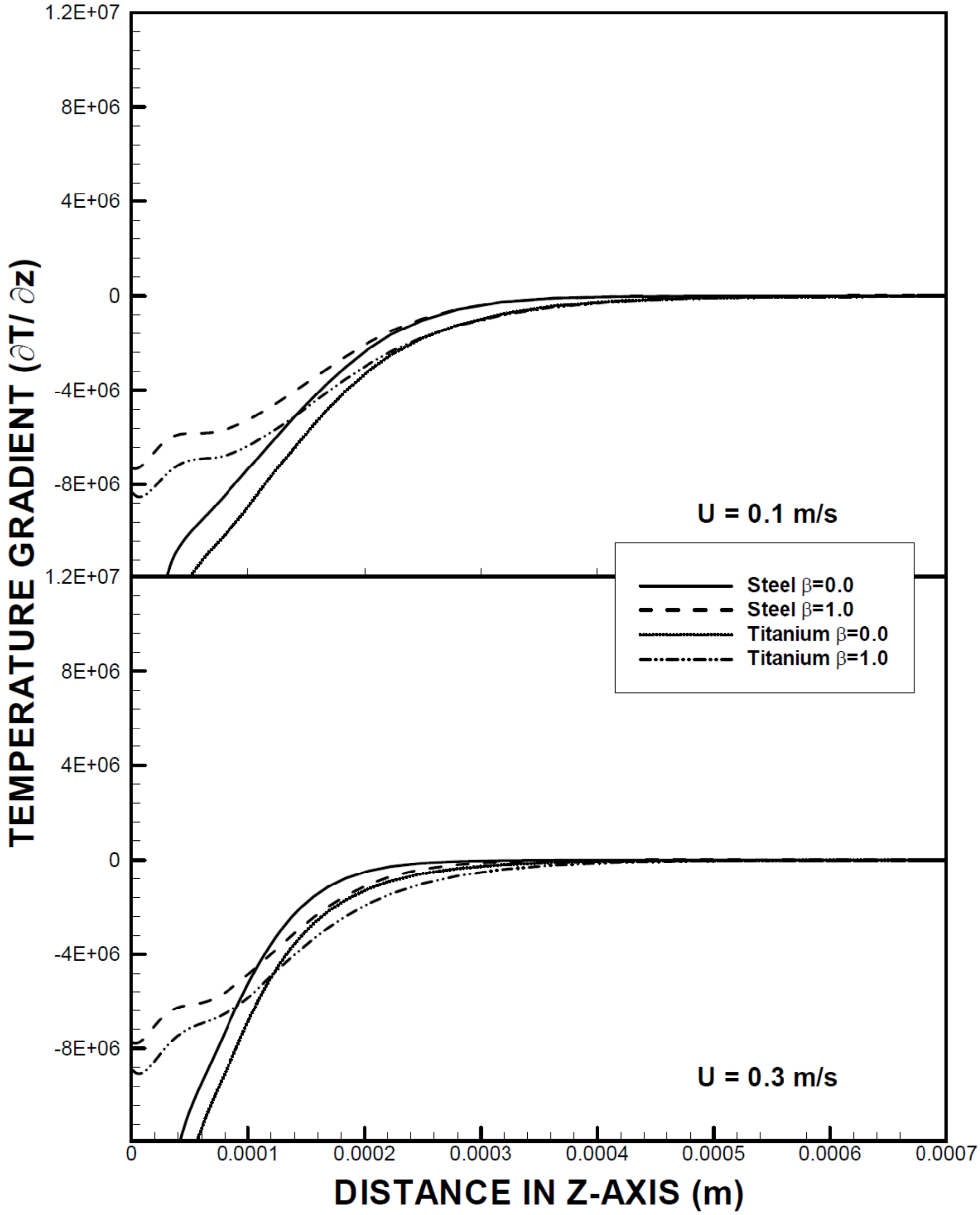

Figure 25: Temperature gradient along z-axis for Steel and Titanium.

4.3. EFFECT OF MATERIAL PROPERTIES: STEEL AND TITANIUM

Figure (26) shows temperature variation at titanium and steel surfaces along the y- axis for two laser pulse parameters and two laser scanning speeds. The x and y –axes locations are at the centre of the irradiated spot. Temperature decay at the y - axis almost follows the laser pulse intensity distribution for both pulse parameters $\beta = 0$ and $\beta = 1$. However, in the phase change region, where the peak laser intensity is high, temperature profile deviates from the laser pulse profile. The formation of melting zone across the melt pool and the solid substrate is visible where temperature remains almost the same. Temperature decay in the irradiated spot centre is low for $\beta = 0$. In this case, liquid phase heating occurs in the region, since the peak temperature exceeds the melting temperature of the substrate material. The peak temperature remains high for titanium as compared to steel. However, temperature decays sharper for titanium than that of steel. This can also be observed from figure (27), in which temperature gradients along the y – axis is shown for two laser pulse parameters and scanning speeds. It is evident that temperature gradient remains low for steel in the region $0 \leq y \leq 0.00025$ m. This is true for both laser scanning speeds and laser pulse parameters. The slope of temperature gradient changes across the mushy zone at the surface, since temperature remains almost constant in this region. The size of mushy zone remains almost the same for all laser scanning speeds and pulse parameter for steel.

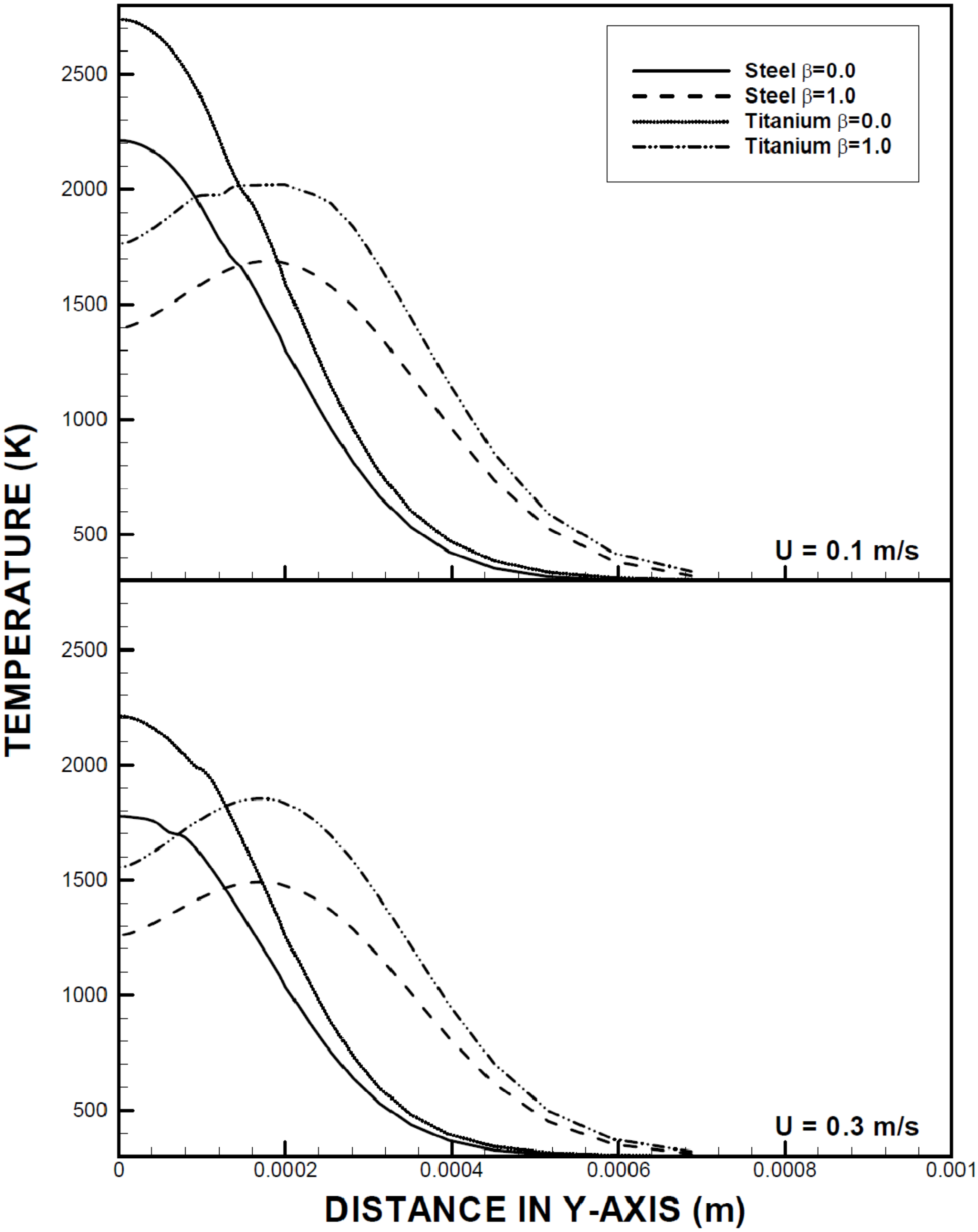

Figure 26: Temperature variation along y-axis for Steel and Titanium.

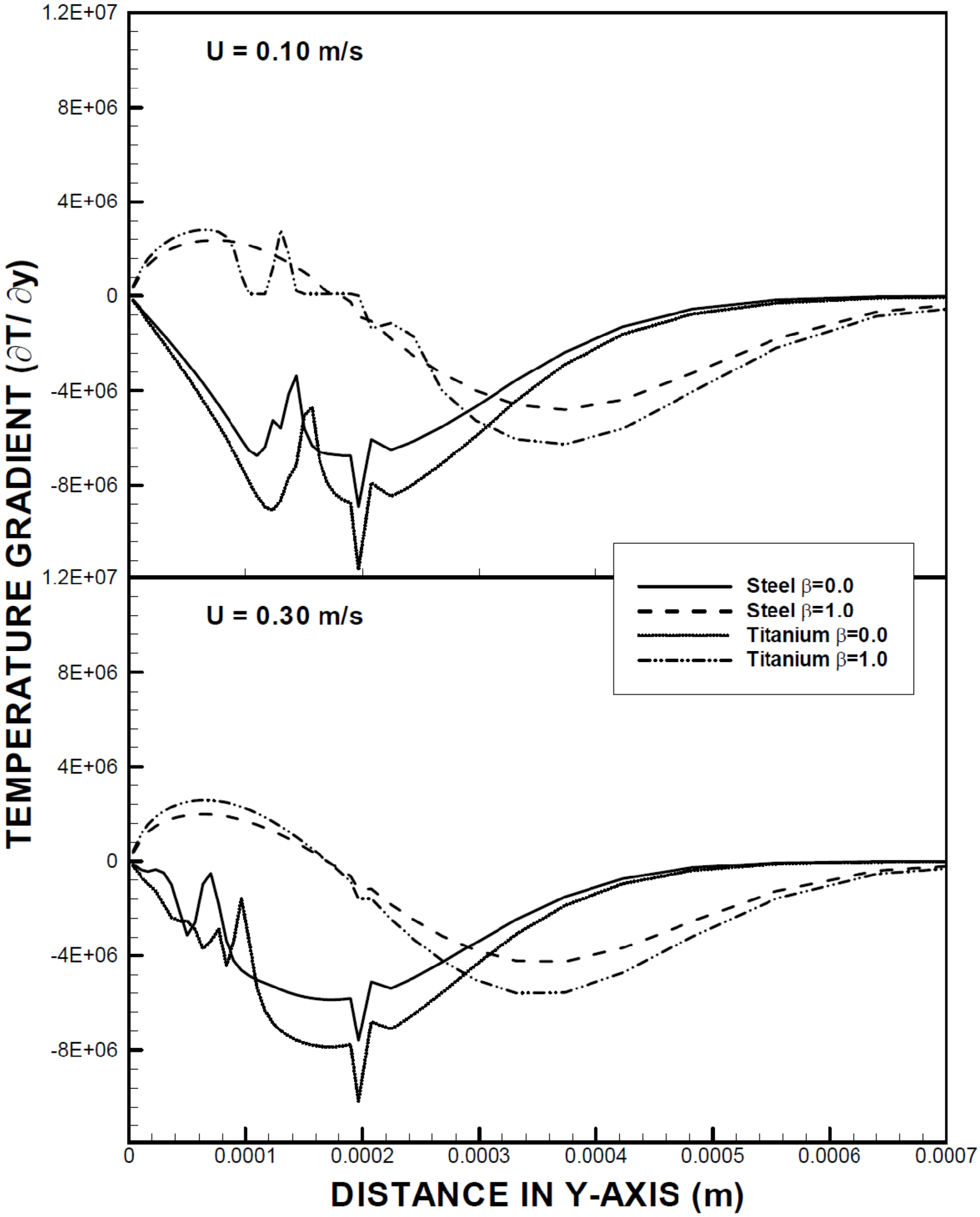

Figure 27: Temperature gradient along y-axis for Steel and Titanium

Figure (28) shows temperature distribution at titanium and steel surfaces along the x – axis for two laser pulse parameters and laser scanning speeds. It should be noted that y = 0 and z = 0 corresponds to the irradiated spot centre at the surface. Temperature decay along the x- axis is gradual in the melt zone where temperature exceeds the melting temperature of the workpiece. This is associated with the liquid phase heating at the surface, which in turn result is gradual decay of temperature along the x – axis. This can also be seen from figure (29), in which temperature gradient along the x- axis is shown for steel and titanium. The gradual decay of temperature is true for both laser scanning speeds and laser pulse parameters. Temperature decay is sharp in the region next to the melted zone towards the solid bulk. This is attributed to the conduction heat transfer taking place in this region, since increasing temperature gradient enhances the conduction heat transfer from the melted zone to the solid bulk. However, spikes are observed in the temperature gradient curves indicating the presence of the mushy zone around the melted zone. The influence of the laser pulse parameter on temperature distribution is significant along the x –axis, which is associated with the laser pulse intensity distribution along the x –axis. Increasing laser scanning speed reduces the peak temperature as well as the temperature gradient along the x –axis because of the less rate of energy deposited into the substrate material for high laser scanning speed.

Figures (30) and (31) show melt pool at steel and titanium surfaces for two laser scanning speeds and two laser pulse parameters, respectively. Melt pool size changes with increasing laser scanning speed, which is because of the rate of energy deposition at the surface. The melt pool width is slightly less than

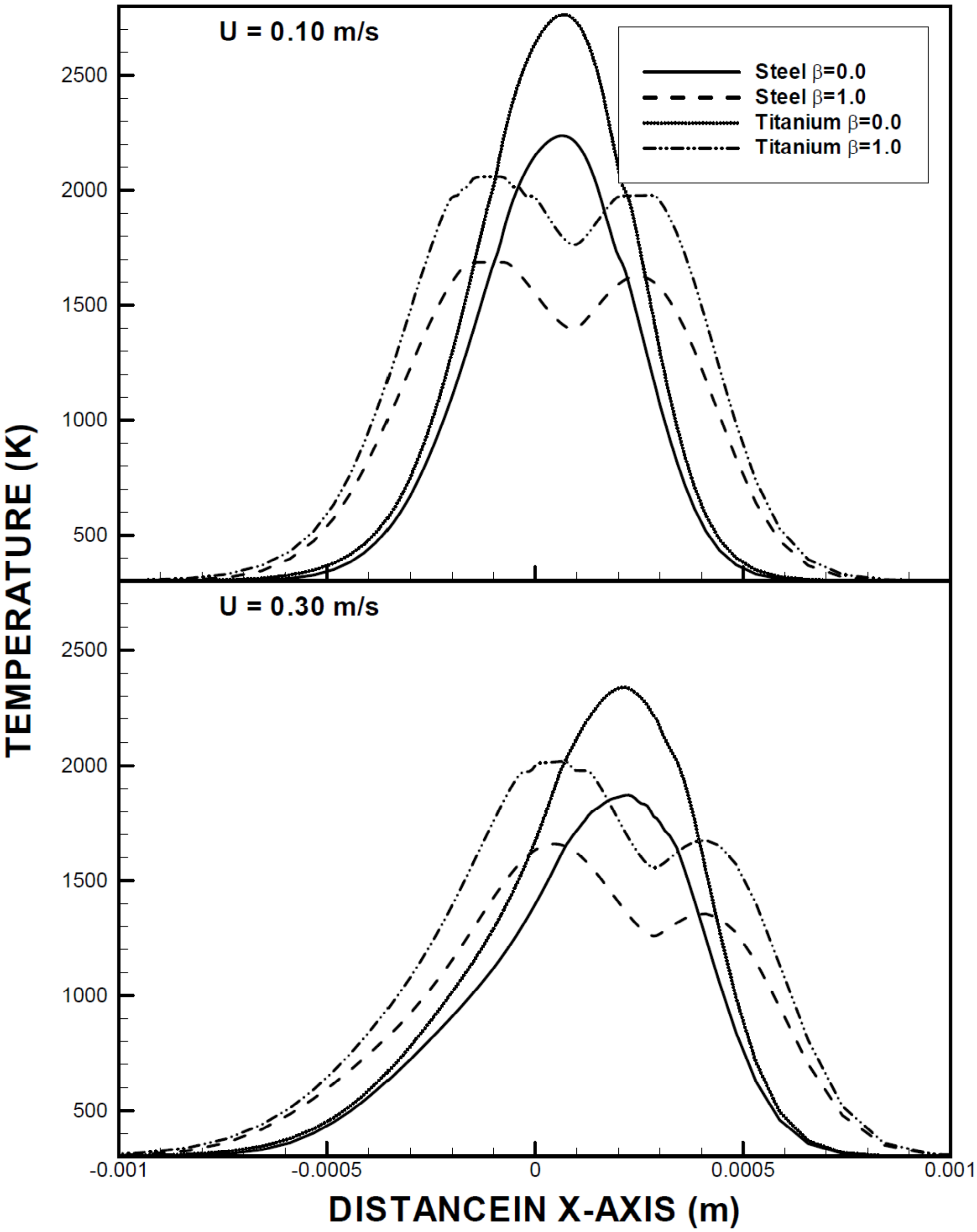

Figure 28: Temperature variation along x-axis for Steel and Titanium.

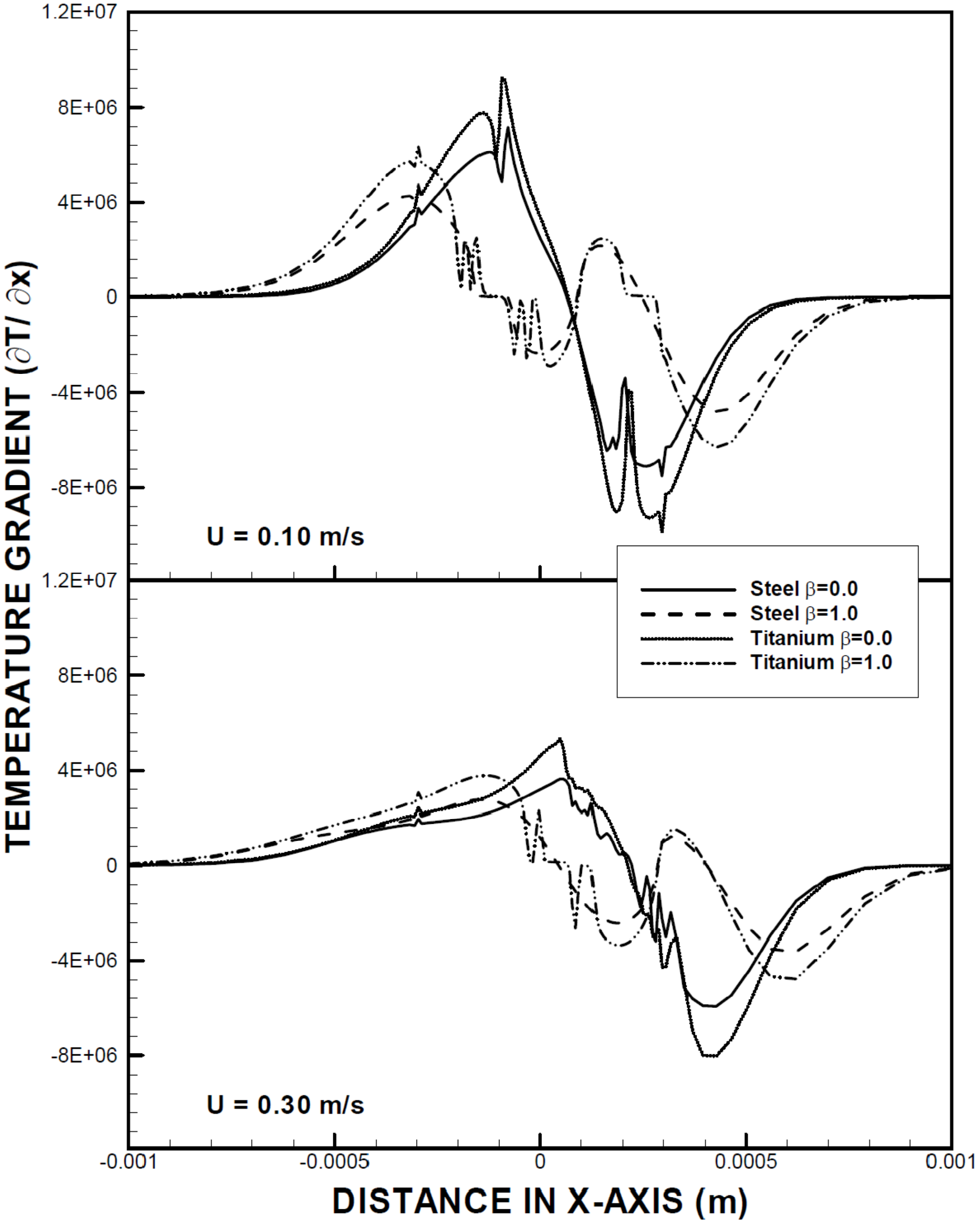

Figure 29: Temperature gradient along x-axis for Steel and Titanium.

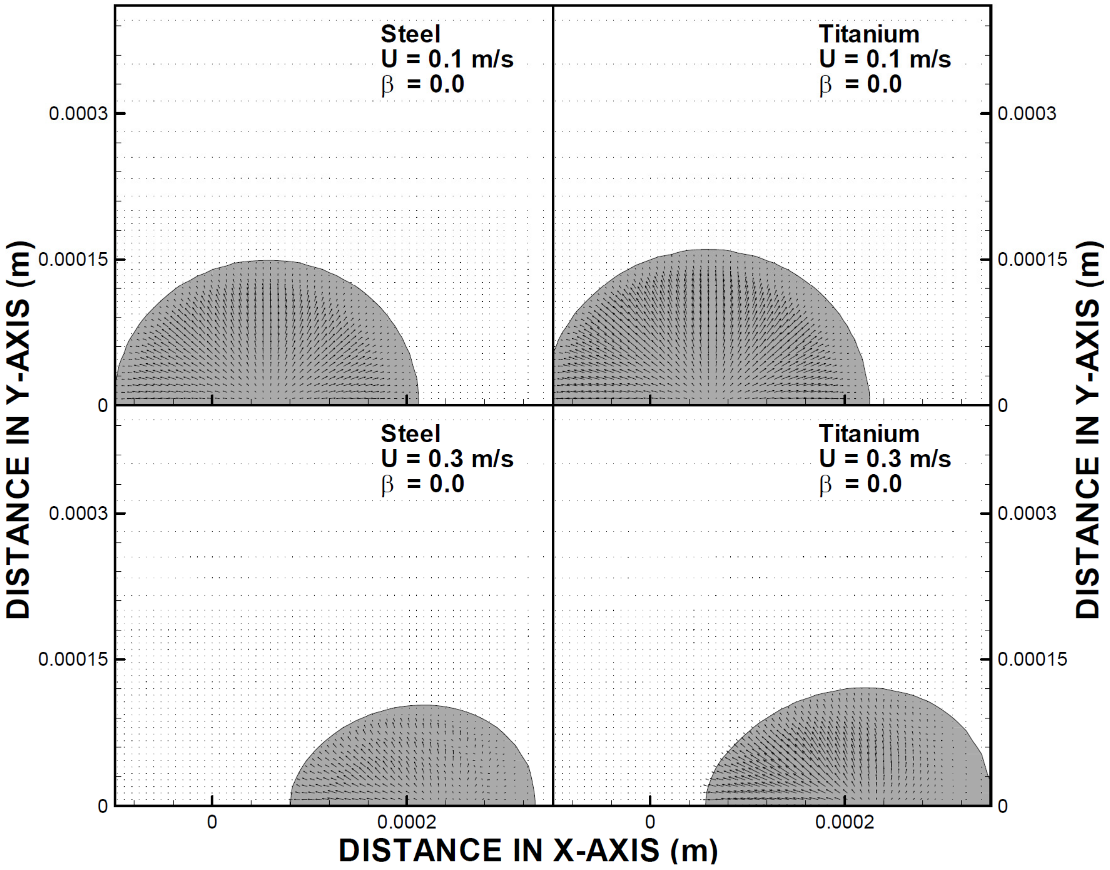

Figure 30: Melt pool in the x, y-plane at the surface of Steel and Titanium for laser pulse parameter β =0.0.

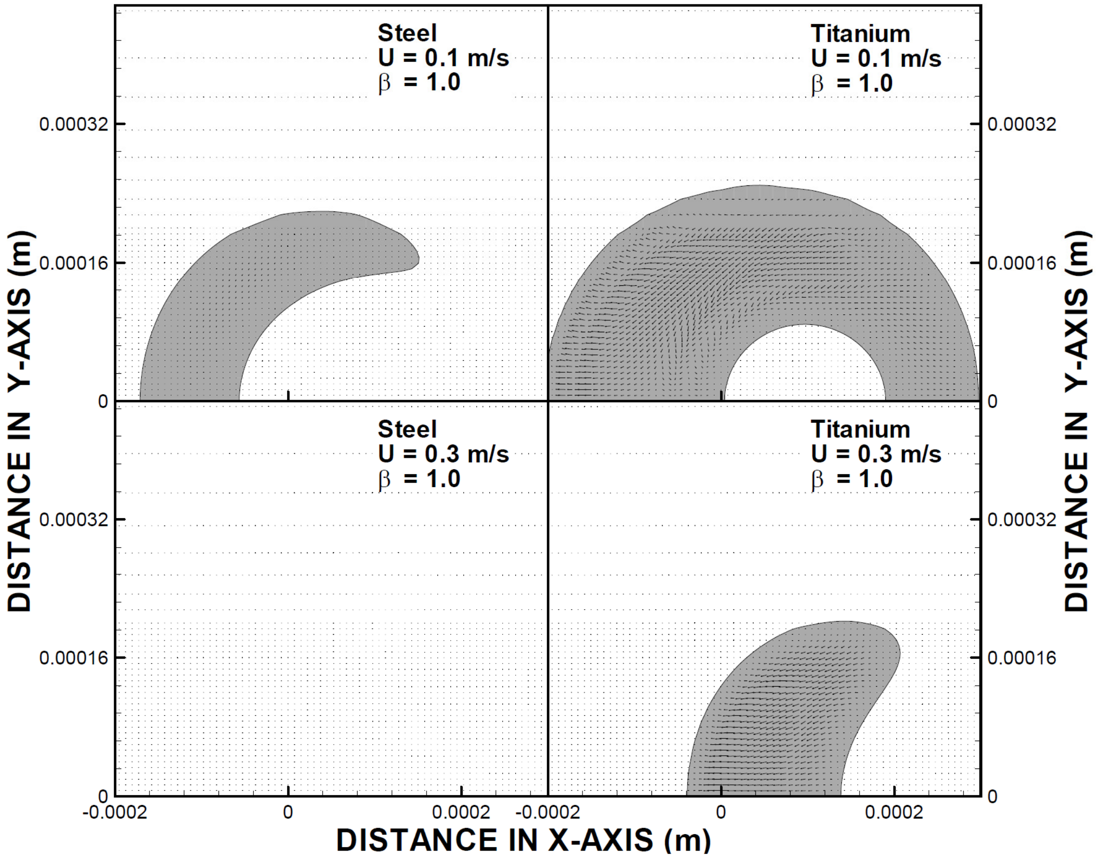

Figure 31: Melt pool in the x, y-plane at the surface of Steel and Titanium for laser pulse parameter β =1.

the melt pool length in the x, y – plane. This is more pronounced for increasing laser scanning speed. The flow generated at the melt pool surface due to the Marangoni effect results in a velocity field from center of the irradiated spot towards the melt pool edge where the surface tension force is high. The flow field developed has almost equal distribution of velocities in all directions towards the melt pool edge for laser scanning speed 0.1 m/s. However, the flow field at the melt pool surface is modified with increasing laser scanning speed. In this case, convective acceleration of the liquid phase enhances the flow in the direction opposite to the laser scanning direction. This results in high flow velocities on one side of the melt surface. This is more pronounced for titanium for laser scanning speed 0.3 m/s. The melt pool size developed at the x-y plane (at the surface) is larger for titanium than for steel. This is attributed to the low thermal conductivity of titanium, which in turn results in high surface temperature and consequently large melt pool size. In the case of the laser pulse parameter $\beta = 1$, the melt pool shape and size become different than that of $\beta = 0$. For titanium, due to the laser pulse intensity distribution at the surface, the solid phase appears within the melt pool, where laser pulse intensity is low, and partially formed melt pool is observed for steel for laser scanning speed of 0.1 m/s. The Marangoni effect in the melt pool results in complex flow field in titanium; however, negligibly small velocity field is developed at the surface of steel melt pool. As the laser scanning speed increases to 0.3 m/s, phase change at the steel surface ceases and solid phase heating takes places. In the case of titanium, partially formed melt pool occurs at the surface and flow acceleration opposite to laser scanning direction causes slightly higher velocities in this direction.

4.4. STRESS ANALYSIS

To study stress generation due to laser heating, simulations were carried out for three consecutive laser heating pulses. It is followed by an extended period of cooling so that the substrate material returns to room temperature. The temporal variation of temperature is shown in figure (32). The study was limited to three pulses to ensure that phase change does not occur. Consequently, only solid phase heating is considered. It is apparent that heat dissipation takes place with progressing time from the irradiated spot towards the solid bulk; therefore, temperature at the irradiated spot center reduces. This lowers the temperature gradient and the rate of heat dissipation in this region. As a result, temperature decays exponentially and becomes asymptotic reaching the ambient temperature. The variation of temperature along the x-axis at the end of the third heating pulse is shown in figure (33). At the end of the third heating pulse, the center of irradiation has moved forward towards the positive x-direction at the surface and temperature is maximum at this location.

Figure (34) is the hydrostatic stress distribution at the end of the third heating pulse. The peak stress occurs at the point of maximum temperature intensity. A negative peak occurs at the location which was heated initially by the first and second pulses but the absolute value of this peak is much smaller as compared to the maximum stress occurring at the point of maximum temperature. This is made obvious in figure (35) which depicts hydrostatic stress variation in x-axis at the end of the third heating pulse.

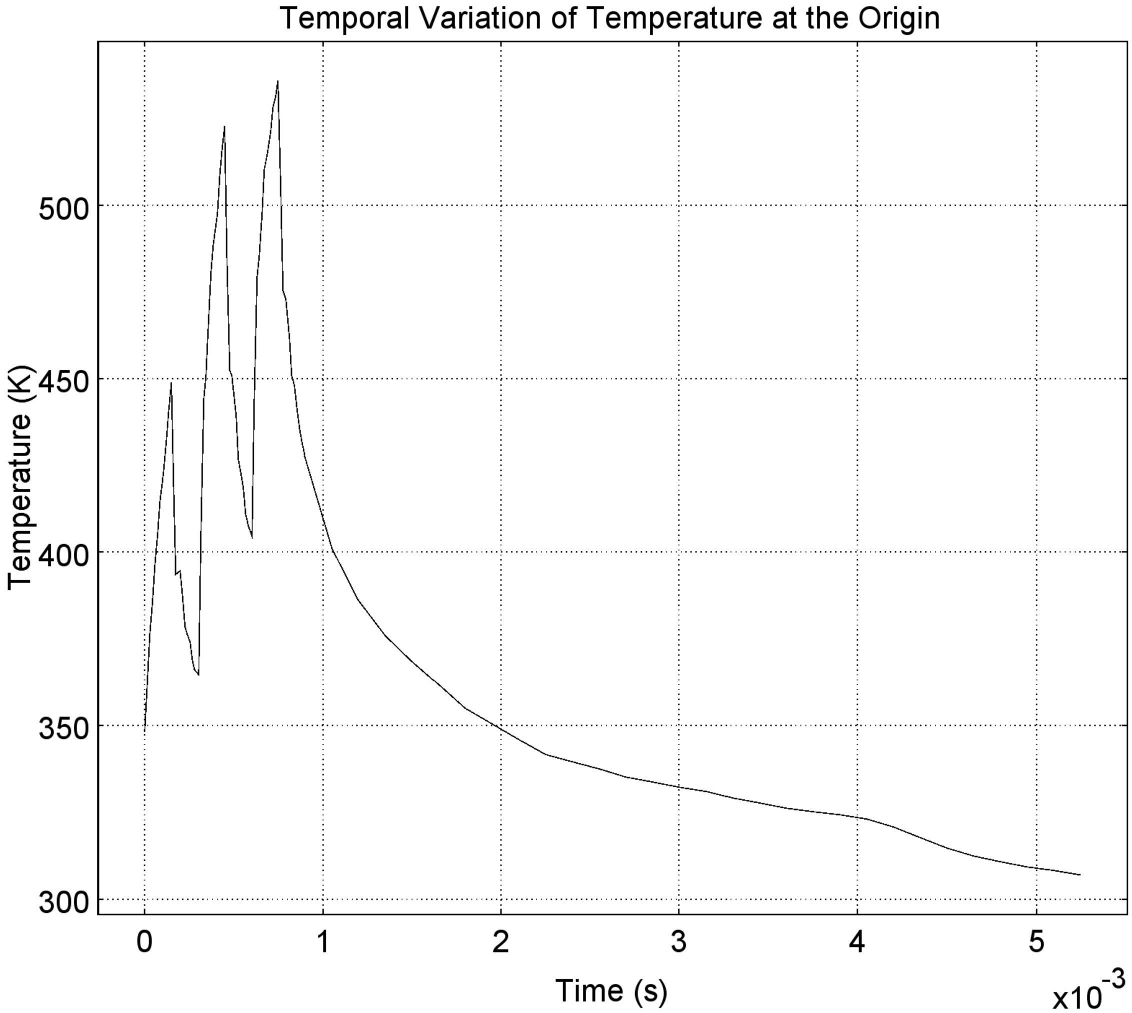

Figure 32: Temporal variation of temperature at the origin

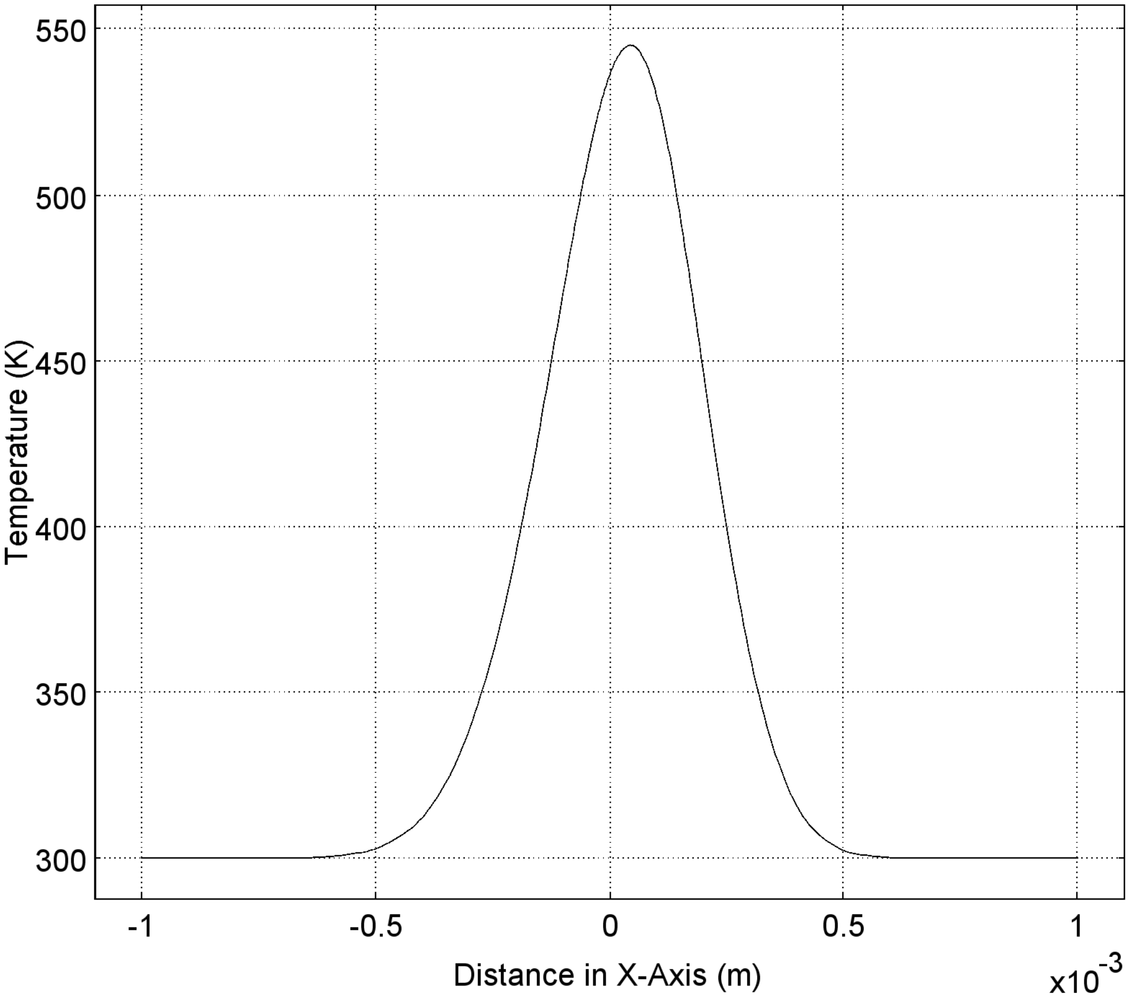

Figure 33: Temperature variation in X-axis at the end of the third heating pulse

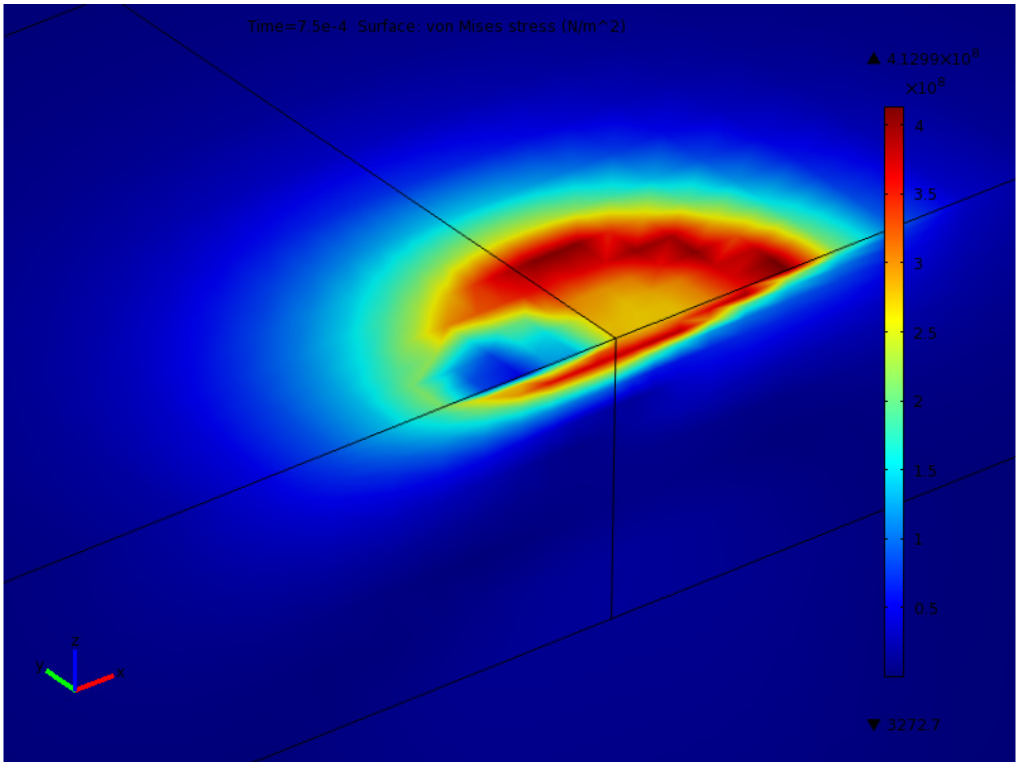

Figure 34: Von Mises stress distribution at the end of the third heating pulse

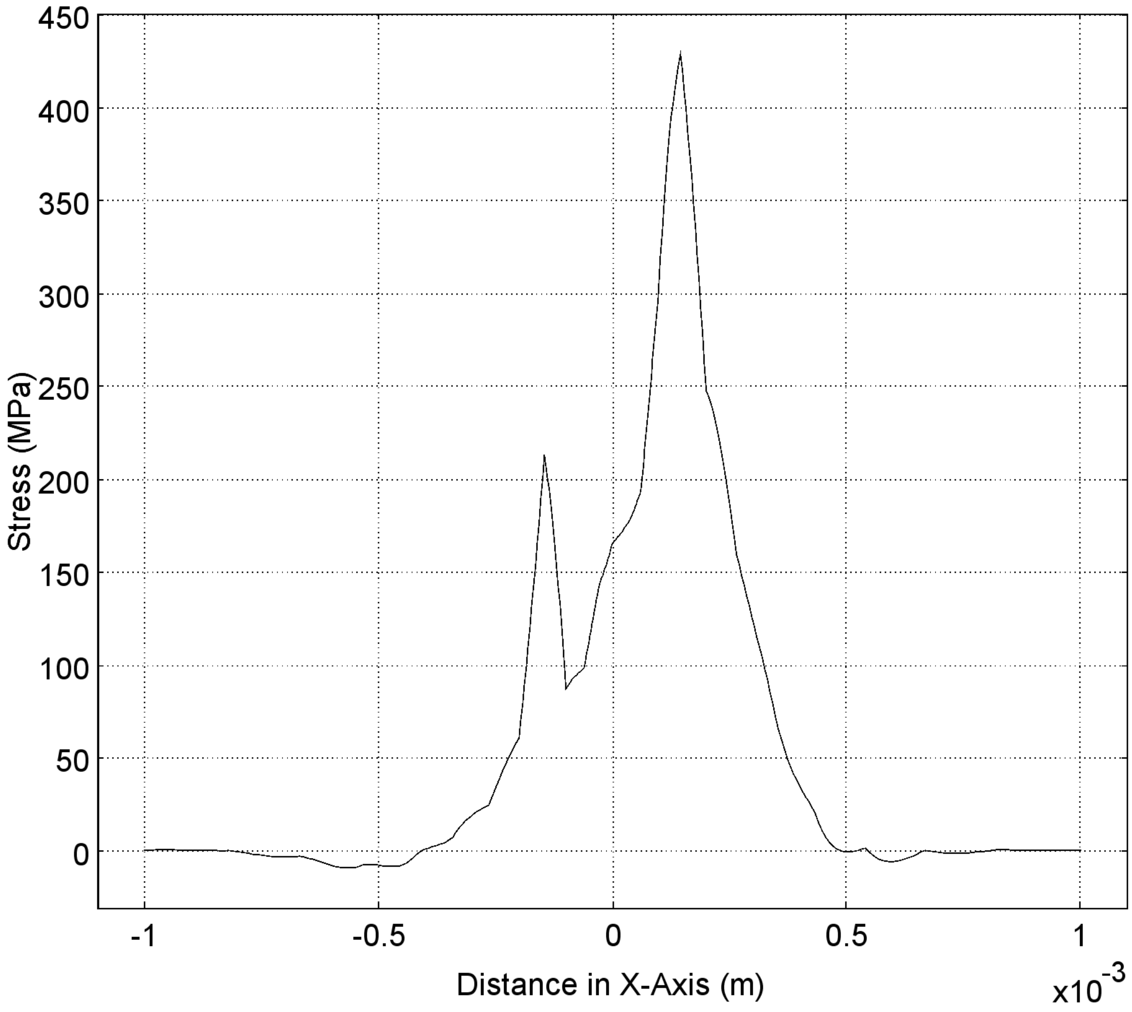

Figure 35: Hydrostatic stress variation in x-axis at the end of the third heating pulse

A slight negative value occurs followed by a maximum positive value which occurs at the center of irradiance.

The stress distribution at the end of third consecutive heating pulse along the y-axis is shown in figure (36). The peak is located slightly away from the center of irradiation. This is because of the higher value of yield stress at lower temperatures.

After sufficient time after end of heating, the substrate reaches room temperature. At this point all thermal stresses due to temperature difference return to zero, and the stresses in the block are residual stresses.

Figure (37) displays the variation of residual hydrostatic stress at the surface of the workpiece. The stress is distributed throughout the irradiated region and the heat effected zone. In contrast to the hydrostatic stress at the end of the third heating pulse, the negative peaks are quite pronounced and the absolute value is comparable to the positive peaks.

This becomes more obvious when we see the variation of the hydrostatic stress along the x-axis (Figure (38)). Each compressive peak is followed by a tensile peak. Consequently, the von mises is almost constant in the heat affected zone (Figure (39)).

However, it must be noted that the final results depend on the grid size. The problem is computationally very expensive. Consequently, grid independence was not achieved. Decreasing element size and increasing the mesh density will change the maximum values of the von mises and hydrostatic stress.

Moreover, using a more realistic isotropic hardening model instead of the elastic-perfectly-plastic model will provide better results. The effect of geometric non-linearity and annealing and recrystalization must also be accounted for in the simulation. However, accurate physical properties such as tangent modulus are not easily available as a function of temperature. Therefore, some simplifying assumptions must be made.

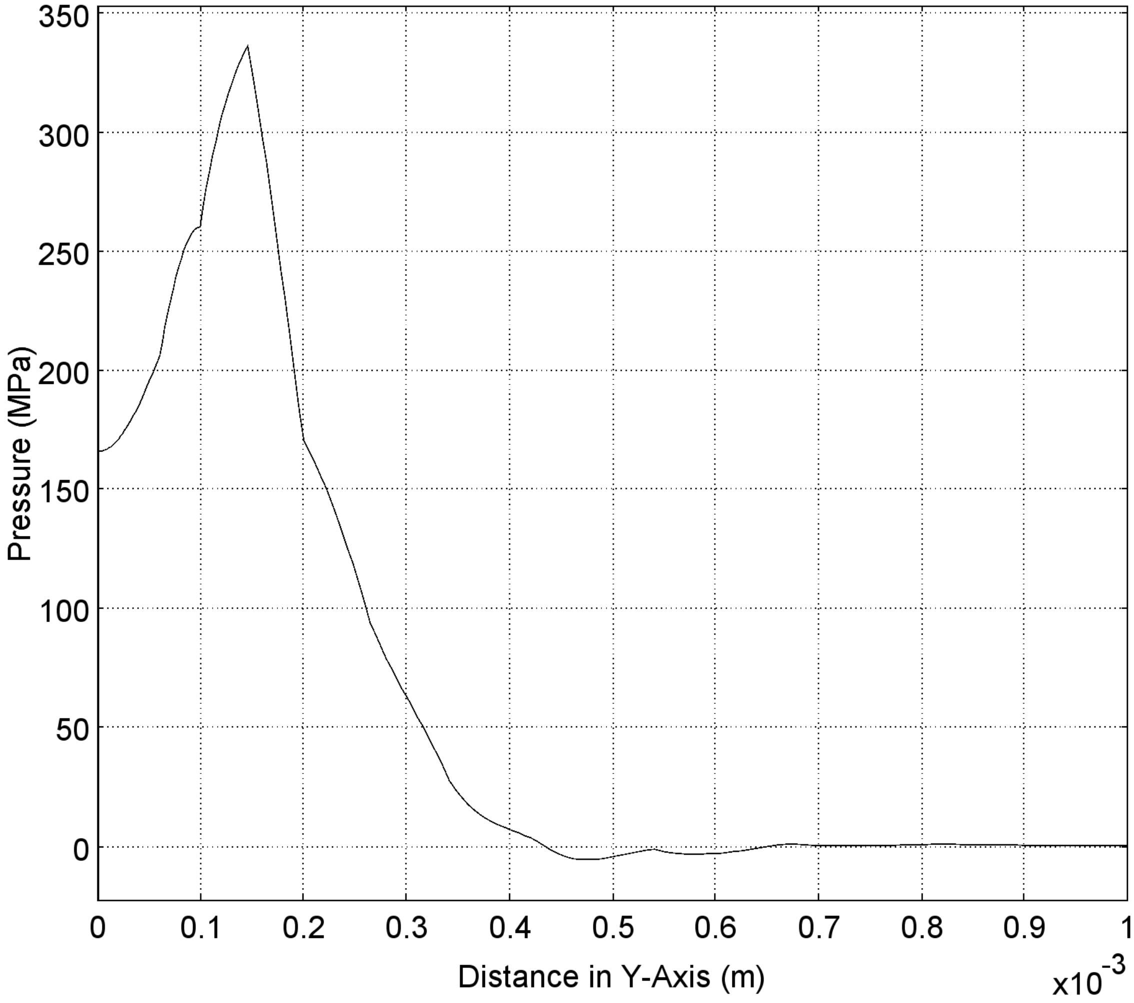

Figure 36: Hydrostatic stress along y-axis at the end of third heating pulse

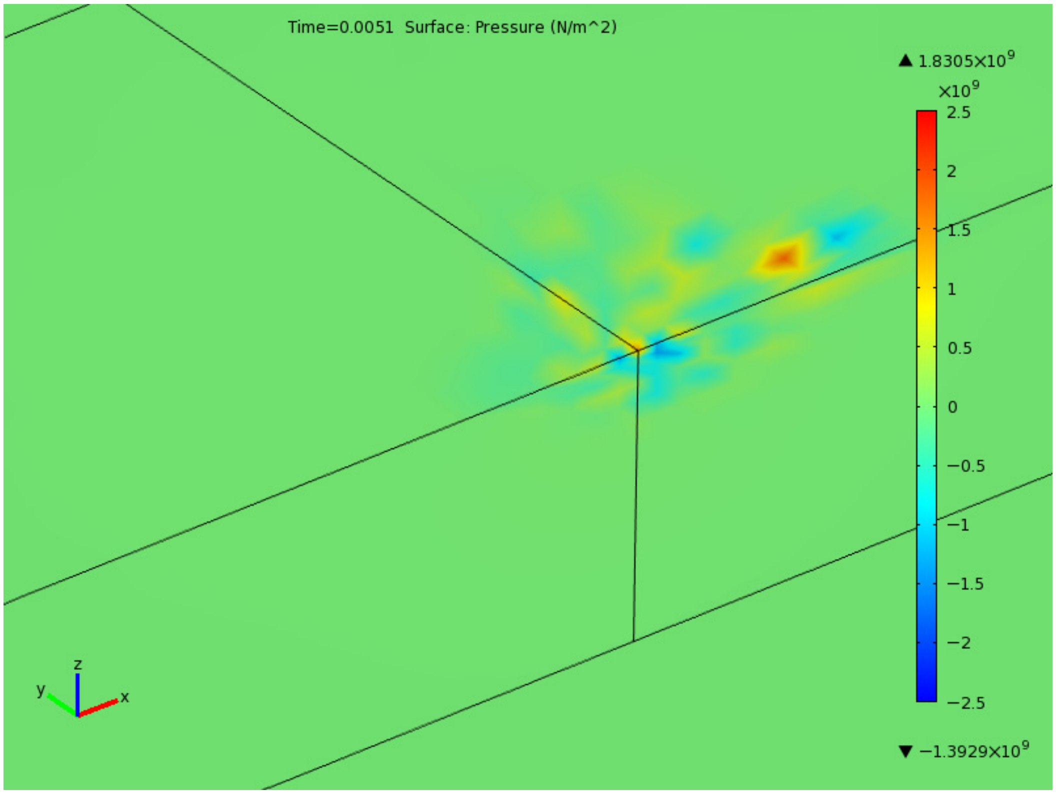

Figure 37: Residual stress

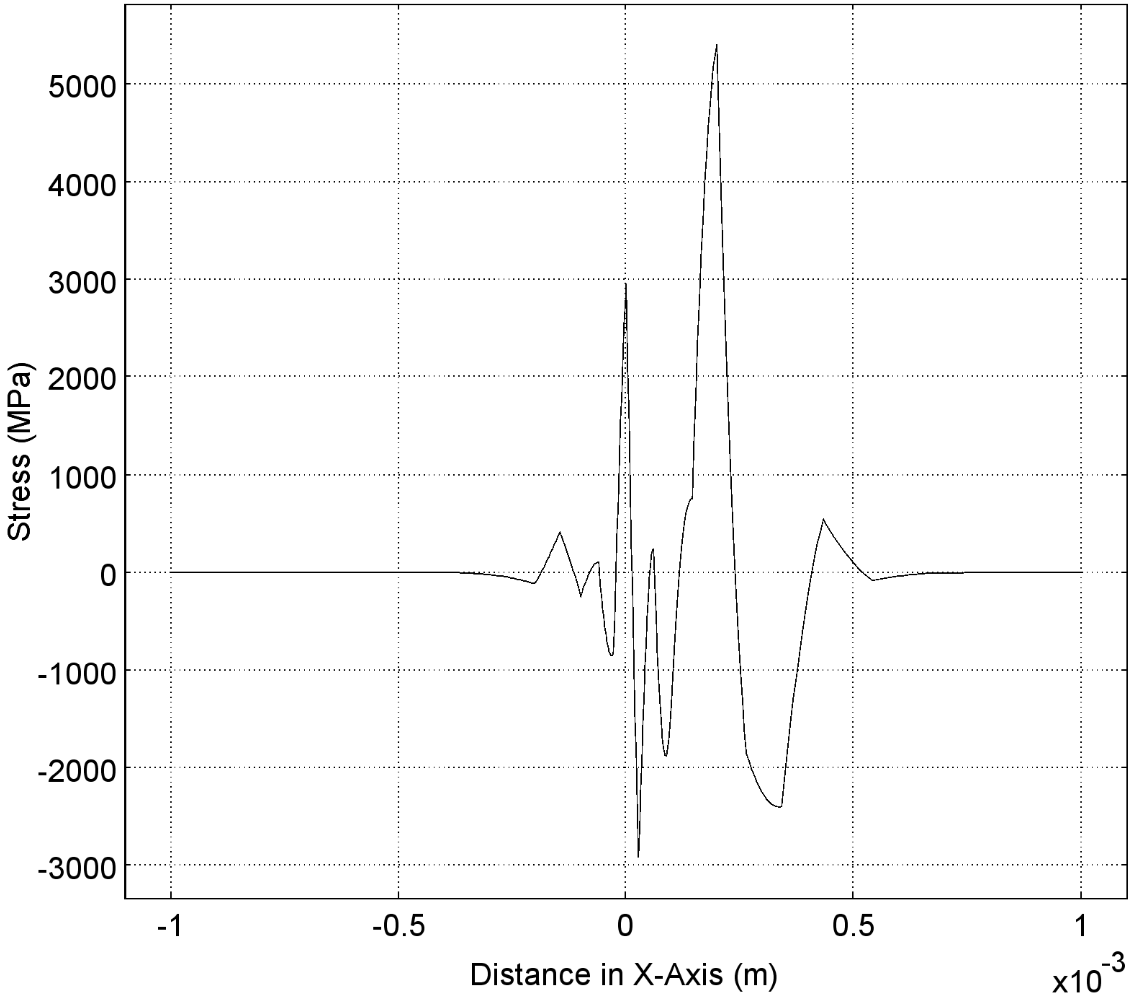

Figure 38: Residual stress distribution along x-axis after cooling

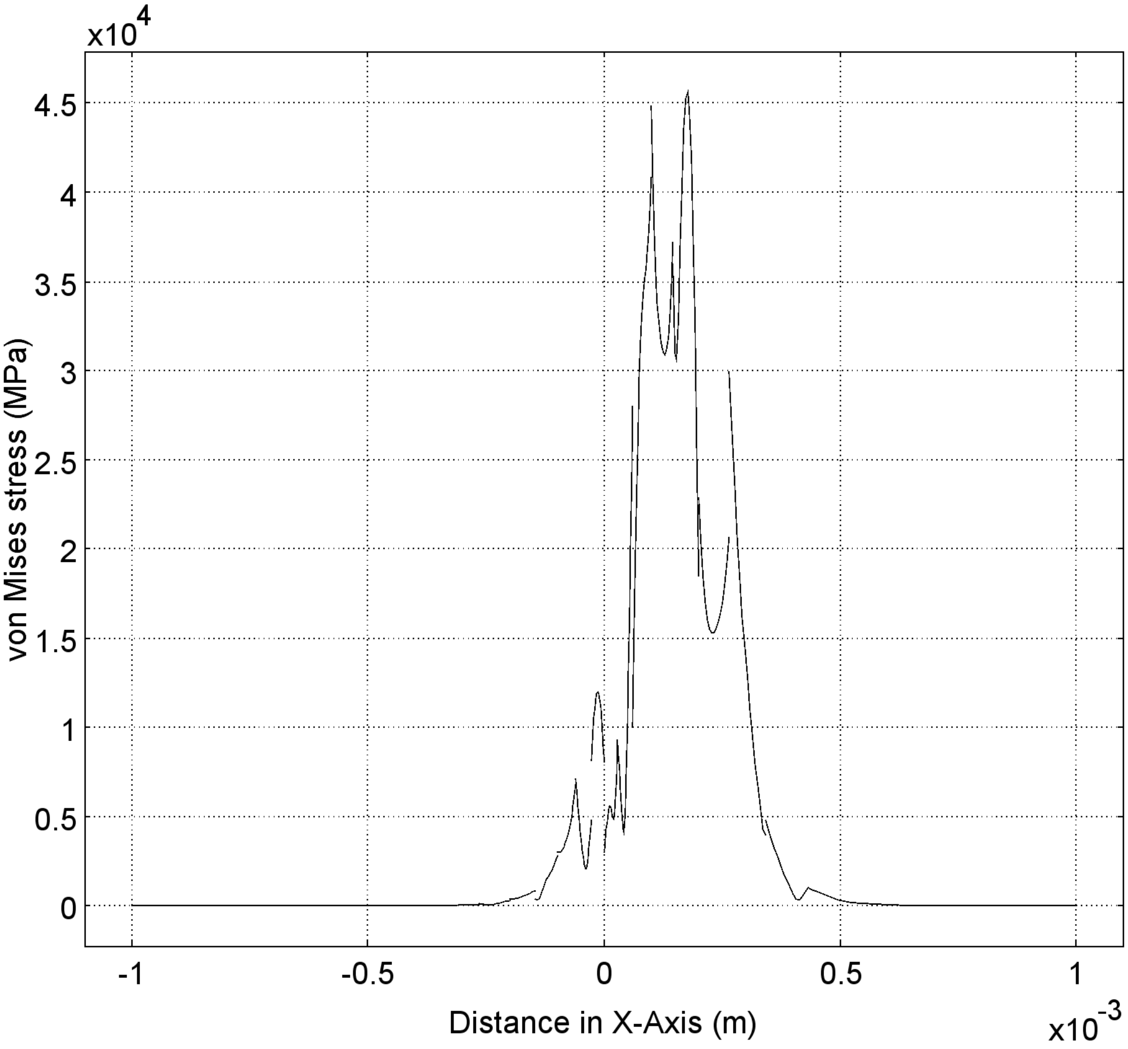

Figure 39: Von Mises Stress Distribution along the x-axis after cooling

CHAPTER # 5

EXPERIMENTAL VERIFICATION

The laser used in the experiment is a CO_2 laser (LC-αIII-Amada) and delivering nominal output power of 2000 W with adjustable duty cycle. Nitrogen emerging from a conical nozzle and co-axially with the laser beam is used. 127 mm focal lens is used to focus the laser beam, which results in the focal radius of 0.3 mm at the surface. The laser heating parameters are given in Table 3. Optical Microscopy is carried out to obtain the micrographs of the laser irradiated surface.

To validate temperature predictions, a thermocouple was used to monitor the temporal variation of surface temperature at the irradiated spot center for the laser pulse parameter $\beta = 0$, which is Gaussian. Two consecutive pulses were used to irradiate the surface. This was necessary to avoid the melting of the surface of the thermocouple during the laser heating process. The thermocouple outputs were calibrated according to the previous study [78]. The experimental error was determined using the experimental repeatability; therefore, the experiments were repeated five times and the error was estimated in the order of 5%.

Figure (40) shows temporal variation of temperature predicted from the simulations and obtained from the thermocouple data at the irradiated spot center for the laser pulse parameter $\beta = 0$. It is evident that temperature predicted agrees well with the

Table 3. Laser heating parameters.

Duty Cycle	Power (W)	Nozzle Gap (mm)	Nozzle Diameter (mm)	Focus Diameter (mm)	N_2 Pressure (kPa)	a (m)
0.4	230	1.5	1.5	0.8	400	0.2×10^{-3}

thermocouple data. The discrepancies between both results are small, which is within the experimental error.

Figure (41) shows top view of laser produced melt pool predicted at the workpiece surface and melt pool obtained from the experiment for laser pulse parameter $\beta = 0$ and laser scanning speed 0.1 m/s. It can be observed that the melt pool size predicted agrees with that obtained from experiments. The differences are negligibly small, which are associated with the uniform properties (isotropic properties) are assumed in the analysis and the experimental errors in the experiment which are estimated as 5% based on the repeatability of the experiment.

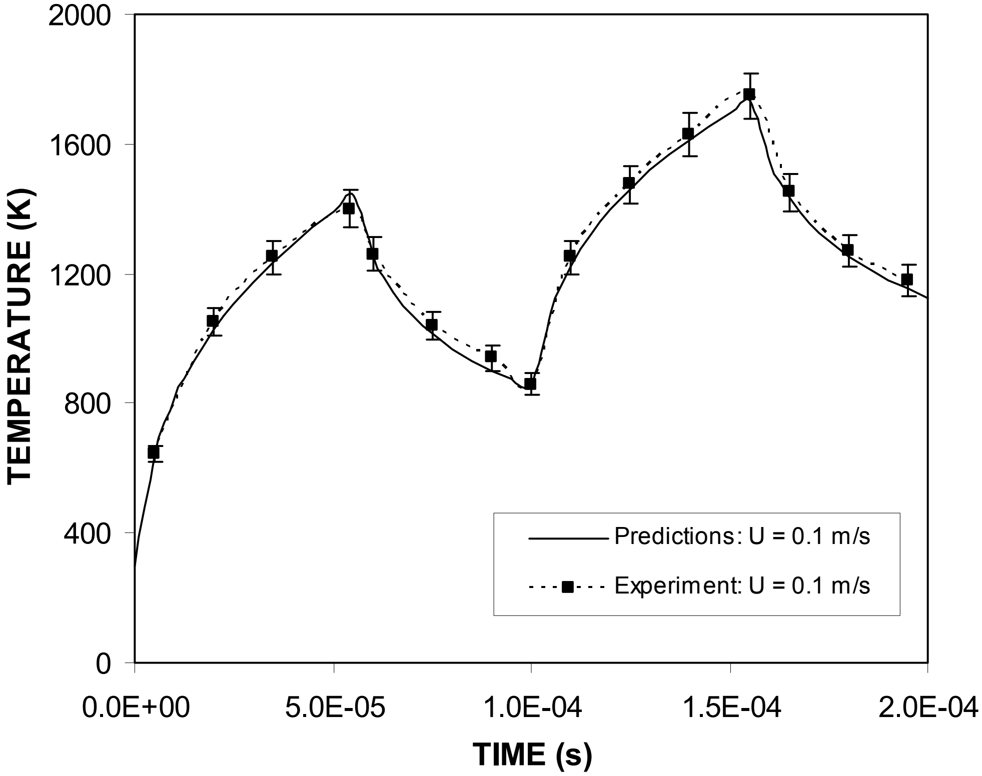

Figure 40: Temporal variation of temperature predicted from simulations and obtained from thermocouple data.

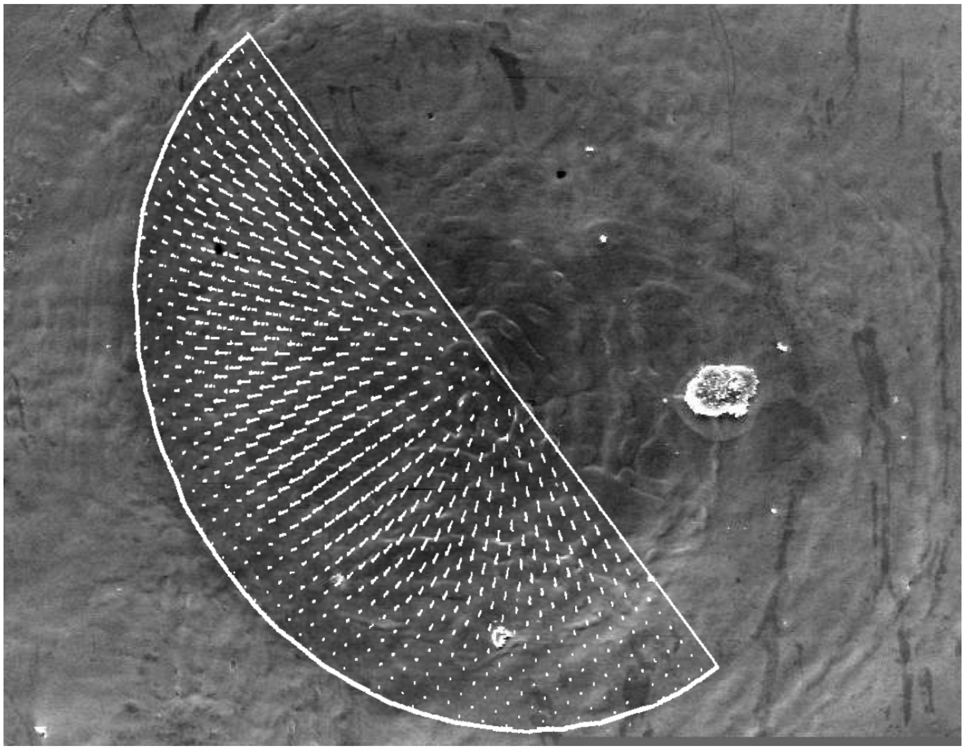

Figure 41: Top view of melt pool from experiment and simulation prediction.

CHAPTER # 6

CONCLUSION

Titanium and its alloys are widely used in the industry due to their high toughness to mass ratio. However, their tribological properties are poor, which limit their practical applicability in harsh environments such as wear and corrosion. Laser surface treatment of titanium alloys provides formation of dense layer with fine grains while improving the hardness of the surface [79].

In the present study, laser repetitive pulse heating of titanium is investigated and phase change in the irradiated region is examined. The study is extended to include the influence of laser scanning speed on the melt formation and the melt pool size. The Marangoni flow in the melt pool is introduced when formulating the heating problem. The laser intensity distribution at the workpiece surface is varied through introducing laser pulse parameter (β). Control volume approach is used to simulate the temperature field while enthalpy porosity method is incorporated to account for the phase change. It is found that temperature at the irradiated surface exceeds the melting temperature of the substrate material resulting in liquid phase heating in melt pool, which is true for the laser pulse parameter $\beta = 0$, which corresponds to the Gaussian intensity distribution at the surface. The laser pulse repetition results in temperature spikes at the surface exceeding the melting temperature for $\beta = 0$ while solid heating takes place for $\beta = 1$ at the irradiated spot center. Increasing laser scanning speed reduces the peak temperature at the surface for all laser pulse parameters. In addition, laser scanning speed has significant effect on the melt size and depth; in which case, melt size reduces considerably with increasing scanning speed. The melt pool size in the surface region changes for the laser pulse parameter $\beta = 1$ and elongated semi-circular melt pools are formed at the surface. However, semi-circular melt pool is modified in size with increasing laser scanning speed. The Marangoni flow results in two counter rotating cells in the melt pool. This is slightly modified for $\beta = 1$ due to the shallow melt pool generated after the 20th heating pulse. Temperature predictions are well compared with the thermocouple data obtained from the experiment.

To compare the effect of material properties, the study was extended to include laser heating of titanium and steel surface for repetitive laser pulses, which scan the workpiece surface at a constant speed. The peak temperature at the surface is higher for titanium as compared to that corresponding to steel, which is attributed to the low thermal diffusivity of titanium. Temperature decay along the z axis is sharp in the melt phase as compared to the solid phase, which is related to energy deposited from the irradiated field, which is high in the surface region. Temperature along the y-axis follows almost the laser pulse intensity distribution at the surface. In this case, increasing intensity parameter lowers the peak temperature at the surface. Two temperature peaks are observed at the surface along the x-axis for increased laser intensity parameter. This is more pronounced as the laser scanning speed increases. The influence of laser scanning speed on temperature profiles is significant; in which case, increasing scanning speed lowers peak temperature at the surface and modifies temperature profile, particularly in the direction of laser scanning along the x-axis. The melt pool size at the surface changes significantly for increased laser pulse parameter and the scanning speed. In this case, increasing laser pulse parameter and scanning speed reduces the melt size. Steel results in smaller melt size than that corresponding to titanium. In addition, melting seizes and solid phase heating takes place at the surface of steel for laser pulse parameter β = 1 and laser scanning speed 0.30 m/s.

It is found that temperature follows almost the laser pulse intensity distribution at the surface along the y-axis provided that phase change at the surface modifies slightly this behavior. The temperature gradient along the y-axis changes slightly, which is attributed to the liquid phase formation at the irradiated surface. This is particularly true for titanium for low laser scanning speed (0.1 m/s). In the case of steel, the peek temperature at the surface remains less than that corresponding to titanium. Temperature decay along the z-axis is sharp in the melt pool, which is attributed to the energy deposited to the melt pool by the laser source and energy conducted from the melt pool to the solid bulk along the z-axis. The mushy zone formed at the edges of the melt pool is notable along the y-axis; however, it is not clearly observable along the z-axis. The size of the melt pool developed is influenced by laser scanning speed and laser pulse parameter. In this case, increasing laser scanning speed reduces the melt pool size at the surface. In addition partially formed melt pool occurs at the surface for the laser pulse parameter β = 1. The convective acceleration of the flow due to laser scanning speed influences the velocity field in the melt pool. The melt pool size predicted for steel is smaller than that of titanium for all scanning speeds and laser pulse parameters incorporated in the simulations. The phase change at the steel surface ceases for laser scanning speed 0.3 m/s and laser pulse parameter β = 1.

Temperature predictions are validated with the thermocouple data obtained from the experiments. The size of the melt pool predicted is compared with its counterpart obtained from the experiment. Very good agreement is found between the experimental results and simulation predictions. The discrepancies between the results are within the experimental error.

To undertake the study of stress generation during the laser heating process, the finite element method was used. However, finite element solvers require more resources as compared to finite difference solvers. Consequently, solving for thermal stresses is much more resource intensive as compared to solving for the temperature and velocity field. Moreover, finite difference methods allow for non-conformal mesh generation.

The results for the stress analysis are found to be physically realistic and the values predicted are feasible. It is shown that a heat affected zone is generated in which plastic deformation takes place resulting in residual stress formation. The localized heating leads sharp temperature gradients and storing compressive energy in the heated material due to the unequal expansion. The resulting plastic deformation allows this energy to be released. Consequently, compressive and tensile stress peaks distributed throughout the heat affected zones takes place.

NOMENCLATURE

English Symbols

a	Gaussian Parameter
C_p	Specific Heat Capacity at Constant Pressure
E	Total Potential Energy
e_0	Potential Energy per Unit Volume
$E_{elastic}$	Young’s Modulus of Elasticity
h	Specific Enthalpy
h_{lat}	Latent Enthalpy of Fusion
h_{ref}	Reference Enthalpy
h_{sens}	Sensible Enthalpy
h_t	Heat Transfer Coefficient
I_0	Peak Intensity
k	Thermal Conductivity
L	Deformed Length
L_0	Undeformed Length
P	Peak Power Output
S	Momentum Sink
S_0	Intensity Distribution
t	Time
T_{amb}	Ambient Temperature

t_f	Pulse Fall Time
$T_{liquidous}$	Liquidous Temperature
t_p	Total Pulse Length
t_r	Pulse Rise Time
T_{ref}	Reference Temperature
$T_{solidous}$	Solidous Temperature
U	Scanning Velocity
x_0	x-Coordinate of Irradiation Spot Center

Greek Symbols

α	Linear Coefficient of Thermal Expansion
β	Pulse Parameter
γ	Surface Tension
ε	Strain
θ	Liquid Fraction
τ	Shear Stress
ν	Viscosity
ρ	Density
σ	Stress
σ_{vm}	Von Mises Stress
σ_{yield}	Yield Stress

BIBLIOGRAPHY

[1] M. Gower, "Industrial applications of laser micromachining," *Optics Express,* vol. 7, pp. 56-67, 2000.

[2] F. Bachmann, "Industrial laser applications," *Applied Surface Science,* vol. 46, pp. 254-263, 1990.

[3] N. Tabata*, et al.*, "Present and future of lasers for fine cutting of metal plate," *Journal of Materials Processing Technology,* vol. 62, pp. 309-314, 1996.

[4] J. Ready and D. Farson, *LIA handbook of laser materials processing*: Laser Institute of America Orlando, 2001.

[5] G. Crepaz*, et al.*, "High-Frequency Induction Surface Hardening by Multiple Power Pulses," *Heat Treatment Shanghai 1983,* vol. 3, 1983.

[6] S. Z. Shuja, "Simulation of three-dimensional laser gas-assisted heating of solid substance: the fourier heat conduction theory approach," Doctor of Philosophy, Mechanical Engineering, King Fahad University of Petroleum and Minerals, Dhahran, 1998.

[7] J. Zhou*, et al.*, "Transport phenomena and keyhole dynamics during pulsed laser welding," *Journal of Heat Transfer,* vol. 128, p. 680, 2006.

[8] S. Safdar*, et al.*, "Numerical analysis of the effects of non-conventional laser beam geometries during laser melting of metallic materials," *Journal of Physics D: Applied Physics,* vol. 40, p. 593, 2007.

[9] M. Sheikh and L. Li, "Understanding the effect of non-conventional laser beam geometry on material processing by finite-element modelling," *Proceedings of the Institution of Mechanical Engineers, Part C: Journal of Mechanical Engineering Science,* vol. 224, pp. 1061-1072, 2010.

[10] B. Wong*, et al.*, "Nano-scale machining via electron beam and laser processing," *Journal of Heat Transfer,* vol. 126, p. 566, 2004.

[11] P. Raj*, et al.*, "Three-dimensional computational modelling of momentum, heat and mass transfer in laser surface alloying with distributed melting of alloying element," *International Journal of Numerical Methods for Heat & Fluid Flow,* vol. 11, pp. 576-599, 2001.

[12] P. Wei and J. Ho, "Energy considerations in high-energy beam drilling," *International Journal of Heat and Mass Transfer,* vol. 33, pp. 2207-2217, 1990.

[13] A. Fathi*, et al.*, "Prediction of melt pool depth and dilution in laser powder deposition," *Journal of Physics D: Applied Physics,* vol. 39, p. 2613, 2006.

[14] Z. Shen*, et al.*, "Mathematical modeling of laser induced heating and melting in solids," *Optics & laser technology,* vol. 33, pp. 533-537, 2001.

[15] J. Van de Ven and A. Erdman, "Laser Transmission Welding of Thermoplastics—Part I: Temperature and Pressure Modeling," *Journal of Manufacturing Science and Engineering,* vol. 129, p. 849, 2007.

[16] D. Chatterjee and S. Chakraborty, "An enthalpy-based lattice Boltzmann model for diffusion dominated solid-liquid phase transformation," *Physics Letters A,* vol. 341, pp. 320-330, 2005.

[17] S. Sarkar*, et al.*, "Three-dimensional computational modeling of momentum, heat, and mass transfer in a laser surface alloying process," *Numerical Heat Transfer, Part A: Applications,* vol. 42, pp. 307-326, 2002.

[18] B. Yilbas and S. Mansoor, "Laser evaporative heating of surface: simulation of flow field in the laser produced cavity," *Journal of Physics D: Applied Physics,* vol. 39, p. 3863, 2006.

[19] B. Yilbas*, et al.*, "Laser pulse heating and vapor front generation," *AIChE Journal,* vol. 54, pp. 627-638, 2008.

[20] B. Yilbas and S. Shuja, "Laser non-conduction limited heating and prediction of surface recession velocity in relation to drilling," *Proceedings of the Institution of Mechanical Engineers, Part C: Journal of Mechanical Engineering Science,* vol. 217, pp. 1067-1075, 2003.

[21] J. Li*, et al.*, "Comparison of volumetric and surface heating sources in the modeling of laser melting of ceramic materials," *International Journal of Heat and Mass Transfer,* vol. 47, pp. 1159-1174, 2004.

[22] A. De*, et al.*, "Finite element simulation of laser spot welding," *Science and Technology of Welding &# 38; Joining,* vol. 8, pp. 377-384, 2003.

[23] U. Paek and F. Gagliano, "Thermal analysis of laser drilling processes," *Quantum Electronics, IEEE Journal of,* vol. 8, pp. 112-119, 2002.

[24] T. Elperin and G. Rudin, "Thermoelasticity problem for a multilayer coating-substrate assembly irradiated by a laser beam," *International Communications in Heat and Mass Transfer,* vol. 23, pp. 133-142, 1996.

[25] H. Wang*, et al.*, "A study of thermal stresses during laser quenching," *Journal of Materials Processing Technology,* vol. 63, pp. 550-553, 1997.

[26] B. Yilbas*, et al.*, "Laser-induced thermal stresses on steel surface," *Optics and Lasers in Engineering,* vol. 30, pp. 25-37, 1998.

[27] S. Shuja and B. Yilbas, "3-Dimensional conjugate laser heating of a moving slab," *Applied Surface Science,* vol. 167, pp. 134-148, 2000.

[28] L. Yang*, et al.*, "Numerical modeling and experimental investigation on the characteristics of molten pool during laser processing," *International Journal of Heat and Mass Transfer,* vol. 44, pp. 4465-4473, 2001.

[29] D. Sowdari and P. Majumdar, "Finite element analysis of laser irradiated metal heating and melting processes," *Optics & laser technology,* vol. 42, pp. 855-865, 2010.

[30] A. Kumar and S. Roy, "Effect of three-dimensional melt pool convection on process characteristics during laser cladding," *Computational Materials Science,* vol. 46, pp. 495-506, 2009.

[31] B. Yilbas*, et al.*, "Laser treatment of aluminum surface: Analysis of thermal stress field in the irradiated region," *Journal of Materials Processing Technology,* vol. 209, pp. 77-88, 2009.

[32] O. Velde*, et al.*, "Numerical investigations of Lorentz force influenced Marangoni convection relevant to aluminum surface alloying," *International Journal of Heat and Mass Transfer,* vol. 44, pp. 2751-2762, 2001.

[33] S. Shuja*, et al.*, "Laser consecutive pulse heating and phase change: Influence of spatial distribution of laser pulse intensity on melting," *International Journal of Thermal Sciences,* vol. 48, pp. 1960-1966, 2009.

[34] Y. Lei*, et al.*, "Numerical analysis of the competitive influence of Marangoni flow and evaporation on heat surface temperature and molten pool shape in laser surface remelting," *Computational Materials Science,* vol. 21, pp. 276-290, 2001.

[35] N. Chakraborty and S. Chakraborty, "Modelling of turbulent molten pool convection in laser welding of a copper-nickel dissimilar couple," *International Journal of Heat and Mass Transfer,* vol. 50, pp. 1805-1822, 2007.

[36] J. Li*, et al.*, "A three-dimensional numerical model for a convection-diffusion phase change process during laser melting of ceramic materials," *International Journal of Heat and Mass Transfer,* vol. 47, pp. 5523-5539, 2004.

[37] B. Yilbas and I. Naqvi, "Laser heating including the phase change process and thermal stress generation in relation to drilling," *Proceedings of the Institution of*

Mechanical Engineers, Part B: Journal of Engineering Manufacture, vol. 217, pp. 977-991, 2003.

[38] P. Mohan Raj*, et al.*, "Modelling of transport phenomena in laser surface alloying with distributed species mass source* 1," *International Journal of Heat and Fluid Flow,* vol. 23, pp. 298-307, 2002.

[39] A. Pinkerton and L. Li, "Modelling the geometry of a moving laser melt pool and deposition track via energy and mass balances," *Journal of Physics D: Applied Physics,* vol. 37, p. 1885, 2004.

[40] H. Chung and S. Das, "Numerical modeling of scanning laser-induced melting, vaporization and resolidification in metals subjected to step heat flux input," *International Journal of Heat and Mass Transfer,* vol. 47, pp. 4153-4164, 2004.

[41] B. Yilbas*, et al.*, "Laser welding of low carbon steel and thermal stress analysis," *Optics & laser technology,* vol. 42, pp. 760-768, 2010.

[42] J. Chen and Y. Huang, "Thermocapillary flows of surface melting due to a moving heat flux," *International Journal of Heat and Mass Transfer,* vol. 34, pp. 663-671, 1991.

[43] M. Alimardani*, et al.*, "A 3D dynamic numerical approach for temperature and thermal stress distributions in multilayer laser solid freeform fabrication process," *Optics and Lasers in Engineering,* vol. 45, pp. 1115-1130, 2007.

[44] N. Ahmed*, et al.*, "Investigation into the effect of beam shape on melt pool characteristics using analytical modelling," *Optics and Lasers in Engineering,* vol. 48, pp. 548-554, 2010.

[45] E. Toyserkani*, et al.*, "3-D finite element modeling of laser cladding by powder injection: effects of laser pulse shaping on the process," *Optics and Lasers in Engineering,* vol. 41, pp. 849-867, 2004.

[46] S. Nisar*, et al.*, "The Effect of Laser Beam Geometry on Cut Path Deviation in Diode Laser Chip-Free Cutting of Glass," *Journal of Manufacturing Science and Engineering,* vol. 132, p. 011002, 2010.

[47] S. Safdar*, et al.*, "An analysis of the effect of laser beam geometry on laser transformation hardening," *Journal of Manufacturing Science and Engineering,* vol. 128, p. 659, 2006.

[48] S. Safdar*, et al.*, "Thermal history analysis of surface heating of mild steel with different laser beam geometries," *Proceedings of the Institution of Mechanical Engineers, Part C: Journal of Mechanical Engineering Science,* vol. 220, pp. 1549-1557, 2006.

[49] Y. Kim and W. Kim, "A numerical analysis of heat and fluid flow with a deformable curved free surface in a laser melting process," *International Journal of Heat and Fluid Flow,* vol. 29, pp. 1481-1493, 2008.

[50] H. Wang*, et al.*, "Effect of pressure gradient driven convection in the molten pool during the deep penetration laser welding," *Journal of Materials Processing Technology,* vol. 184, pp. 386-392, 2007.

[51] X. Peng*, et al.*, "Effects of initial molten pool and Marangoni flow on solid melting," *International Journal of Heat and Mass Transfer,* vol. 44, pp. 457-470, 2001.

[52] D. Höche*, et al.*, "Marangoni Convection during Free Electron Laser Nitriding of Titanium," *Metallurgical and Materials Transactions B,* vol. 40, pp. 497-507, 2009.

[53] B. Sim and W. Kim, "Melting and dynamic-surface deformation in laser surface heating," *International Journal of Heat and Mass Transfer,* vol. 48, pp. 1137-1144, 2005.

[54] C. Zhao*, et al.*, "The effect of oxygen on transitional Marangoni flow in laser spot welding," *Acta Materialia,* 2010.

[55] D. Morvan*, et al.*, "Convection thermocapillaire au cours d'une opération de refusion superficielle par laser: Thermocapillary convection during laser surface melting," *International Journal of Heat and Mass Transfer,* vol. 37, pp. 1973-1983, 1994.

[56] B. Yilbas*, et al.*, "Laser nitriding of tool steel: thermal stress analysis," *The International Journal of Advanced Manufacturing Technology,* pp. 1-10, 2010.

[57] H. Al-Qahtani and B. Yilbas, "Comparison of temperature field due to laser step input and time exponentially varying pulses," *Optics & laser technology,* vol. 41, pp. 931-937, 2009.

[58] A. Matsunawa and T. Ohji, "Role of surface tension in fusion welding (part 1)," *JWRI 1982 11 (2) 145,* vol. 154.

[59] A. Matsunawa and T. Ohji, "Role of surface tension in fusion welding (part 3)," *JWRI 1984 13 (1) 147,* vol. 156.

[60] A. Matsunawa and T. Ohji, "Role of surface tension in fusion welding (part 2)," *JWRI 1983 12 (1) 124,* vol. 130.

[61] U. Gratzke*, et al.*, "Theoretical approach to the humping phenomenon in welding processes," *Journal of Physics D: Applied Physics,* vol. 25, p. 1640, 1992.

[62] M. Beck*, et al.*, "Aspects of keyhole/melt interaction in high-speed laser welding," 1991, p. 769.

[63] A. Mackwood and R. Crafer, "Thermal modelling of laser welding and related processes: a literature review," *Optics & laser technology,* vol. 37, pp. 99-115, 2005.

[64] S. Lambrakos*, et al.*, "A numerical model for deep penetration welding processes," *Journal of Materials Engineering and Performance,* vol. 2, pp. 819-836, 1993.

[65] P. Klemens, "Heat balance and flow conditions for electron beam and laser welding," *Journal of Applied Physics,* vol. 47, pp. 2165-2174, 2009.

[66] J. Andrews and D. Atthey, "Hydrodynamic limit to penetration of a material by a high-power beam," *Journal of Physics D: Applied Physics,* vol. 9, p. 2181, 1976.

[67] J. Dowden*, et al.*, "A keyhole model in penetration welding with a laser," *Journal of Physics D: Applied Physics,* vol. 20, p. 36, 1987.

[68] J. Kroos*, et al.*, "Dynamic behaviour of the keyhole in laser welding," *Journal of Physics D: Applied Physics,* vol. 26, p. 481, 1993.

[69] R. Fabbro and K. Chouf, "Keyhole modeling during laser welding," *Journal of Applied Physics,* vol. 87, p. 4075, 2000.

[70] R. Fabbro and K. Chouf, "Dynamical description of the keyhole in deep penetration laser welding," *Journal of Laser Applications,* vol. 12, p. 142, 2000.

[71] V. Voller and C. Prakash, "A fixed grid numerical modelling methodology for convection-diffusion mushy region phase-change problems," *International Journal of Heat and Mass Transfer,* vol. 30, pp. 1709-1719, 1987.

[72] S. Patankar, *Numerical heat transfer and fluid flow*: Hemisphere Pub, 1980.

[73] *Fluent Theory Guide*, Ansys Inc.

[74] W. Gale*, et al.*, *Smithells metals reference book*: Butterworth-Heinemann, 2004.

[75] WolframAlpha Knowledgebase 2010 [Online].

[76] L. Gardner*, et al.*, "Elevated temperature material properties of stainless steel alloys," *Journal of Constructional Steel Research,* vol. 66, pp. 634-647, 2010.

[77] J. Rempe*, et al.*, "High Temperature Thermal and Structural Material Properties for Metals Used in LWR Vessels," Idaho National Laboratory (INL)2008.

[78] B. Yilbas*, et al.*, "Study into the measurement and prediction of penetration time during CO 2 laser cutting process," *ARCHIVE: Proceedings of the Institution of Mechanical Engineers, Part B: Journal of Engineering Manufacture 1989-1996 (vols 203-210),* vol. 204, pp. 105-113, 1990.

[79] B. Yilbas*, et al.*, "Laser gas assisted nitriding and tin coating of Ti-6Al-4V alloy: Experimental and numerical investigation of mechanical properties," *Journal of Materials Processing Technology,* vol. 209, pp. 1199-1208, 2009.

VITAE

Name: Omeir Momin

Nationality: Pakistani

Present Address: Muhammad Mushtaq, SaudConsult, P.O. Box 1293, Dammam 31431, Saudi Arabia

Permanent Address: Saad Mahmood, 7-Chah Shahanwala, Gujranwala, Pakistan

Telephone: 00966544990244

Education: Received Degree of Bachelor in Mechanical Engineering from NUST, Pakistan.

Joined Mechanical Engineering Department of King Fahd University of Petroleum and Minerals, Dhahran as Research Assistant in October 2008.

E-mail: omeirmomin@gmail.com